

REPORT DOCUMENTATION PAGE

Public reporting burden for this collection of information is estimated to average 1 hour per response, including the time for reviewing instructions, searching existing data sources, gathering the required data, completing and reviewing this collection of information. Send comments regarding this burden estimate or any other aspect of this collection of information, including suggestions for reducing this burden to Washington Headquarters Services, Directorate for Information Operations and Reports (0704-0188), 1215 Jefferson Davis Boulevard, Arlington, VA 22202-4302. Respondents should be aware that notwithstanding any other provision of law, no person shall be subject to any penalty for failing to comply with a collection of information if it does not display a currently valid OMB control number. **PLEASE DO NOT RETURN YOUR FORM TO THE ABOVE ADDRESS.**

1. REPORT DATE (DD-MM-YYYY) 29-07-2004		2. REPORT TYPE Final		3. DATES COVERED (From - To) 30-09-2003 - 29-07-2004	
4. TITLE AND SUBTITLE Computational Methods for Feedback Controllers for Aerodynamic Flow Applications				5a. CONTRACT NUMBER F49620-03-C-0108	
				5b. GRANT NUMBER	
				5c. PROGRAM ELEMENT NUMBER	
6. AUTHOR(S) Siegel, Stefan; McLaughlin, Thomas E.; Cohen, Kelly; Seidel, Jürgen; Luchtenburg, Mark; Wetlesen, David; Strang, William Z., Forsythe, James R.				5d. PROJECT NUMBER	
				5e. TASK NUMBER	
				5f. WORK UNIT NUMBER	
7. PERFORMING ORGANIZATION NAME(S) AND ADDRESS(ES) Cobalt Solutions, LLC 4636 New Carlisle Pike Springfield, OH 45504-3336				8. PERFORMING ORGANIZATION REPORT NUMBER F49620-03-C-0108-04	
9. SPONSORING / MONITORING AGENCY NAME(S) AND ADDRESS(ES) Air Force Office of Scientific Research 4015 Wilson Blvd, Room 713 Arlington, VA 22203-1954				10. SPONSOR/MONITOR'S ACRONYM(S) AFOSR/NM	
				11. SPONSOR/MONITOR'S REPORT NUMBER(S)	
12. DISTRIBUTION / AVAILABILITY STATEMENT Approved for public release; distribution unlimited.					
13. SUPPLEMENTARY NOTES					
14. ABSTRACT Report developed under STTR contract for topic AF03T007. This document represents the final report of a phase I STTR program between the USAF Academy Department of Aeronautics and Cobalt Solutions, LLC. The goal of the STTR is to develop a set of computational design tools for closed loop flow control. These tools need to cover the entire design cycle from plant characterization through control system development to testing of the control algorithms against truth models and finally experiments. The specific goal of the phase I was to demonstrate feasibility of the proposed approach by applying it to three challenging test cases: the circular cylinder, the "D" shaped cylinder, and the NACA 0015 airfoil. These three cases were chosen because of the differing approaches needed for each problem. Both cylinders need to be controlled by stabilizing the wake. The circular cylinder has variable separation points (depending on control input), while the "D" shaped cylinder has fixed separation. The airfoil may be controlled strictly by controlling the separation (i.e. eliminating it). These cases were all treated in 2-D to demonstrate feasibility prior to attempting control in 3-D.					
15. SUBJECT TERMS STTR Report; Feedback Flow Control; Computational Fluid Dynamics					
16. SECURITY CLASSIFICATION OF:			17. LIMITATION OF ABSTRACT UU	18. NUMBER OF PAGES	19a. NAME OF RESPONSIBLE PERSON William Z. Strang
a. REPORT U	b. ABSTRACT U	c. THIS PAGE U			19b. TELEPHONE NUMBER (include area code) (937) 902-6108

Standard Form 298 (Rev. 8-98)
Prescribed by ANSI Std. Z39.18

BEST AVAILABLE COPY

20040810 023



Computational Methods for Feedback Controllers for Aerodynamics Flow Applications

**Cobalt Solutions, LLC
USAF Academy**

**Contract: F49620-03-C-0108
STTR Final Report
29 July, 2004**



Executive Summary

This document represents the final report of a phase I STTR program between the USAF Academy Department of Aeronautics and Cobalt Solutions, LLC. The goal of the STTR is to develop a set of computational design tools for closed loop flow control. These tools need to cover the entire design cycle from plant characterization through control system development to testing of the control algorithms against truth models and finally experiments. The specific goal of the phase I was to demonstrate feasibility of the proposed approach by applying it to three challenging test cases: the circular cylinder, the "D" shaped cylinder, and the NACA 0015 airfoil. These three cases were chosen because of the differing approaches needed for each problem. Both cylinders need to be controlled by stabilizing the wake. The circular cylinder has variable separation points (depending on control input), while the "D" shaped cylinder has fixed separation. The airfoil may be controlled strictly be controlling the separation (i.e. eliminating it). These cases were all treated in 2-D to demonstrate feasibility prior to attempting control in 3-D.

The approach taken was to combine a computational fluid dynamics solver that is able to handle complex geometries with low dimensional modeling. Improvements were made in the CFD solver in order to performed closed loop simulations with blowing/suction in addition to the existing motion capability and several closed loop interface and post processing improvements. Numerous Matlab routines were developed and applied including a Proper Orthogonal Decomposition (POD) Algorithm, a State Equation (SEQ) Algorithm, a Linear Stochastic Estimation (LSE) Algorithm a Closed Loop Simulation Module, Controllability, Observability, and Stability (COS) Algorithms, and Sensor Placement and Mode Estimation Modules (SME). The toolbox was applied to the three cases outlined with demonstrated success on all three. The cylinder wakes were stabilized to a large extent with a reduction in lift oscillations and drag. The separation on the NACA 0015 was reduced, though not eliminated (in the mean). The tools were very useful in designing controllers for all three cases. Conclusions and lessons learned from these test cases are outlined with recommendations made for proceeding to phase II of the STTR.



Main Contributors and Acknowledgements

Cobalt Solutions, LLC

- Mr. William Z. Strang
- Dr. James R. Forsythe

USAF Academy

- Dr. Stefan Siegel
- Dr. Thomas E. McLaughlin
- Dr. Kelly Cohen (via a Project Agreement with Israel)
- Dr. Jürgen Seidel
- Mr. Mark Luchtenburg
- Lt. Col. David Wetlesen
- USAFA cadets within the framework of 471/499 classes

The USAFA team would like to acknowledge the support of the USAFA/DFAN Modeling and Simulation Center headed by Lt. Col. Scott Morton. Furthermore, the USAFA team would like to thank the technical and administrative staff at the USAFA/DFAN Laboratory for their support of the research program.

Note: Publications related to this research have a "*" in the bibliography

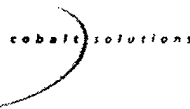
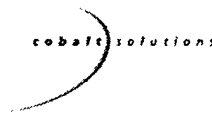


Table of Contents

Executive Summary.....	1
1. Introduction.....	4
1.1 Significance of Problem	4
1.2 Main Objectives.....	5
1.3 Toolbox Application.....	6
2. Computational Tools Development.....	8
2.1 Overview of COBALT CFD Solver.....	8
2.2 Development and Coding Issues	9
2.3 Debugging Issues.....	11
2.4 Computational Highlights.....	11
3. Modeling, Estimation and Control Tools Development.....	13
3.1 Modeling Approaches.....	13
3.2 Proper Orthogonal Decomposition (POD)	15
3.3 Sensor Configuration, Estimation and Observability	19
3.4 Controllability, and Stability (COS) Algorithms.....	21
3.5 Important Control Lessons Learned	23
4. Application I: Circular Cylinder Wake Control	24
4.1 Circular Cylinder: Introduction	24
4.2 Circular Cylinder: Numerical Methods	26
4.3 Circular Cylinder: POD Modeling and Estimation	27
4.4 Circular Cylinder: Controller.....	31
4.5 Circular Cylinder: Results	31
4.6 Circular Cylinder: 3-D High Reynolds Number Baseline CFD	43
4.7 Summary.....	45
5. Application II: "D" Shaped Cylinder Wake Control.....	46
5.1 "D" Shaped Cylinder: Application Background.....	46
5.2 "D" Shaped Cylinder: Surface Mounted Sensor Estimation	47
5.3 "D" Shaped Cylinder: Blowing/Suction Modeling	58
5.4 "D" Shaped Cylinder: Feedback Controlled Results and Discussion	60
5.5 "D" Shaped Cylinder: Experimental Validation and Discussion	63
5.6 "D" Shaped Cylinder: 3-D High Reynolds Number Baseline CFD.....	64
6. Application III: NACA 0015 Airfoil Separation Control.....	66
6.1 NACA 0015 Airfoil: Application Background.....	66
6.2 NACA 0015 Airfoil: Computational Model.....	66
6.3 NACA 0015 Airfoil: Computational Results and Discussion	67
6.4 NACA 0015 Airfoil: 3-D Baseline CFD	74
7. Summary of Phase I & Recommendations for Phase II	75
7.1 Main Achievements of Phase I.....	75
7.2 Recommended Development Approach for Phase II	76
8. Matlab Modeling and Control Toolbox Suite.....	77
9. References.....	81



1. Introduction

1.1 Significance of Problem

The main idea of flow control is the improvement of aerodynamic characteristics of air vehicles and munitions enabling augmented mission performance. Flow control can either be passive or active depending on whether energy is added to the flow. Furthermore, active flow control may be characterized by open-loop or closed-loop techniques. Gad-el-Hak (1996) provides an insight into the advances in the field of flow control. Research into closed-loop flow control methods has increased over the past two decades. Cattafesta et al (2003) provide a useful classification of active flow control and describes the main components of a feedback control system. Before proceeding into the details of modeling and control, it is imperative to appreciate the reasons as to why closed-loop control is of consequence and the main advantages associated with its implementation in flow control problems. It is advantageous to opt for closed-loop flow control for it:

- Enables addressing problems that have over the years not been solved using passive means and /or open-loop techniques.
- Provides performance augmentation of an open-loop flow control system.
- Lowers the amount of energy required to manipulate the flow to induce the desired behavior. This aspect affects actuation requirement and may be a deciding factor.
- Enables adaptability to a wider operating envelope, thereby limiting the drop in performance associated with multiple design working points.
- Provides design flexibility and robustness.

Feedback flow control is an emerging discipline which aims at applying the methods of closed loop feedback control to problems in fluid dynamics. Traditionally, these two research fields have existed independently and without mutual involvement. Control scientists have applied their knowledge historically to problems with a relatively small dimensionality. Single input single output systems of linear behavior are very well understood and theoretically covered. More recently, feedback control has been applied to more complex problems in structural dynamics as well as fluid-structure interaction. These problems are of higher dimensionality and typically can be described by a small number of dominant modes. They also often involve multiple sensors and actuators. Feedback control of relatively complex structures is currently state of the art in control sciences, and very few control researchers have ventured into problems of higher complexity. Several applications of closed-loop control have been reported in literature. Specific areas of interest include flow-induced cavity resonance (Cattafesta, 2003), vectoring control of a turbulent jet, separation control of the NASA Langley hump model (a variation on the Glauert Glas II airfoil) control of the vortex motion in the combustion recirculation region and control of vortex shedding in circular cylinder wakes.

Even simple problems in fluid dynamics, however, present themselves to the control scientist as a system of much higher dimensionality whose governing equations are highly nonlinear and, for most all boundary conditions of technical interest, cannot be solved in closed form. This poses a formidable challenge for the application of feedback flow control to fluid dynamics problems of technical interest. On the other hand, since most fluid dynamics problems are featuring local or global instabilities, feedback flow control holds great promise in improving these flow fields with very



moderate control inputs, while yielding large reductions in flow quantities of technical importance like drag and unsteadiness of loads imposed by the flow field onto structures exposed to the flow.

The biggest challenge to be overcome in order to be able to make progress in the field of feedback flow control is in the area of modeling the dynamics of the flow field. So far, there have been three different approaches to modeling. Fluid dynamics researchers usually refrained from modeling the flow at all. Instead, they relied on empirical tuning of black box type controllers. Their attempt to control flow fields was met with very moderate success, and only for very simple flow fields were they able to achieve significant improvements. The linear control strategies applied were typically limited to single sensor / single actuator scenarios and important questions of controllability and observability could not be addressed due to the nonexistence of a mathematical model which is a prerequisite for this kind of investigations.

The second approach, usually employed by researchers with a background in applied mathematics, is based on solving the Navier Stokes equations and their respective boundary conditions using discretization on a grid and numerical methods. While this approach is shared by the field of computational fluid dynamics (CFD), for application to feedback control not just the forward problem that CFD solves but also the inverse problem needs to be considered especially when optimum controls approaches are considered. This leads to various forms of the Ricatti equations, which have proven to be much more difficult to solve than the Navier Stokes equations themselves. For most fluid dynamics problems a solution of the Ricatti equations with current state of the art computing methods seems out of reach. The problems encountered by both of these approaches to feedback flow control led to the third approach which employs low dimensional modeling. This technique has been applied with great success to control problems involving structural dynamics. The goal is to capture the relevant dynamics of the system, be it a mechanical structure or a flow field, by a finite number of spatial modes. The state of the system is then characterized by these modes, and an observer or state estimator is usually employed to derive the state of the system in terms of the mode amplitudes based on sensor readings. The controller then acts on the mode estimates as opposed to the sensor readings. The advantage of this approach is in the ability to actually model the important features of the system without having to solve the governing equations directly or numerically. Furthermore, the model can be derived from either experimental or simulation data, thus allowing development of a controller based on the dynamics of the actual system that is to be controlled. Of the three described attempts at feedback flow control, the use of low dimensional modeling has shown the greatest promise to date.

1.2 Main Objectives

This STTR research program aims at developing computational tools necessary to develop feedback control algorithms based on low dimensional models. These tools need to cover the entire design cycle from plant characterization through control system development to testing of the control algorithms against truth models and finally experiments. Currently, no such tools are commercially available, and researchers interested in feedback flow control have to develop their own tools from scratch. Since neither controls nor fluids experts are typically expert programmers, they need to expend significant time and effort to even obtain tools of limited functionality, typically only usable for a very specific problem. The main goal of this STTR collaboration between the US Air Force Academy and Cobalt Solutions is to join the controls and fluids expertise at the Academy with the programming and numerical mathematical solution skills at Cobalt Solutions. The result will be a toolbox that provides



an integrated closed loop flow control development environment covering the entire range of tasks from fluid dynamics simulation through low order modeling, mathematical model development and controller design to controller implementation and testing of the controller design by applying it to a truth model based on closed loop fluid dynamic simulation.

The toolbox enables closed loop CFD simulations based on Low-Dimensional Models obtained from POD. The toolbox features the following main components:

- Computational Fluid Dynamics (CFD) Solver
- Proper Orthogonal Decomposition (POD) Algorithm
- State Equation (SEQ) Algorithm
- Linear Stochastic Estimation (LSE) Algorithm
- Closed Loop Simulation Module
- Controllability, Observability, and Stability (COS) Algorithms
- Sensor Placement and Mode Estimation Modules (SME)

These tools cover the entire controller design cycle from model development through control algorithm design to verification of the design on the truth model.

1.3 Toolbox Application

In order to demonstrate and evaluate the performance of the toolbox components developed, we plan to use three (3) different benchmark problems:

- Circular Cylinder
- D- Shaped Cylinder
- Symmetric airfoil (NACA 0015) at high angle of attack

While the first two geometries develop a typical wake flow featuring an absolute instability, the third geometry aims at separation control.

Absolutely unstable wake flows have proven to be one of the most intractable problems in fluid dynamics using active open loop flow control. Typically, the unsteadiness of the flow is actually increased along with an increase in drag, or the small performance gain achieved using high amplitude forcing at high frequencies does not outweigh the energy expended for the forcing. Thus this type of flow is an ideal benchmark problem for feedback flow control, and success at very small Reynolds numbers has been achieved.

While separation control has been successfully addressed in literature using open loop forcing techniques, it will be interesting to see what performance gain can be achieved using closed loop techniques. This makes the airfoil at high angle of attack an interesting feedback flow control problem.

The different forcing methods outlined in the previous section will be applied to demonstrate the capabilities of the system. State estimation will be obtained both using sensors distributed in the flow field, as well as surface mounted sensors. Linear stochastic estimation will be employed for the surface mounted sensors to map their readings to POD mode amplitude estimates. For all three geometries, we will keep the Reynolds numbers low enough to be able to obtain physical results without the use of turbulence models.



This report paper is organized as follows: The next section provides an overview on the computational tools developed within the framework of this Phase I STTR program. The modeling and control aspects are presented in the following section, and the applications of the design tools are presented in the following three chapters. The first application is the circular cylinder followed by the D- shaped cylinder and finally by a symmetric airfoil (NACA 0015). Then, a chapter summarizes Phase I and presents recommendations for Phase II. At the end of the report, we have included a listing of the main Matlab files developed in the areas of modeling, estimation and control.



2. Computational Tools Development

2.1 Overview of COBALT CFD Solver

The CFD solver used is *Cobalt*, a commercial unstructured finite-volume code developed for solution of the compressible Navier-Stokes equations. The basic algorithm is described in Strang *et al.* (1999), although substantial changes/improvements have been made since this paper. The numerical method is a cell-centered finite volume approach applicable to arbitrary cell topologies (e.g., hexahedrals, prisms, tetrahdra). The spatial operator uses the exact Riemann Solver of Gottlieb and Groth (1988), least squares gradient calculations using QR factorization to provide second order accuracy in space, and TVD flux limiters to limit extremes at cell faces. A point implicit method using analytic first-order inviscid and viscous Jacobians is used for advancement of the discretized system. For time-accurate computations, a Newton sub-iteration scheme is employed, the method is second order accurate in time.

For parallel performance, *Cobalt* utilizes the domain decomposition library ParMETIS (Karypis *et al.* 1997) to provide optimal load balancing with a minimal surface interface between zones. Communication between processors is achieved using Message Passing Interface (MPI), with parallel efficiencies above 95% on as many as 1024 processors (Grismer *et al.* 1998).

The vast majority of Air Force vehicles operate at high Reynolds numbers where the fluid is turbulent. The main methods for calculating turbulent flows with a CFD solver are Direct Numerical Simulation (DNS), Large Eddy Simulation (LES), and Reynolds-averaged Navier Stokes (RANS). The RANS approach is the most economical since it is designed to solve for the mean flow, but is subject to many modeling approximations. Since it models rather than resolves the bulk if not all of the turbulent motions this is an inappropriate choice for most flow control applications. DNS, on the other hand, makes no modeling assumption but is the most expensive approach since all turbulent motions must be resolved by the grid. Since the smallest scales of turbulence (the Kolmogorov length scale) decrease with Reynolds number, this limits this approach to low Reynolds number flows. LES is less expensive than DNS since it models only the small subgrid scales of motion and resolves the rest of the turbulent motions. However, since the "large" scales in the boundary layer are on the order of the boundary layer thickness (which is quite thin for high Reynolds number flows), this method is cost prohibitive at high Reynolds numbers for wall bounded flows.

Detached-Eddy Simulation (DES) is a hybrid technique first proposed by Spalart *et al.* (1997) for prediction of turbulent flows at high Reynolds numbers (see also Spalart 2000). The motivation for developing DES was to combine the most favorable aspects of RANS and LES, i.e., the acceptable predictions using RANS models of thin shear layers (e.g., attached boundary layers) and LES for resolution of time-dependent, three-dimensional large eddies. For natural applications of DES, RANS is applied in the boundary layer, while outside the boundary layer in the separated region. An array of flows ranging from "building block" applications such as the flow over a cylinder, sphere, aircraft forebody, and missile base to complex geometries including full aircraft have been modeled (e.g., see Travin *et al.* 2001, Squires *et al.* 2001, Constantinescu *et al.* 2002, Forsythe *et al.* 2002, Hansen and Forsythe 2003, Constantinescu *et al.* 2003). These and other applications have been largely successful, illustrating DES capabilities in accurately resolving chaotic unsteady features in the separated regions along with a rational treatment of the attached boundary layers. Recent DES predictions of the flow



around complex configurations (all with *Cobalt*) include the massively separated flow around an F-15E at 65° angle of attack reported by Forsythe *et al.* (2004) (the first eddy-resolving simulation of flow around a full aircraft configuration), transonic shock-separated flow over an F/A-18E by Forsythe and Woodson (2003), and vortex breakdown on an F-18C by Morton *et al.* (2003).

The use of a pre-existing CFD code that has been thoroughly verified within the context of turbulence resolving calculations has reduce the costs/risks of the proposed work. The Phase I work with the CFD solver has consisted of integrating the solver more tightly with the flow control tools and building a 3D baseline of open loop applications.

2.2 Development and Coding Issues

First, it was decided that a Hierarchical Data Format (HDF) file would best serve as the communications interface between the fluid flow solver, Cobalt, and the USAFA-developed feedback controller. HDF, developed by the National Center for Supercomputing Applications, is a multi-object file format for sharing scientific data in a distributed environment. HDF is a standard file format in the science and engineering field, facilitating the incorporation of feedback controllers developed outside of USAFA. Also, the platform independence of HDF provides considerable flexibility in operating the feedback-controller-Cobalt-HDF system. For example, Cobalt could be running on 128-processor parallel computer, with the feedback controller running on an individual's workstation and the HDF file residing on a fileserver. The sole requirement is that the three machines are networked together.

Second, it was agreed upon that the feedback controller would control two similar boundary conditions in the fluid flow solver. Both boundary conditions simulate flow entering or leaving the fluid domain; differences between the two lie in the details. In the first method, called the "mass flow boundary condition", the external controller controls the mass flow entering or leaving the domain as well as the total temperature and total pressure of that mass flow. This boundary condition is valid for incompressible and compressible flows. The second boundary condition, called the "velocity boundary condition", is based on a method developed by S. A. Morton of USAFA. This method is strictly valid for incompressible flows only, but can be used with good results up to a Mach number of around 0.2. Here, the external controller controls only the velocity of the fluid entering or leaving the domain; pressure and temperature conditions can be derived based on the knowledge of the temporal derivative of velocity (calculated either by the external controller or by the fluid flow solver) with the assumption of incompressible flow.

The mass flow boundary condition was first added to Cobalt and validated. The validation was straightforward, since this boundary condition is the simple union of two existing, and well validated, boundary conditions in Cobalt. The coding required for Cobalt to create, read from, and write to an HDF file was then accomplished. A very simple external controller was then developed to validate that information was being properly passed via the HDF file for a simple test case. Results of this test were compared with those resulting from a similar test where Cobalt itself varied the mass flow boundary condition in exactly the same manner as the external controller. Results between the two tests were identical to with machine round-off error.

Coding of the velocity boundary condition was accomplished. Since this boundary condition is new to Cobalt, it was subjected to extensive validation. However, once this validation was complete, integrating it with the HDF file interface advanced quickly, since much of the integration for the mass

flow boundary condition was reused. During the coding, an “open –loop” boundary condition was also added that did not require interfacing through HDF to an external controller. This module was used for the prediction of the flow over a wall mounted hump by Krishnan *et al.* (2004).

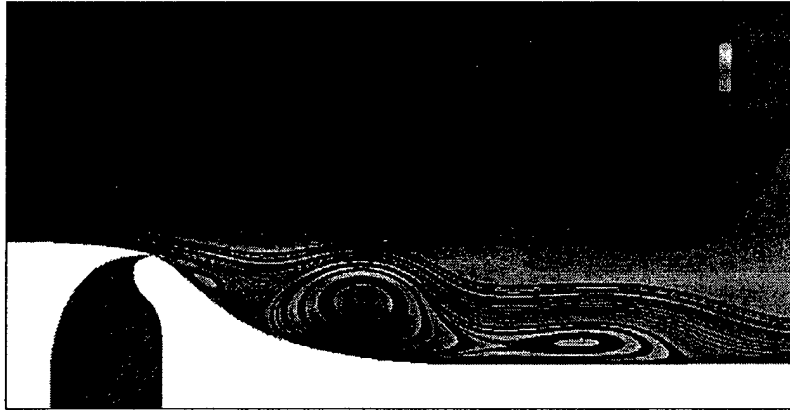


Fig. 2.1: Open loop blowing/suction using on the wall mounted hump by Krishnan *et al.* using Cobalt.
Contours of streamwise velocity with instantaneous streamlines.

Cobalt Solutions provided data exchange interfaces in the CFD solver that allowed both unforced and open loop forced data collection to HDF format files, as well as control interaction during a CFD simulation. The latter feature allowed the CFD Solver (Cobalt) to be used as a truth model to verify a given controller design. By using files in order to interface the CFD solver and the control toolbox, debugging of the overall system was facilitated. Additionally, the entire CFD code was not needed to be recompiled when new control algorithms were implemented. Within the Phase I, the following limitations were applied:

- All modules other than the CFD Solver were implemented in a high level language, in particular, in Matlab. Porting of Matlab algorithms to lower level languages and parallelization of these codes will be performed in Phase II, in order to accommodate larger (3D) data sets and improve performance.
- All closed loop simulations were two-dimensional in order to keep the required computation times low, while still being able to achieve the objective of demonstrating the performance of the tools. While open loop three-dimensional CFD performance was demonstrated in Phase I, closed loop 3D simulations will be performed in Phase II.
- All of the Matlab tools were implemented for two-dimensional datasets. Extension of the tool's capabilities to three-dimensions will take place in Phase II.

In order to perform closed loop flow control, actuation is needed. The following actuation approaches was developed and validated:

- Translation normal to the flow
- Blowing and suction at the model surface



The toolbox allows for an unlimited number of sensors to be placed within the computational domain. At any sensing location, the following flow variables will be available to the controller:

- All three velocity components (U, V, W)
- Pressure
- Density

Additionally, the following global flow properties are available to the controller and can be used for closing the feedback loop:

- X,Y,Z components of force acting on the body
- X,Y,Z components of moment

As a result of the current research program, Cobalt can now output instantaneous flow data at arbitrary user-specified locations, 'taps', in Hierarchical Data Format (HDF). Previously, only ASCII format was available. Due to the nature of HDF, all flow quantities available for post-processing, 16 in all, are output for every tap. Optimization of the algorithm resulted in a very low interpolation overhead during the output of only 15% of the computational time per time step, for a large number of taps. Note that this overhead is only incurred during data output. Furthermore, the implementation of HDF output for an external controller, for both rigid body motion and blowing and suction boundary patches was successfully completed. An additional improvement is that the flow quantities are now tri-linearly interpolated to the taps. Previously, the computational cell containing any given tap was first found and the flow state at that cell centroid was then assigned to the tap location. The current method, while more accurate, requires additional CPU time over the original method. These two modifications have enabled more rapid and more accurate POD creation.

2.3 Debugging Issues

After development and coding of the toolbox components was accomplished, a thorough debugging phase followed. We compared the results of the toolbox modules to published literature wherever possible and available. Test cases were run to first verify the performance of the individual toolbox components separately. After the individual toolbox components performance were verified, the integration of the toolbox components with each other was tested, with particular attention on the interface between the CFD solver and the Matlab based components of the toolbox.

Finally, the external controller HDF interface was debugged in collaboration with USAFA. After debugging was completed, we applied the toolbox to the benchmark problems outlined in Section 1.3 of this report.

2.4 Computational Highlights

Overall, the final toolbox will be able to handle any flow geometry at any Reynolds number. The CFD solver is capable of handling unstructured grids. It can perform simulations from Euler through laminar Navier Stokes up to a variety of turbulence models as well as Detached-Eddy Simulation (DES). Rigid body motion as well as variable boundary conditions are implemented. On the toolbox side, all of the above features are supported, while limiting the flow geometry to two-dimensional at this point in time.



One of the main integration goals reached was to interface the toolbox to the CFD simulation using open standard data formats, in particular, the Hierarchical Data Format (HDF) developed by the National Center for Supercomputing Applications (NCSA). The open standard data format will allow users to use their plotting and data post processing software tools of choice, since most major software packages support this format. Additionally, this data format is very efficient in terms of file size while providing convenient and quick access to the data.



3. Modeling, Estimation and Control Tools Development

3.1 Modeling Approaches

A closed-loop flow control system is comprised of a controller that introduces a perturbation into the flow, via a set of actuators, to obtain desired performance. Furthermore, the controller acts upon information provided by a set of sensors. There are three basic approaches to closed-loop flow control of a two-dimensional wake as depicted in Figure 3.1.

Model Independent Approach - involves the introduction of sensors in the wake and using a control law (usually linear) which produces a command to the actuator that forces the flow. The advantage of this approach is to show:

- No model of the flow field is required for controller design.
- Direct feedback eliminates the need for a state estimator.
- A simple control law may be implemented in an experimental set up with relative ease.

For example, let us consider the circular cylinder wake problem. Experimental studies show that a linear proportional feedback control based on a single sensor feedback is able to delay the onset of the wake instability, rendering the wake stable at Re about 20% higher than the unforced case. Above $Re = 60$, a single-sensor feedback may suppress the original mode but destabilizes one of the other modes (Roussopoulos, 1993). This approach is relatively simple to implement experimentally. However, the results are very limited for the challenging problem of an absolutely unstable wake.

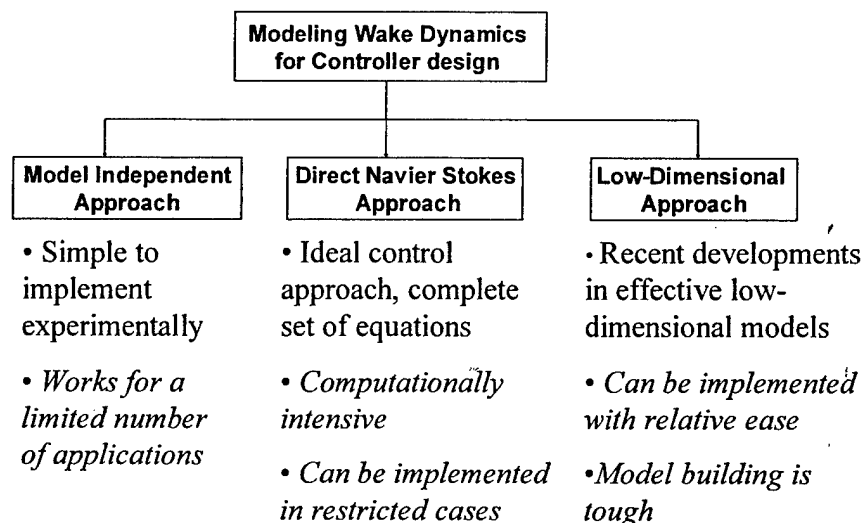
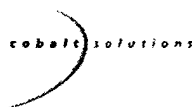


Fig. 3.1: Approaches to Closed-Loop Flow Control



Direct Navier Stokes Approach – This approach is more structured as it applies conventional and proven model-based control strategies such as optimal control theory for flow control problems. Abergel and Temam (1990) developed conditions for optimality for a few simple applications. However, real time implementation of this approach to the cumbersome unsteady Navier-Stokes equations is not practical.

Low-Dimensional Approach - Low-dimensional modeling is a vital building block when it comes to realizing a structured model-based closed-loop strategy for flow control. For control purposes, a practical procedure is needed to break down the velocity field, governed by Navier Stokes partial differential equations, by separating space and time. A common method used to substantially reduce the order of the model is proper orthogonal decomposition (POD). This method is an optimal approach in that it will capture a larger amount of the flow energy in the fewest modes of any decomposition of the flow. The POD method may be used to identify the characteristic features, or modes, of a cylinder wake as demonstrated by Gillies (1998).

The major building blocks of this structured approach are comprised of a reduced-order POD model, a state estimator and a controller. The desired POD model contains an adequate number of modes to enable reasonable modeling of the temporal and spatial characteristics of the large scale coherent structures inherent in the flow though it may faithfully reproduce the flow. Further details of the POD method may be found in the book by Holmes, Lumley, and Berkooz (1996). A common approach referred to as the method of “snapshots” introduced by Sirovich(1987) is employed to generate the basis functions of the POD spatial modes from flow-field information obtained using either experiments or numerical simulations. This approach to controlling the global wake behavior behind a circular cylinder was effectively employed by Gillies (1998) and is also the approach followed in this research effort.

For low-dimensional control schemes to be implemented, a real-time *estimation* of the modes present in the wake is necessary since it is not possible to measure them directly especially in real-time. An illustration of the various blocks within the low-dimensional modeling approach is presented in Fig. 3.2. Velocity field data, provided from either simulation or experiment, is fed into the POD procedure. The time histories of the temporal coefficients of the POD model are determined by applying the least squares technique to the spatial Eigen-functions and the unforced flow. Then, the estimation of the low-dimensional states is provided using a linear stochastic estimator (LSE). Sensor measurements may take the form of wake velocity measurements, as in this effort, or body-mounted pressure measurements. This process leads to the state and measurement equations, required for design of the control system. For practical applications it is desirable to reduce the information required for estimation to the minimum. The requirement for the estimation scheme then is to behave as a modal filter that “combs out” the higher modes. The main aim of this approach is to thereby circumvent the destabilizing effects of observation “spillover” as described by Balas (1978). Spillover has been the cause for instability in the control of flexible structures and modal filtering was found to be an effective remedy.



Basic Modeling Approach

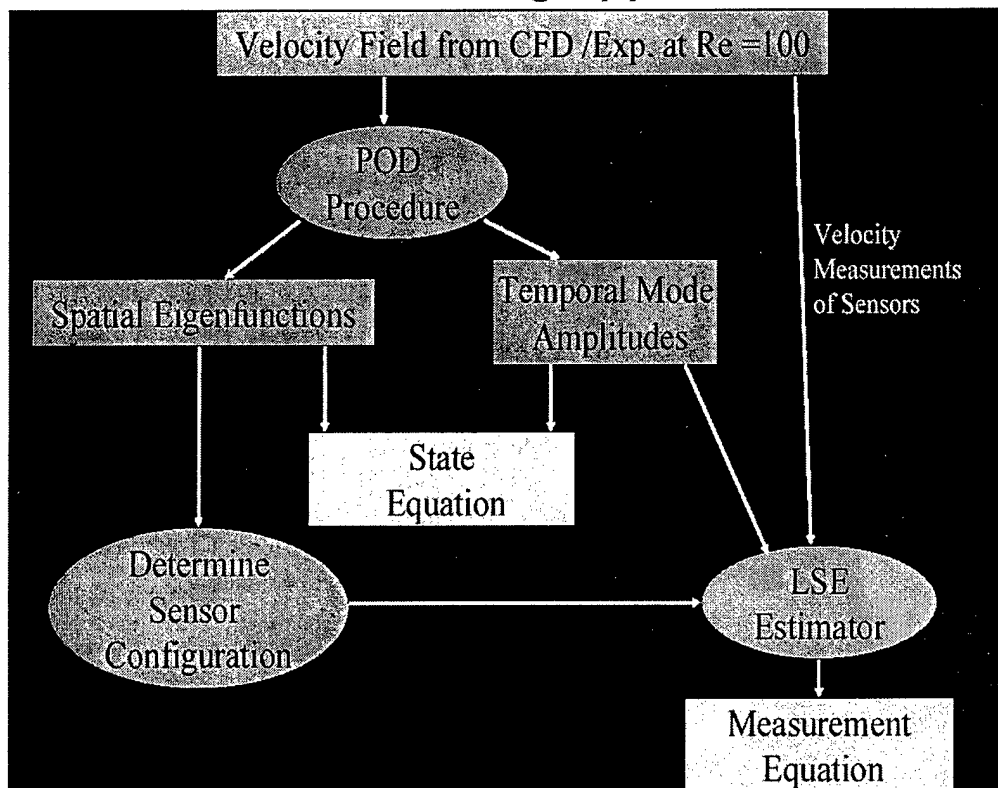


Fig. 3.2: Low-Dimensional Modeling Strategy

The intention of the proposed strategy is that the signals, provided by a certain configuration of sensors placed in the wake, are processed by the estimator to provide the estimates of the first two modes. The estimation scheme, based on the linear stochastic estimation procedure introduced by Adrian (1997), predicts the temporal amplitudes of the first two POD modes from a finite set of measurements obtained from either computational or experimental data. A major design challenge lies in finding an appropriate number of sensors and their locations that will best enable the desired modal filtering.

3.2 Proper Orthogonal Decomposition (POD)

Feasible real time estimation and control of the cylinder wake may be effectively realized by reducing the model complexity of the cylinder wake as described by the Navier-Stokes equations, using POD techniques. POD, a non-linear model reduction approach is referred to in the literature as the Karhunen-Loeve expansion. The desired POD model will contain an adequate number of modes to enable modeling of the temporal and spatial characteristics of the large-scale coherent structures inherent in the flow, but no more modes than necessary.



The basis functions of the POD spatial modes may be obtained from the numerical solution of the Navier-Stokes equations using CFD simulations or by incorporating experimental data. For control design purposes, the POD method enables the Navier-Stokes equations to be modeled as a set of ordinary differential equations (O.D.E.). The decomposition of this component of the velocity field is as follows:

$$\tilde{u}(x, y, t) = U(x, y) + u(x, y, t) \quad (3.1)$$

where $U[\text{m/s}]$ denotes the mean flow and $u[\text{m/s}]$ is the fluctuating component that may be expanded as:

$$u(x, y, t) = \sum_{k=1}^n a_k(t) \phi_i^{(k)}(x, y) \quad (3.2)$$

where $a_k(t)$ denotes the time-dependent coefficients and $\phi_i(x, y)$ represents the non-dimensional spatial Eigenfunctions determined from the POD procedure. In some cases the velocity component may represent the vorticity, which is calculated from the flow field.

Next, the empirical correlation matrix, R is computed. A simple approximation technique is applied to obtain the numerical integration. In this effort, the correlation matrix is computed using the inner product. Solving the Eigenvalue problem, the Eigenvalues and the orthogonal spatial Eigenfunctions, $\phi_i(x, y)$ are obtained. Since the Eigenvalues measure the relative energy of the system dynamics contained in that particular mode, they may be normalized to correspond to a percentage. Finally, the time histories of the temporal coefficients of the POD model, $a_k(t)$, are determined using the extracted spatial modes and the data of the unforced flow. For an arbitrarily forced circular cylinder, we can write the low-dimensional wake model as:

$$\frac{da_k}{dt} = g_k(a_n) + b_k f_a \quad (3.3)$$

where g_k , for k modes, is a quadratic non-linear function of the time-dependent mode coefficients. b_k are coefficients associated with the control input and f_a is the feedback control input to the cylinder. For the open-loop case $f_a = 0$. For a full state feedback system, the closed loop control input, f_a , is a function of a_k . However, it is not possible to obtain a direct measurement of a_k . An essential aspect of reduced order modeling concerns truncation. How many modes are required and what are the criteria for effective truncation? The answers to this question has been partially addressed by Cohen et al (2003) for the example of the circular cylinder wake control. This effort showed that control of the POD model of the von Kármán vortex street in the wake of a circular cylinder at $Re = 100$ is enabled using just the first mode.

Furthermore, feedback based on the first mode alone suppressed all the other modes in the four mode POD model. At this point, it is imperative to note the difference between the number of modes required to *reconstruct* the flow and the number of modes required for effective low-dimensional modeling for control design. For real-time control, we are interested in estimating only those modes required for closed-loop control. On the other hand, an accurate reconstruction of the velocity field based on a low-dimensional model may be obtained using between 4-8 modes.

A very important lesson learned concerns the validity of the low-dimensional model. Is there an operating envelope wherein the model is valid? How do we find this envelope? The cylinder wake flow can be forced in an open loop fashion using sinusoidal displacement of the cylinder with a given amplitude and frequency. Koopman (1967) investigated the response of the flow to this type of forcing in a wind tunnel experiment. He found a region around the natural vortex shedding frequency where he could achieve “lock-in”, which is characterized by the wake responding to the forcing by establishing a fixed phase relationship with respect to the forcing. The frequency band around the natural vortex shedding frequency for which lock-in may be achieved is amplitude dependent, as shown in Fig. 3.3. Inside the V-shaped area the flow responds to the forcing with a fixed phase relationship, outside the response to the forcing is chaotic.

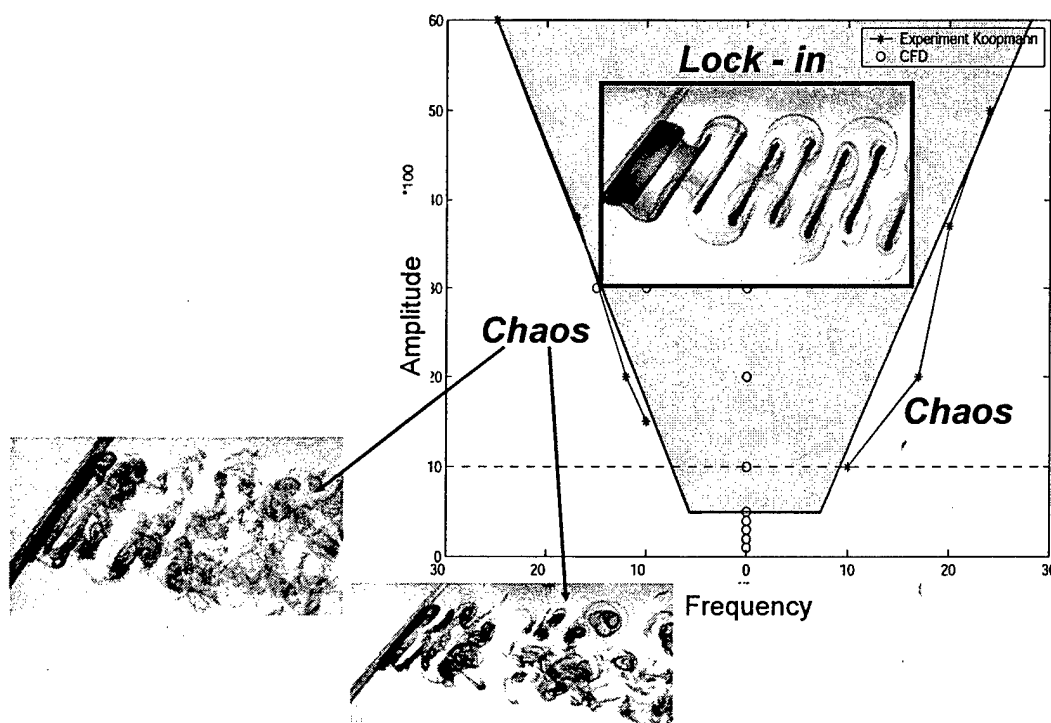


Fig.

3.3: Validity of the Low-dimensional Model



In general, the larger the amplitude, the larger the frequency band for which lock-in is possible. However, a threshold amplitude exists below which the flow will not respond to the forcing any more. In Koopman's experiment, this amplitude was at 10% peak displacement of the cylinder. Shifting the forcing frequency away from the natural shedding frequency yields a qualitatively different behavior, ultimately yielding a chaotic flow behavior at and beyond the lock-in limit according to Koopman (1967). We were able to verify this behavior as shown in Fig. 3.3. The open loop forcing results have important implications for the closed loop feedback control runs. Since our POD model is based on unforced flow field data, it can only capture flow behavior that possesses similar phenomenology when compared to the unforced wake. In terms of the lock-in region, this flow behavior is encountered as long as the controller keeps the flow within the lock-in region. The chaotic behavior at off-natural frequencies is clearly not modeled in the POD modes. Also, more importantly, if the displacement of the cylinder becomes smaller than about 5% of the cylinder diameter, the flow will no longer be responsive to the forcing.

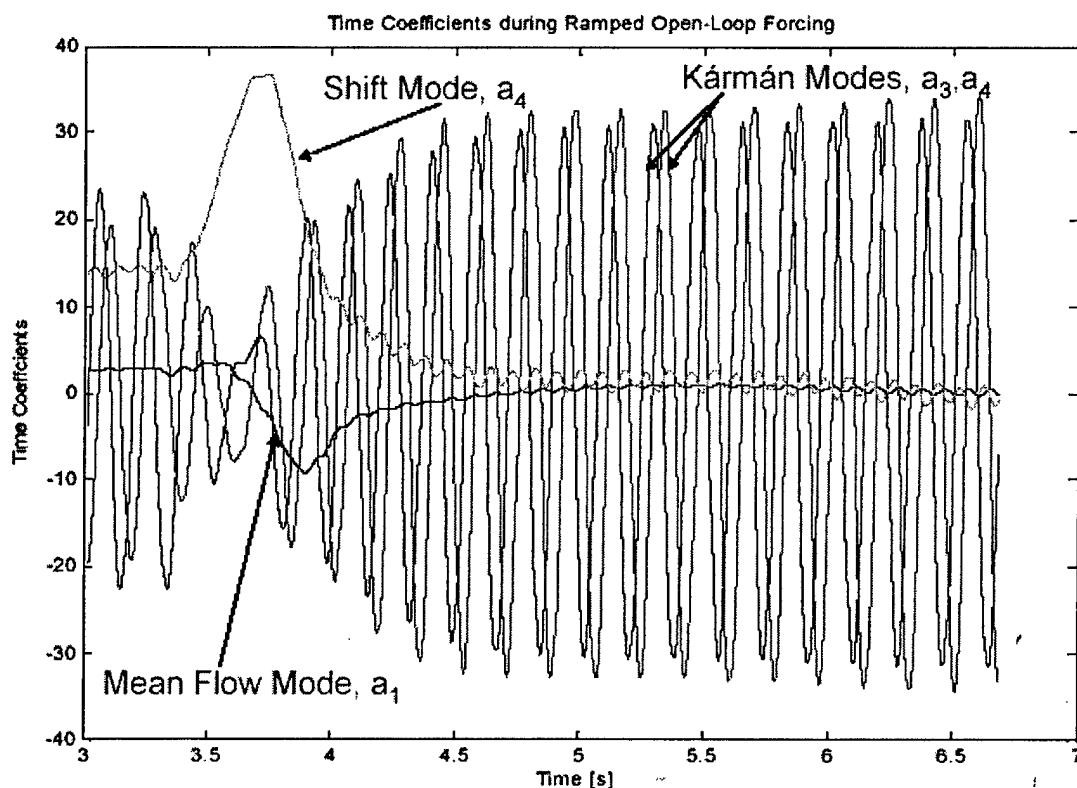


Fig. 3.4: Time depending POD coefficients obtained using transient forcing

In several applications of the POD method for low-dimensional model building the mean flow is removed. Practically speaking, from an ensemble of snapshots, the 'average snapshot' is computed and then this profile is subtracted from each member of the ensemble. This is done mainly for reasons of scale; *i.e.* the deviations from the mean contain information of interest but may be small compared



with the original signal. However, Siegel et al (2003) demonstrated that as the closed-loop controller reduces the unsteady vortex induced drag in the cylinder wake, there is a basic "recovery" of energy in the mean-flow mode. It is important to note that the desire of the closed-loop controller is not to dissipate the unsteady modes alone but to recover the energy expended due to the vortex shedding. Therefore the low-dimensional model should include the mean flow mode. This vital conclusion has also been noted by Siegel et al (2003) used the estimate of this "dynamic" mean flow mode to adapt the phase of a PD (proportional differential) controller applied to the cylinder wake at $Re=100$. By ensuring that the controller was restricted within the operating envelope of the POD model, this approach resulted in a reduction of the vortex induced drag by 90%.

Given the importance of capturing the energy exchange between the mean flow, aperiodic mode, and the unsteady periodic modes, care needs to be taken in selecting an appropriate snapshot ensemble for the POD procedure. If the snapshots are comprised from the steady state regime alone as done often in recent years, then there is an obvious difficulty in capturing the desired transient energy exchange. As an example, consider the cylinder wake problem at $Re=100$. A POD procedure is applied to 500 "snapshots" from steady-state forcing at $d/D=0.2$ and ramping up until $d/D=0.3$. The mean flow (Φ_1) was included in the POD procedure. In addition to the mean flow mode Φ_1 and the von Kármán modes Φ_2 and Φ_3 , a shift mode, Φ_4 was also detected. The energy content of the shift mode is about a fourth of the von Kármán periodic modes. About 99.17% of the entire kinetic energy is contained within the first 4 modes. Once the essential dynamics has been captured, we can go on and obtain the desired set of ordinary differential equations, described in Equation 3. This procedure has been described in detail by Luchtenburg et al (2003).

3.3 Sensor Configuration, Estimation and Observability

The time histories of the temporal coefficients of the POD model are determined by applying the least squares technique to the spatial modes and the unforced flow. The intent of the proposed strategy is that the velocity measurements provided by the sensors are processed by the estimator to provide the estimates of the first two temporal modes. The estimation scheme, based on the linear stochastic estimation procedure introduced by Adrian (1977), predicts the temporal amplitudes of the first four POD modes from a finite set of velocity measurements obtained from the CFD solution of the uncontrolled cylinder wake. For each sensor configuration, velocity measurements, equally spaced at an appropriate time interval, were used. The mode amplitudes, a_1 - a_4 , were mapped onto the extracted sensor signals, u_s , as follows:

$$a_n(t) = \sum_{s=1}^m C_s^n u_s(t) \quad (3.4)$$

where m is the number of sensors and C_s^n represents the coefficients of the linear mapping. The effectiveness of a linear mapping between velocity measurements and POD states has been experimentally validated by Siegel et al. (2004) The coefficients C_s^n ($n=1,2$; $s=1,m$) in Equation (4) are obtained via the linear stochastic estimation method from the set of discrete sensor signals and temporal mode amplitudes.



For the sensor configuration, the effectiveness of the linear stochastic estimation process for the estimation of the first four temporal mode amplitudes, $a_1 - a_4$, is calculated. The quantitative criterion, associated with estimation accuracy, is based on the root mean square (RMS) of the error between the estimated and the extracted mode amplitudes.

The spatial eigenfunctions obtained from the POD procedure provides information concerning the location of areas where modal activity is at its highest. These energetic areas would be the maxima and minima of the spatial eigenfunctions (Cameron et al, 2004). Placing sensors at the energetic maxima and minima of each mode is the basic hypothesis of this effort and the purpose of the CFD simulation is to design a sensor configuration which is later validated using water-tunnel experiments. Location of vorticity maxima/minima of the spatial eigenfunctions are used for sensor placement. A sensor was placed on each the maxima and the minima of modes 1 and 2. On the other hand, for effective estimation, two pairs of sensors each are located on maxima/minima of modes 3 and 4. The estimated versus desired mode amplitude plot, for the above sensor configuration is presented in Fig. 3.5. Furthermore, the details concerning the validity of the measurement equation and conditions for observability are presented in Siegel, Cohen and McLaughlin (2002). The main focus of the work to date of the sensor placement studies has been the usage of a steady-state scenario. However, the development of an observer for real-time estimation of the coefficients during a closed-loop simulation/experiment remains a challenge.

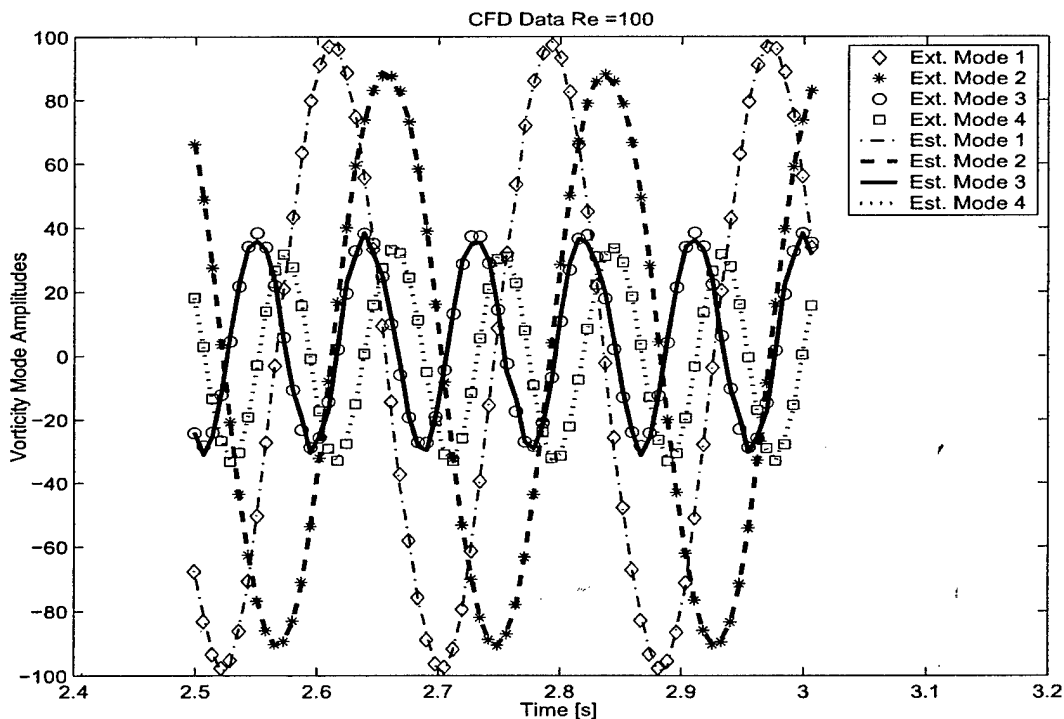


Fig. 3.5: Extracted Mode Amplitudes projected on the estimated ones for CFD data at Re=100



3.4 Controllability, and Stability (COS) Algorithms

Let us examine Equation (3.3). For the origin, $a_k = 0$ as the **desired** equilibrium or fixed point, the aim is to find an appropriate control law for f_a that will make the equilibrium **stable**. The current effort only concentrates on stability issues. The function g_k can be expanded locally as a Taylor series about the desired equilibrium point:

$$\dot{a}_k = g_k(0) + \frac{\partial g_k(0)}{\partial a_j} \cdot a_j + o(|a_k|) + b_k \cdot f_a \quad (3.5)$$

where $o(|a_k|)$ represents higher order terms of the expansion and can be neglected for the stability analysis. For the wake POD model, we observe $g_k(0) \sim 0$. Therefore, the linearization of \dot{a}_k about the desired equilibrium point is:

$$\dot{a}_k = J \cdot a_j + b_K \cdot f_a \quad (3.6)$$

where the Jacobian, J , is:

$$J = \begin{bmatrix} \frac{\partial g_1(0)}{\partial a_1} & \dots & \frac{\partial g_1(0)}{\partial a_M} \\ \dots & \dots & \dots \\ \frac{\partial g_M(0)}{\partial a_1} & \dots & \frac{\partial g_M(0)}{\partial a_M} \end{bmatrix}$$

For nonlinear system given in Equation (3.3), the simplest approach to study controllability is to consider its linearization as described in Equation (3.6).

Definition: The pair (J, B) is state controllable if and only if there exists a control f_a that will transfer any initial state $A_k(t = 0)$ to the desired equilibrium point in finite time.

The following algebraic condition for controllability may be written down for $B = [b_1, b_2, \dots, b_M]$:

$$\text{rank}(B : JB : J^2B : \dots : J^{n-1}B) = n \quad (3.7)$$



The conditions for asymptotic stability can now be stated for linearized models about their equilibrium point, as follows: *For the linearization given in Equation (3.6) if the Jacobian, J_C , has n eigenvalues, each of which has a strictly negative real part, then the equilibrium point is asymptotically stable.*

In addition to conditions for stability, it is also important to make sure that the closed-loop linearized system is hyperbolic. A fixed point of an n th order system is hyperbolic if all the eigenvalues of the linearization (Jacobian) lie off the imaginary axis. The Hartman-Grobman theorem states that the local phase portrait near a hyperbolic fixed point is “topologically equivalent” to the phase portrait of the linearization; in particular the stability type of the fixed point is faithfully captured by the linearization (Cohen, 2004). A linearized system, see Equation (3.6), that is hyperbolic is equivalent in terms of stability and bifurcations, chaos and attractors, equilibria and limit cycles to the nonlinear POD model (see Equation (3.3)). From a practical point of view, let us consider the case when the controller is simply based on proportional control feeding back on the estimate of mode 1 alone, namely:

$$f_a = -K_P \cdot a_1^{est} \quad (3.8)$$

where K_P is the proportional gain of the P controller and a_1^{est} is the estimate of the time-dependent coefficient of Mode 1, a_1 . Inserting the control law in Equation (3.8) into Equation (3.6) yields:

$$\dot{a}_k = J_C \cdot a_j \quad (3.9)$$

where J_C is the “closed-loop” Jacobian and a linear stability analysis based on J_C will provide an insight into the behavior of the closed-loop system:

$$J_C = \begin{bmatrix} \frac{\partial g_1(0)}{\partial A_1} - b_1 \cdot K_P & \dots & \frac{\partial g_1(0)}{\partial A_M} \\ \dots & \dots & \dots \\ \frac{\partial g_M(0)}{\partial A_1} - b_M \cdot K_P & \dots & \frac{\partial g_M(0)}{\partial A_M} \end{bmatrix}$$

Now, it is the aim of the control design to find an appropriate gain, K_P , which will render **all** the eigenvalues of J_C to have a **negative real part**. In addition, the eigenvalues need to lie off the imaginary axis by an adequate margin so that the system is hyperbolic. An illustration of this approach for the cylinder wake problem is detailed in Cohen et al (2003).

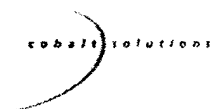


3.5 Important Control Lessons Learned

Table 6.1 summarizes the important lessons learned by the multi-disciplinary research team at the Department of Aeronautics of the Air Force Academy in the context of the cylinder wake problem. These lessons result from the application of a unique suite of simulation and experimental tools development by the team. The path towards meaningful applications of closed-loop control has several obstacles that need to be effectively addressed. These open issues, also listed in Table 6.1, will be continued to be addressed as we proceed towards Phase II.

Description	Lessons Learned	Open Issues
Modeling	<ul style="list-style-type: none"> • Validity of low-dimensional model connected to lock-in phenomena • Energy exchange between aperiodic "mean flow" modes and periodic vortex shedding modes • Snap-shot ensemble to include data reflecting transient forcing 	<ul style="list-style-type: none"> • Evaluate sensitivity of low-dimensional model using transient forcing for Reynolds number effects, and geometrical different bluff bodies
Sensor Placement and Number	<ul style="list-style-type: none"> • Sensor placement may be based on the topology of the spatial Eigenfunctions • Number of sensors required are determined by keeping RMS error of estimated signal within a desired threshold 	<ul style="list-style-type: none"> • Modification of strategy using transient forcing • Modify approach for surface mounted sensors as opposed to sensors in the flow
Observability, Controllability Conditions	<ul style="list-style-type: none"> • Controllability based on the linearization of the state equation • Observability is based on linearized state equation and the measurement equation 	<ul style="list-style-type: none"> • Validate approach using transient forcing model
Estimator	<ul style="list-style-type: none"> • Linear stochastic estimator effectively provides measurement equation from steady-state data 	<ul style="list-style-type: none"> • Modify observer to effectively operate with few sensors in a transient environment
Controller	<ul style="list-style-type: none"> • Feedback is effective when based on primary shedding mode of von Kármán vortex-street • Adaptive strategy, based on the estimation of the "mean-flow" mode incorporated to tune the phase of a Proportional-Differential (PD) controller 	<ul style="list-style-type: none"> • Experimental validation of adaptive controller that provides augmented performance using the US Air Force Academy cylinder wake benchmark

Table 6.1: Control Issues: Summary of Lessons Learned and Open Issues



4. Application I: Circular Cylinder Wake Control

The main portion of this section was accomplished under core AFOSR funding. Nonetheless, the results are pertinent to the toolbox development and approach taken for all three applications. In particular, the feedback control strategy used for the circular cylinder wake was carried on to the D shaped cylinder presented in the next section.

4.1 Circular Cylinder: Introduction

Two-dimensional bluff body wakes have been investigated for quite some time. In a two-dimensional cylinder wake, self-excited oscillations in the form of periodic shedding of vortices are observed above a critical Reynolds number of approximately 47. This behavior is referred to as the von Kármán Vortex Street. According to Williamson, the regime of laminar vortex shedding extends to a Reynolds number of approximately 180, before three-dimensional instabilities occur. This is the Reynolds number regime that we target in this investigation. However, the Kármán vortex street as the fundamental feature of this type of wake flow is sustained to very large Reynolds numbers (on the order of millions). Therefore the lessons learned at low Reynolds numbers will still be applicable to applications of practical interest at much higher Reynolds numbers. Conversely, it would be impossible to control the flow at high Reynolds numbers without being able to successfully do this at low Reynolds numbers.

The non-linear oscillations of the vortex street lead to some undesirable effects associated with unsteady pressures such as fluid-structure interactions and lift/drag fluctuations. Also, the vortices themselves greatly increase the drag of the bluff body, compared to the steady wake that can be observed at lower Reynolds numbers. Monkewitz showed that the von Kármán Vortex Street is the result of an absolute, global instability in the near wake of the cylinder. Further downstream the flow is convectively unstable. This absolute instability is causing the flow to behave as a self sustained oscillator, with internal positive feedback leading to temporal amplification of the oscillation by the recirculation region downstream of the cylinder.

Many attempts to improve the unsteady vortex street have been made. When active open loop forcing of the wake is employed, the vortex shedding in the wake can be locked in phase to the forcing signal. While these findings suggest that the dominant structures in the flow field can be influenced by the forcing, it also strengthens the vortices, and, consequently increases the mean drag as well as unsteady lift fluctuations. Different forcing methods are effective in influencing the behavior of the flow. Acoustic excitation of the wake, longitudinal, lateral or rotational vibration of the cylinder model, and alternate blowing and suction at the separation points have been used. Using these methods, the flow exhibits regions of lock-in and non-lock-in. Koopmann experimentally investigated these regions, and found that the lock-in frequency range depends on the forcing amplitude. The higher the forcing amplitude, the larger the frequency band for which he could achieve lock-in. Additionally, even at the natural vortex shedding frequency, he found a minimum threshold amplitude that was needed for lock-in to occur.



All of these open loop forcing methods have not been shown to reduce the drag, independent of frequency and amplitude employed. The only exceptions are situations where the separation point location is shifted. It should be noted that the geometry of a circular cylinder lends itself to active control methods that target the separation point location of the flow rather than the absolute instability of the wake itself. Using methods like periodic blowing and suction on the cylinder surface in a fashion similar to that employed on the suction side of airfoils, the separation point can be moved aft which in turn will lead to a narrower wake. A narrower wake will exhibit improved stability characteristics, in addition to lower drag due to a lower velocity deficit in and by itself. This effect can be observed in the natural cylinder wake during the "drag crisis", when laminar-turbulent boundary layer transition occurs upstream of the separation point, and the resulting turbulent boundary layer keeps the flow attached longer shifting the separation point downstream. Thus feedback control investigations using periodic blowing and suction like that employed by Min and Choi actually employ two flow control techniques simultaneously, namely separation control and wake stabilization due to feedback. It is difficult if not impossible to judge what portion of the improvement is due to either of these techniques in their simulations.

The only way of suppressing the self-excited flow oscillations without altering the mean flow is by the incorporation of active closed-loop flow control. Traditionally, several fundamentally different approaches to achieve feedback flow control have been employed. The mathematically driven approach to develop a control scheme is hampered by the complexity of the governing Navier Stokes equations. In order to tackle this complexity, one needs to make simplifying assumptions. At this point, the assumptions made in simplifying the equations have often rendered the results inapplicable to real life experiments (Li and Aubry). If no simplifications or assumptions are made, however, the resulting control algorithm (if it can be derived at all with today's computing capabilities) is often too complex to be implemented in real time (Bewley and Trenchea).

On the other hand, approaching the controls problem using an experimental / empirical approach without any modeling of the physics of the flow yields unsatisfactory results also. Experimental studies conducted by Roussopoulos show that a linear proportional feedback control based on a single sensor feedback is able to delay the onset of the wake instability only slightly, rendering the wake stable at Re about 20% higher than the unforced case. Roussopoulos reports that above $Re = 60$, a single-sensor feedback may suppress the original mode but destabilizes one of the other modes. Therefore, better control strategies are needed to stabilize the wake at Reynolds numbers of technical interest.

The solution to this problem lies in the development of a low order model of the flow. The model can be used both for controller development, as well as flow field state estimation. Ideally, it reduces the complexity of the governing Navier Stokes equations to a level that the model can be implemented in real time, while still capturing the important physics of the flow. Gillies pioneered the application of this technique to cylinder wakes by developing a low dimensional model of the cylinder wake at a Reynolds number of 100. Cohen et al. have shown that using this model, the cylinder wake model flow can be successfully controlled using a relatively simple linear control approach based on the most dominant mode only.

The goal of this effort is to apply the approach developed by Cohen et al. to a full Navier Stokes simulation of the flow field. A limited number of sensors placed in the wake are used to estimate the state of the flow which is characterized using a low dimensional model. The controller then acts on the flow state estimates in order to determine the actuator displacement (Figure 4.1 shows the overall setup of this experiment).

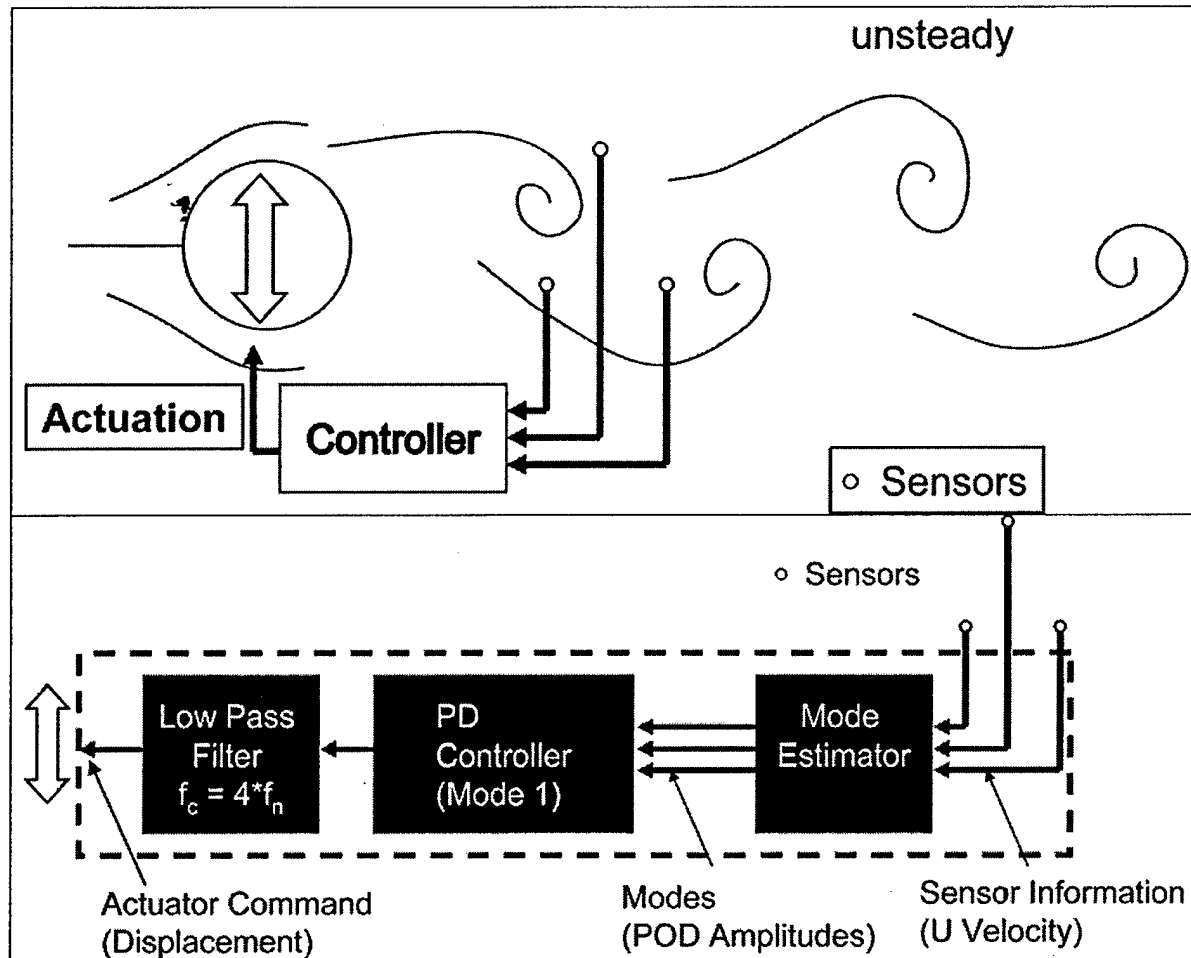


FIGURE 4.1 Feedback Control Setup

4.2 Circular Cylinder: Numerical Methods

CFD Model

For the numerical simulations, Cobalt Solutions' Cobalt solver V.2.02 was used. This code can operate in many different modes using various turbulence models. However, for the present investigation it was used as a direct Navier Stokes solver with second order accuracy in



time and space. Cobalt operates on unstructured grids. For all investigations an unstructured two-dimensional grid with 63700 nodes / 31752 elements was used, see Figure 4.2. The grid extended from -16.9 cylinder diameters to 21.1 cylinder diameters in the x (streamwise) direction, and ± 19.4 cylinder diameters in y (flow normal) direction.

Other pertinent simulation parameters:

- Reynolds Number (Re) = 100
- Mean flow, $U = 34$ m/s
- Damping Coefficients: Advection = 0.01; Diffusion = 0.00
- 32 Iterations for matrix solution scheme
- 3 Newtonian sub-iterations
- Non-dimensional time step $\Delta t^* = \Delta t \cdot U/D = 0.05$
- Time step, $\Delta t = 0.00147$ s
- Vortex shedding frequency 5.55 Hz

The simulation was triggered by skewing the incoming mean flow by $\alpha = 0.5$ degrees in order to introduce an initial perturbation. An important issue concerning the validity of the CFD model needs to be addressed before using the data. A grid and time resolution study showed good convergence for the simulation parameters outlined above. For further validation of the unforced cylinder wake CFD model at $Re = 100$, the resulting value of the mean drag coefficient, c_d , was compared to experimental and computational investigations reported in the literature. At $Re = 100$, experimental data, reported by Oertel and Panton point to c_d values ranging from 1.26 to 1.4. Furthermore, Min and Choi report on several numerical studies that obtained drag coefficients of 1.35 and 1.337. The COBALT CFD model, used in this effort results in a $c_d = 1.35$ at $Re = 100$, which compares well with the reported literature. Another important benchmark parameter is the non-dimensional vortex shedding frequency, the Strouhal number (St) for the unforced cylinder wake. Experimental results at $Re = 100$, presented by Williamson, show Strouhal numbers ranging from 0.163 to 0.166. The Strouhal number obtained from the COBALT CFD model used in this effort is $St = 0.163$ at $Re = 100$, which also compares well.

The simulations were performed on a Beowulf Linux cluster consisting of 64 Pentium III processors operating at 1 Ghz. When running on 8 processors, typically a time step took on the order of 6 s to compute. Employing larger number of processors yielded disproportionately small improvements in execution time, due to network and disk access overhead for saving the results at the end of each time step.

4.3 Circular Cylinder: POD Modeling and Estimation

Feasible real time estimation and control of the cylinder wake may be effectively realized by reducing the model complexity of the cylinder wake as described by the Navier-Stokes equations, using POD techniques. POD, a non-linear model reduction approach is also referred to in the literature as the Karhunen-Loeve expansion. The desired POD model contains an adequate number of modes to enable modeling of the temporal and spatial characteristics of the large-scale coherent structures inherent in the flow.



In this effort, the method of “snapshots” introduced by Sirovich is employed to generate the basis functions of the POD spatial modes from the numerical solution of the Navier-Stokes equations obtained using COBALT. In all 200 snapshots were used, equally spaced 0.00735 s apart. The time between snapshots is five times the simulation time step. The snap-shots were taken after ensuring that the cylinder wake reached steady state. Only the U velocity component (in the direction of the mean flow) was used for POD decomposition in this effort. This decision was made in order to be able to estimate the mode amplitudes based on sensor information, which in future experiments will yield the U and V component of velocity. Since the change in mean flow distribution is an important quantity, we chose the U velocity component over the V velocity component. We found that more than 99.98% of the kinetic energy of the flow lies in the first eight modes, with more than 93.5% in the first four modes. An important aspect of reduced order modeling concerns truncation: how many modes are important and what are the criteria for effective truncation?

The answers to the above questions have been addressed by Cohen et al. This effort showed that control of the POD model, of the von Kármán vortex street in the wake of a circular cylinder at $Re = 100$, is enabled using just the first mode. Furthermore, feedback based on the first mode alone suppressed all the other modes in the four mode POD model, indicating that higher order modes derive from the fundamental modes. In view of this result, truncation of the POD model took place after the first four modes. At this point, it is imperative to note the difference between the number of modes required to reconstruct the flow and the number of modes required to control the flow. In this effort, we are interested in estimating only those modes required for closed-loop control. On the other hand, an accurate reconstruction of the velocity field based on a low-dimensional model may be obtained using between 4-8 modes. The POD algorithm was applied to the fluctuating velocity component in the direction of the flow (u) as described in Equation (1). The decomposition of this component of the velocity field is as follows:

$$\tilde{u}(x, y, t) = U(x, y) + u(x, y, t) \quad (4.1)$$

where U [m/s] denotes the mean flow velocity and u [m/s] is the fluctuating component that may be expanded as:

$$u(x, y, t) = \sum_{k=1}^n a_k(t) \phi_i^{(k)}(x, y) \quad (4.2)$$

where $a_k(t)$ denotes the time-dependent coefficients having units of m/s and $\phi(x, y)$ represent the non-dimensional spatial Eigenfunctions (see Figure 4.3) determined from the POD procedure. Shown are the first four modes of the POD decomposition, plus a 5th mode that was derived by subtracting the mean freestream velocity from the mean flow distribution of the unforced flow field. This mode was found to be necessary to obtain an estimate of the effect of feedback flow



control onto the mean flow. It is being used to both estimate the effectiveness of the controller, as well as allow for gain scheduling to account for changes in the flow receptivity to forcing in a real time fashion. Additionally, Noack et al. have shown that adding a similar mode, which they refer to as the shift mode, accounts for changes in the mean flow. It greatly improves the ability of the model to account for transient effects in the flow field. We will show the correlation between the mean flow mode and the wake drag in the following section.

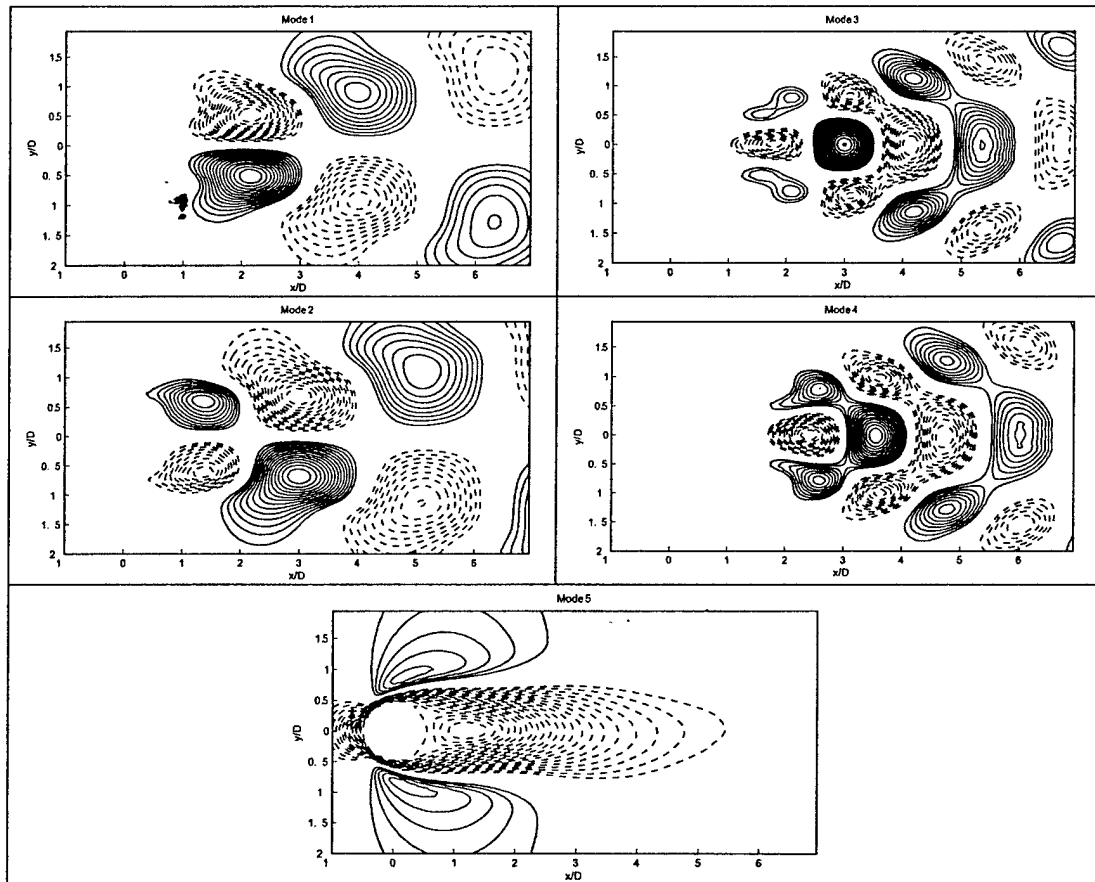


FIGURE 4.3 Eigenfunctions of the 5 Mode POD model based on CFD data at $Re = 100$, using the U velocity component as input for the POD decomposition. Flow from left to right, the cylinder is located at $(0,0)$ and has a diameter of 1

Once the spatial POD eigenfunctions have been derived, the corresponding time-dependent coefficients $a_k(t)$, or mode amplitudes, need to be calculated. For this, two different schemes are reported in literature. Most often a Galerkin projection is used, which involves projecting the spatial eigenfunctions onto the Navier Stokes equations. This process involves spatial derivatives of the snapshots, which are, particularly in the case of experimental data, inherently sensitive to noise. Gillies⁸ used a simple least squares fit, which we found to be much more robust. While we employ the least square fit in the CFD simulations, the experiment will



make use of linear stochastic estimation (LSE) in order to estimate the mode amplitudes in real time. LSE is deterministic in terms of computing time, while least square fitting is not. Thus LSE is a much better choice for real time implementation.

For the feedback controlled runs, the CFD solver writes sensor information at requested (x, y) locations in the flow to a file after calculating a time step, and then waits for an external control algorithm to update the file with the new control command for the next time step. The sensor grid employed for all simulations is shown in Figure 4.2 and employs a total of 35 sensors in the near wake of the cylinder. The main advantage of this sensor grid over others investigated is in its ability to provide a global estimate of the mode amplitudes that shows little error compared to using all grid points. This holds true both for the unforced case as well as the feedback controlled cases. Typical errors are negligible in phase and less than 5 % in amplitude.

While no extensive efforts to optimize the sensor locations was undertaken, we compared a localized uniformly spaced sensor field with 35 sensors between $x/D = 0.75$ and $x/D = 1.75$ to the more widely spaced configuration shown in Figure 4.2. While both grids performed equally well in estimating the unforced flow field, for the feedback control runs the local grid develops large phase and amplitude errors as soon as the flow responds to the forcing. With this finding we decided to use the distributed sensor field shown in Figure 4.2.

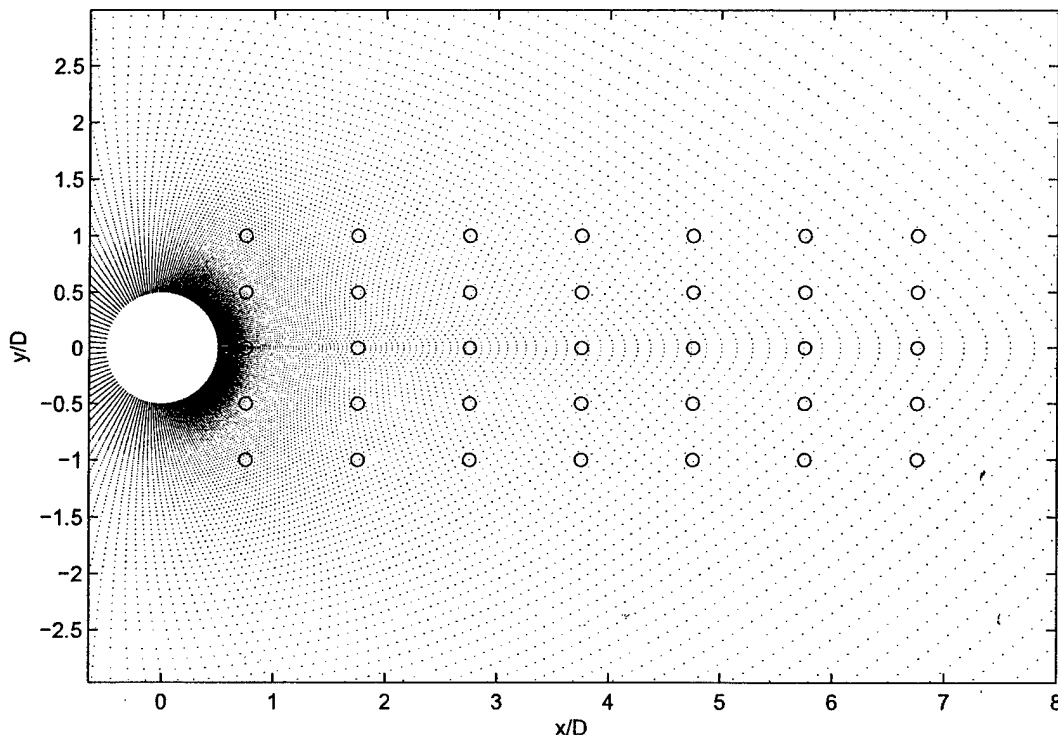


FIGURE 4.2 Computational grid (dots) and sensor locations (circles).



4.4 Circular Cylinder: Controller

Figure 1 shows the controller block diagram. The main components are a Mode estimator, a Proportional and Differential (PD) controller and a low pass filter with a corner frequency of four times the natural shedding frequency. The Cobalt CFD solver has the ability to perform rigid body motion of a given grid. This feature was used to perform both time periodically forced and feedback controlled simulations with one degree of freedom. For all investigations, only displacement of the cylinder in flow normal (y) direction was employed for forcing the flow. The control algorithm acts on the estimate of the Mode 1 amplitude only. This design decision was made based on our earlier investigations controlling a low dimensional model of the flow. For the low dimensional model, proportional gain applied to Mode 1 only was sufficient to suppress vortex shedding. Since our CFD simulations require a filter to avoid feeding back small amounts of noise, we employed a PD feedback control strategy:

$$y_{cyl} = K_p \cdot a_1 + K_d \cdot \frac{da_1}{dt} \quad (4.3)$$

Instead of directly specifying the K_p and K_d gains, these can be expressed in terms of an overall gain K and a phase advance ϕ :

$$\begin{aligned} K_p &= K \cdot \cos(\phi) \\ K_d &= \frac{K \cdot \sin(\phi)}{2\pi f} \end{aligned} \quad (4.4)$$

With f being the natural vortex shedding frequency.

Physically, the control algorithm was implemented in Matlab on a separate PC running Windows. It interfaced to the Beowulf cluster running Cobalt using Windows file sharing through Samba, to read the sensor information and update the cylinder displacement.

4.5 Circular Cylinder: Results

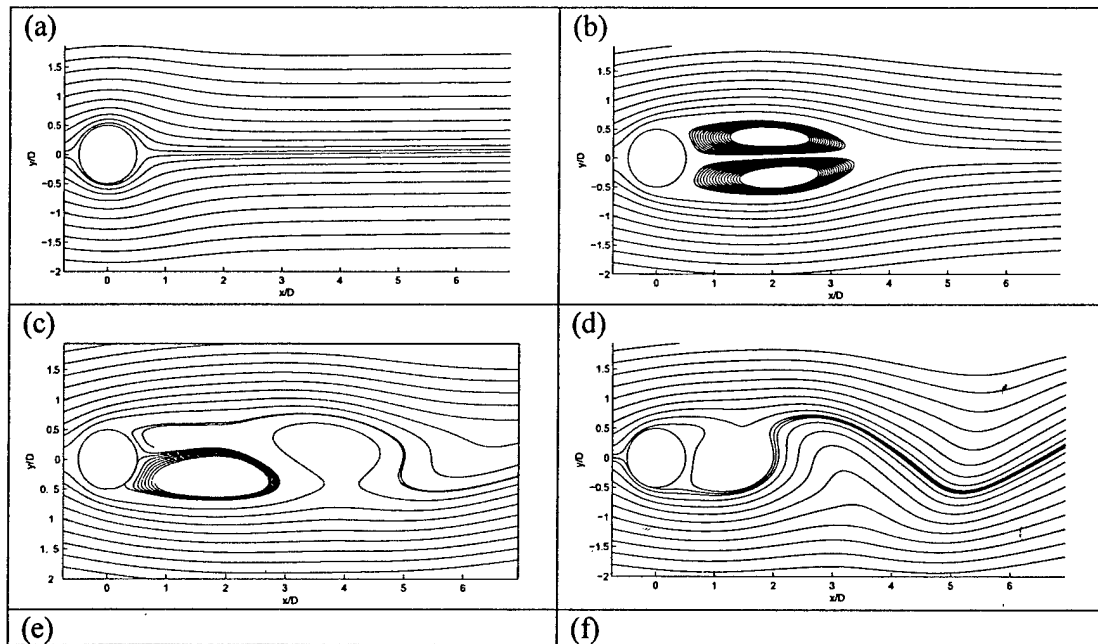
Before closed loop feedback flow control is employed, it is important to investigate the dynamics of the unforced flow field in detail. Equally important, the effect of open loop forcing needs to be understood, since the receptivity of the flow to forcing will manifest itself in these investigations. The following section will outline the results of these investigations, and also show the limitations of the type of forcing employed as well as the limits of the flow improvements that may be obtained using feedback control.

The following two sections will highlight a few select cases of the unforced flow, open loop forced flow and feedback controlled flow. Two different kinds of feedback control were employed, one using a fixed set of proportional and differential gains, and one set where the gains were varied depending on the change in the mean flow. The latter is usually referred to as a gain scheduling scheme.



Unforced Wake Properties

In a CFD simulation, the flow field is started abruptly at time zero. Figure 4.4 shows the evolution of the flow field after this startup. The flow evolves from a Stokes-type streamline pattern at $t = 0$ s (Figure 4.4 (a)) through a steady wake with two closed recirculation bubbles at $t = 0.4$ s (Figure 4.4 (b)) into the steady state showing the unsteady von Kármán Vortex Street at $t = 2.94$ s (Figure 4.4 (d)). During this startup, the flow reaches a state of minimum drag at $t = 0.7$ s (Figure 4.4 (c)). This minimum drag coincides with a maximum amplitude of mode 5 (the free stream mode) as well as a maximum mean recirculation zone length with the downstream end of the recirculation zone located at $x/D = 5.4$ (not depicted). It is worth noting that the minimum drag does not coincide in time with the steady wake as one might expect, but rather with a vortex shedding pattern with a very large wavelength, as shown in Figure 4.4 (c). The total drag in this situation is about 16 % less than in the steady state vortex shedding situation. Thus one may argue that a feedback control scheme aiming to suppress the vortex shedding may be able to recover up to this portion of the total drag, at best. We refer to this 16% portion of the overall drag force as the *vortex induced drag*, since it is caused by the vortex shedding in the unsteady wake flow. It is a portion of the pressure drag. About 2 seconds after the startup of the simulation, the wake approaches a time periodic vortex shedding state. The mean recirculation zone ends at $x/D = 1.9$ in this final flow state.



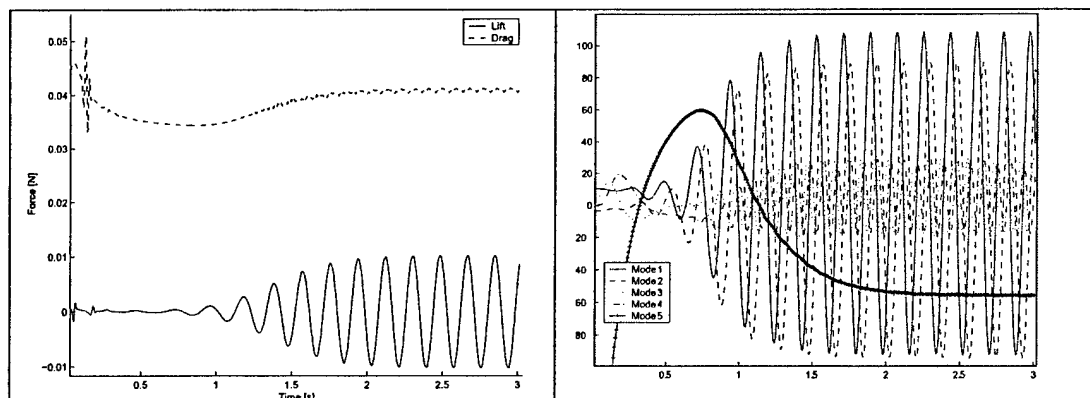


FIGURE 4.4 (a)-(d) Instantaneous streamlines at $t = 0.0, 0.4, 0.7$ and 3.0 seconds after startup of the simulation. (e) lift and drag during startup of the simulation. (f) Mode amplitudes during startup of the simulation, for spatial mode distributions see Figure 3.

Open Loop Forced Wake Properties

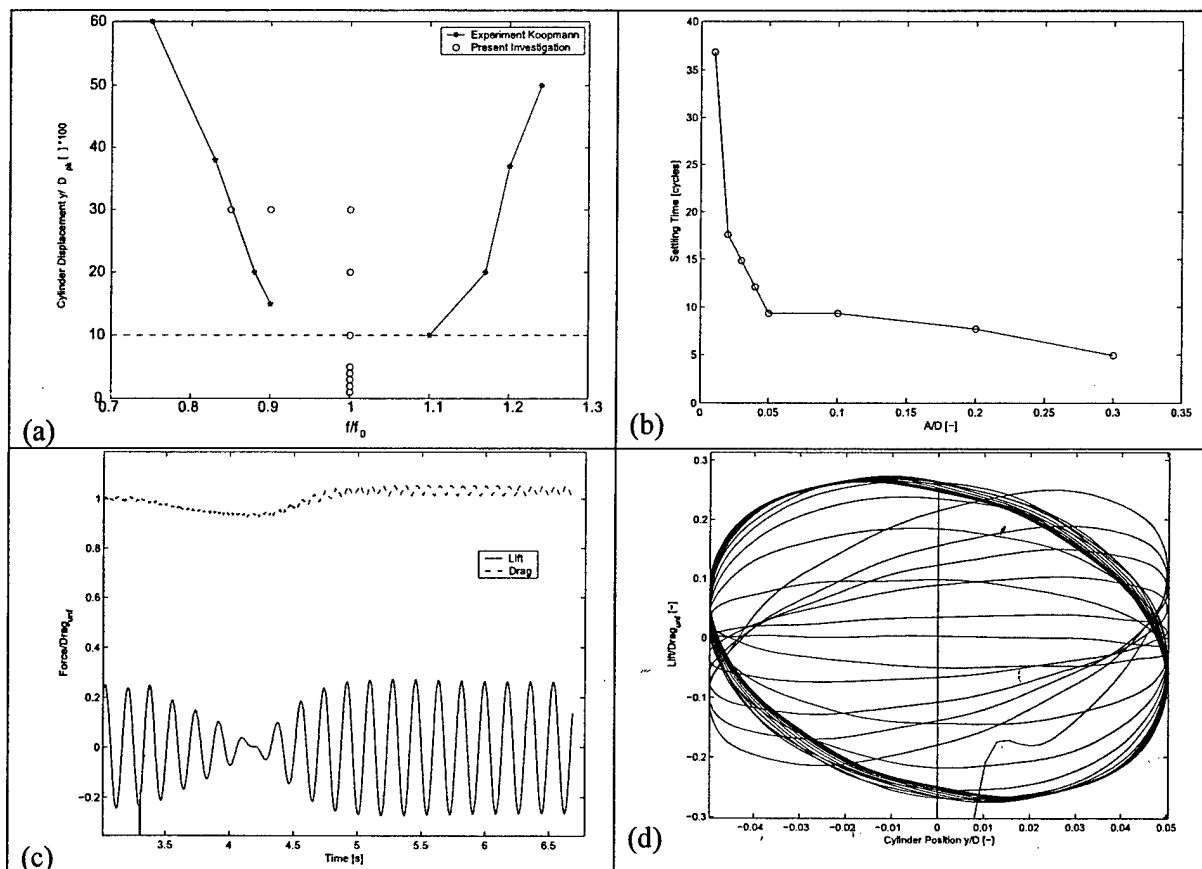
The cylinder wake flow can be forced in an open loop fashion using sinusoidal displacement of the cylinder with a given amplitude and frequency. Koopman investigated the response of the flow to this type of forcing in a wind tunnel experiment. He found a region around the natural vortex shedding frequency where he could achieve “lock-in”, which is characterized by the wake responding to the forcing by establishing a fixed phase relationship with respect to the forcing. The frequency band around the natural vortex shedding frequency f_0 for which lock-in may be achieved is amplitude dependent, as shown in Figure 4.5(a). Inside the V-shaped area the flow responds to the forcing with a fixed phase relationship, with the vortex shedding in phase with the forcing. Outside, the response to forcing is chaotic. In general, the larger the amplitude, the larger the frequency band for which lock-in is possible. However, a threshold amplitude exists below which the flow will not respond to the forcing any more. In Koopman’s experiment, this amplitude was at 10% peak displacement of the cylinder.

We resampled the lock-in region in the CFD simulation at select amplitude and frequency pairs shown in Figure 4.5(a). The simulations activated the forcing always at the same time, 3.3 seconds after the start of the simulation, which resulted in the forcing being 180 degrees out of phase with the vortex shedding. A typical run resulting in lock-in is depicted in Figure 4.5(c) and 4.5(d). Figure 4.5(c) shows that the flow field goes through a transient phase before lock-in is achieved after about 9 shedding cycles. After the transient, a fixed phase relationship between forcing and the unsteady lift force induced by the vortex shedding is established, as shown in Figure 4.5(d). We refer to the time during which the flow adjusts to the forcing as the settling time. For comparison, Figure 4.5(e) and 4.5(f) show the chaotic response of the flow to a forcing input characterized by a frequency / amplitude combination just outside the lock-in range. The flow does not establish a fixed phase relationship to the forcing in that case. A scan through different forcing amplitudes was performed at the natural shedding frequency ($f/f_0 = 1$) with amplitudes ranging from 1 to 30 % of the cylinder diameter. The settling times observed in these cases are shown in Figure 4.5(b). While the settling times are roughly constant for forcing



amplitudes between 5 and 10%, for smaller amplitudes a drastic increase in settling times can be observed. This manifests the behavior observed by Koopman around 10% forcing amplitude, albeit shifted towards somewhat smaller amplitudes. There are two possible explanations for this. Koopman used spanwise coherence as an indicator for lock-in, which may occur at larger amplitudes than the local lock-in observed in our two-dimensional simulations. Additionally, his experiment was conducted in a wind tunnel environment which features more mean flow turbulence than the CFD simulations. This would also tend to increase the amount of forcing needed to overcome the turbulence and achieve lock-in.

The open loop forcing results have important implications for the closed loop feedback control runs. Since our POD model is based on unforced flow field data, it can only capture flow behavior that is phenomenologically similar to the unforced wake. In terms of the lock-in region, this flow behavior is encountered as long as the controller keeps the flow within the lock-in region. The chaotic behavior at off-natural frequencies is clearly not modeled in the POD modes. Also, more importantly, if the displacement of the cylinder becomes smaller than about 5% of the cylinder diameter, the flow will no longer be responsive to the forcing.



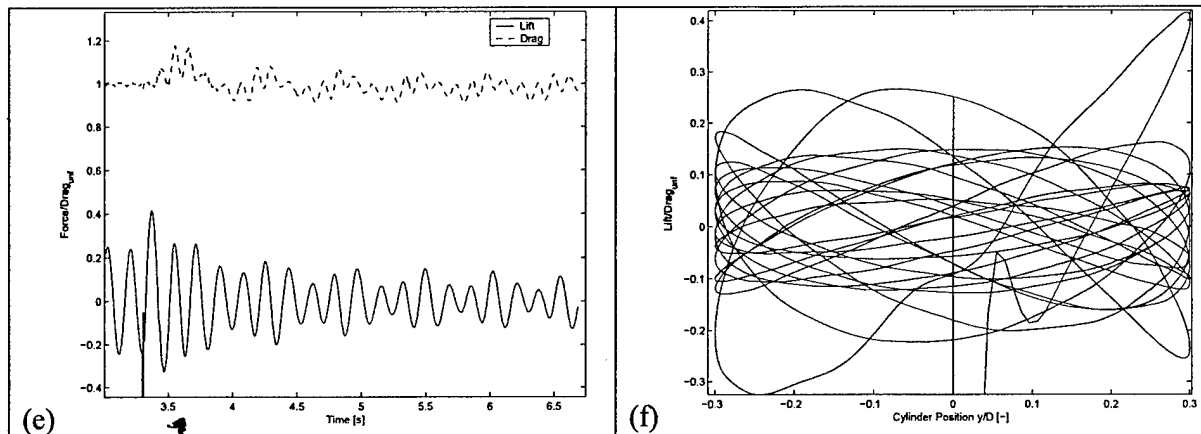


FIGURE 4.5 (a) Lock-in region adapted from Koopman (1966) (b) Settling time for different forcing amplitudes using sinusoidal forcing at the natural shedding frequency. (c-d) Sinusoidal forcing at the natural frequency using an amplitude of 5% of the cylinder diameter (c) Lift and Drag (d) Phase plot no dimensional lift force vs. cylinder motion. (e-f) Sinusoidal forcing at 75% of the natural frequency using an amplitude of 30% of the cylinder diameter (e) Lift and Drag (f) Phase plot lift vs. cylinder motion.

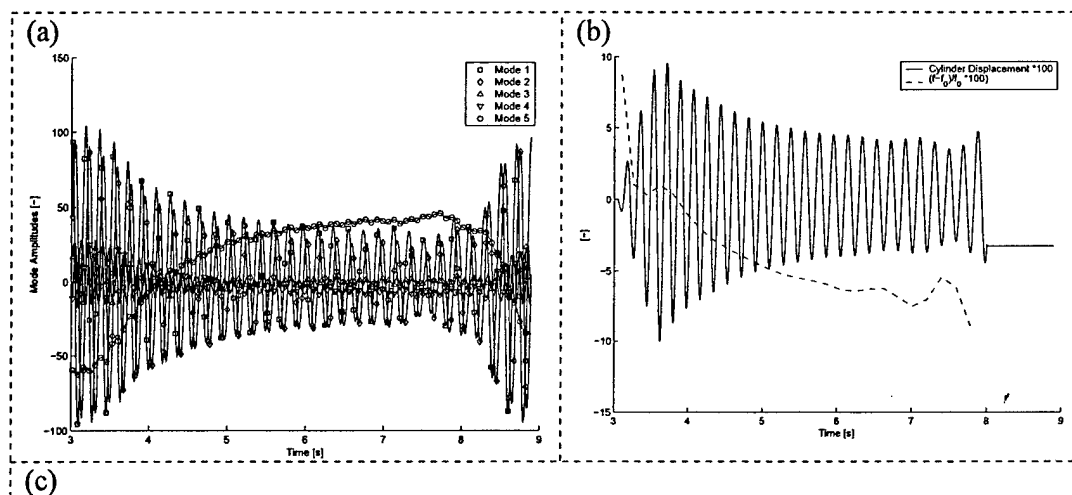
Fixed Phase Feedback

A series of simulations with different phase advance ϕ were conducted. The overall gain K was kept constant at a value that resulted in initial displacements of less than 15% of the cylinder diameter, in order to avoid strongly nonlinear effects that have been reported in literature at higher amplitudes. Qualitatively, the runs resulted in either an increase or decrease of the mode amplitudes. A case with a decrease in mode amplitudes is shown in Figure 4.6. During the control run, the global mode amplitude of Mode 1 decreases from a peak value of around 100 to a peak value of less than 40. This decrease in mode amplitude does not just apply to Mode 1, but also to Mode 2 and the two higher order modes. These findings are consistent with our experience in controlling a low order model of the flow¹², where a similar coupling between the modes could be observed. Considering the behavior of the unsteady lift and the drag, a reduction in drag of about 14% of the unforced drag was observed, while the unsteady lift was reduced by about 50%. Comparing the drag reduction of 14% to the minimum drag encountered during startup of the CFD simulation, which is 16% less than the drag of the unforced flow field, we find that the simple feedback controller with a fixed gain and phase recovers more than 87% of the steady wake flow drag reduction. However, all of the fixed phase simulations that led to a drag reduction were not able to stabilize the flow at a low drag value. In Figure 4.6(a) at a time of 7.5 s, a reduction followed by an increase in mode amplitude can be observed. This is the first indication of the onset of an instability that will ultimately render the flow field chaotic, if the simulation is continued. Inspecting the cylinder displacement during this simulation (Figure 4.6(b)), the onset of the instability coincides with a cylinder displacement that has just dropped below 5% of the cylinder diameter. Thus the onset of the instability coincides with the loss of



flow response found in the periodically open loop forced runs discussed in the previous section. The instantaneous vorticity contours shown in Figure 4.6(c) show a wake flow where the vortices form further downstream of the cylinder, compared to the streamlines of the unforced flow shown in Figure 4.4(d). In the unforced flow, the vortices roll up between 1 and 2 diameters downstream of the cylinder, while in the feedback controlled situation the rollup occurs between 3 and 4 diameters downstream. As a result the reverse flow region is lengthened, from $x/D = 1.9$ in the unforced case to $x/D = 4.3$. Simultaneously with the lengthening of the recirculation zone we observe a reduction in the vortex shedding frequency. The correlation between the shedding frequency and the reduction in drag is in qualitative agreement with the wake model proposed by Ahlborn et al.

A summary of the effect of different amounts of fixed phase advance between mode 1 and the cylinder motion on both the mode amplitudes and the drag force is shown in Figure 4.7. While it is apparent that the largest drag and mode amplitude reductions are achieved for a phase advance of about 35 degrees, this phase advance is also unstable over longer time periods. The good correlation between the mode amplitude reduction and the drag reduction suggests a strong link between these quantities. Also, it can be seen that all mode amplitudes experience a proportional reduction which shows the coupling between the modes to be strong. It is also interesting to note that a zero degree phase advance has no impact on the drag.



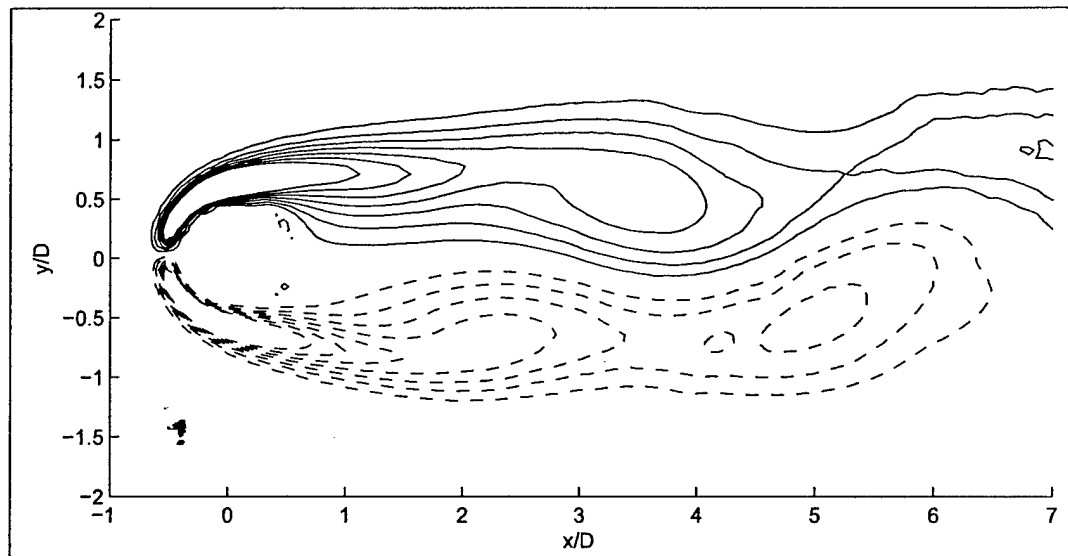


FIGURE 4.6 Linear feedback of Mode 1 with 30° Phase advance. The controller is activated at 3.03 s and deactivated at 8 s. (a) Mode Amplitudes (b) Cylinder Displacement and Frequency (c) Instantaneous Vorticity Contours at $t = 6.5$ s

With these findings on the impact of fixed phase feedback on the wake, an important question to be asked is if the wake can be stabilized at a low mode amplitude, and if so, how? An obvious parameter to adjust in order to achieve this is the gain of the controller. Increasing the gain leads to larger cylinder displacements, which would assure the ability to control the wake at small mode amplitudes. However, we found that larger gains do not stabilize the wake but rather lead to a low frequency oscillation and instability even when the cylinder displacements are kept above 5% of the cylinder diameter. The other parameter to be considered for adjustment is the phase of the feedback which we report on in the following section.

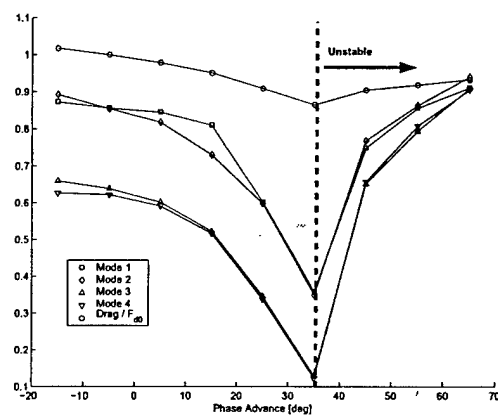


FIGURE 4.7 Mode amplitudes and drag force for various phase advance angles.



Variable Phase Feedback

During an investigation into different sensor configurations, we used a sensor field with 35 sensors localized between $x/D = 0.75$ and $x/D = 1.75$. As was later discovered, this sensor field developed a large estimation error with respect to the phase error of the Mode 1 estimate, relative to an estimate based on the entire flow field, as shown in Figure 4.8 (f). Despite this phase error the wake stabilized at an overall drag reduction of about 15% with an unsteady lift amplitude reduction of 90% (Figure 4.8(c)), compared to the unforced flow field. Inspecting the phase error, one can see that due to the effects of the local sensor field the phase advance is reduced to almost zero in the steady state case. This phase advance angle stabilizes the flow field at a low level of vortex shedding, with the recirculation length extended to $x/D = 3.95$, or more than twice the unforced length. The phase plot in Figure 4.8(d) demonstrates that the wake develops a new limit cycle at a reduced mode 1 amplitude in the steady state stabilized case. The vorticity plot in Figure 4.8(e) is very similar to the fixed phase feedback vorticity distribution shown in Figure 4.6(c). The recirculation zone is clearly lengthened in the stabilized flow, which leads to a decrease in the vortex shedding frequency by 23% (Figure 4.8(b)).

While in the run shown in Figure 4.8 the phase advance was a result of the dense localized sensor placement, the same effect can be achieved using a global sensor field like the one shown in Figure 4.2 in combination with a variable phase advance based on the non-fluctuating mode 5. Thus we find that a variable gain strategy that adjusts the feedback gains according to the change in the mean flow achieves better results than a fixed gain control approach. The success of the variable gain strategy is a logical result given that the initial feedback gain and phase are based on the non-controlled flow field and recirculation length.

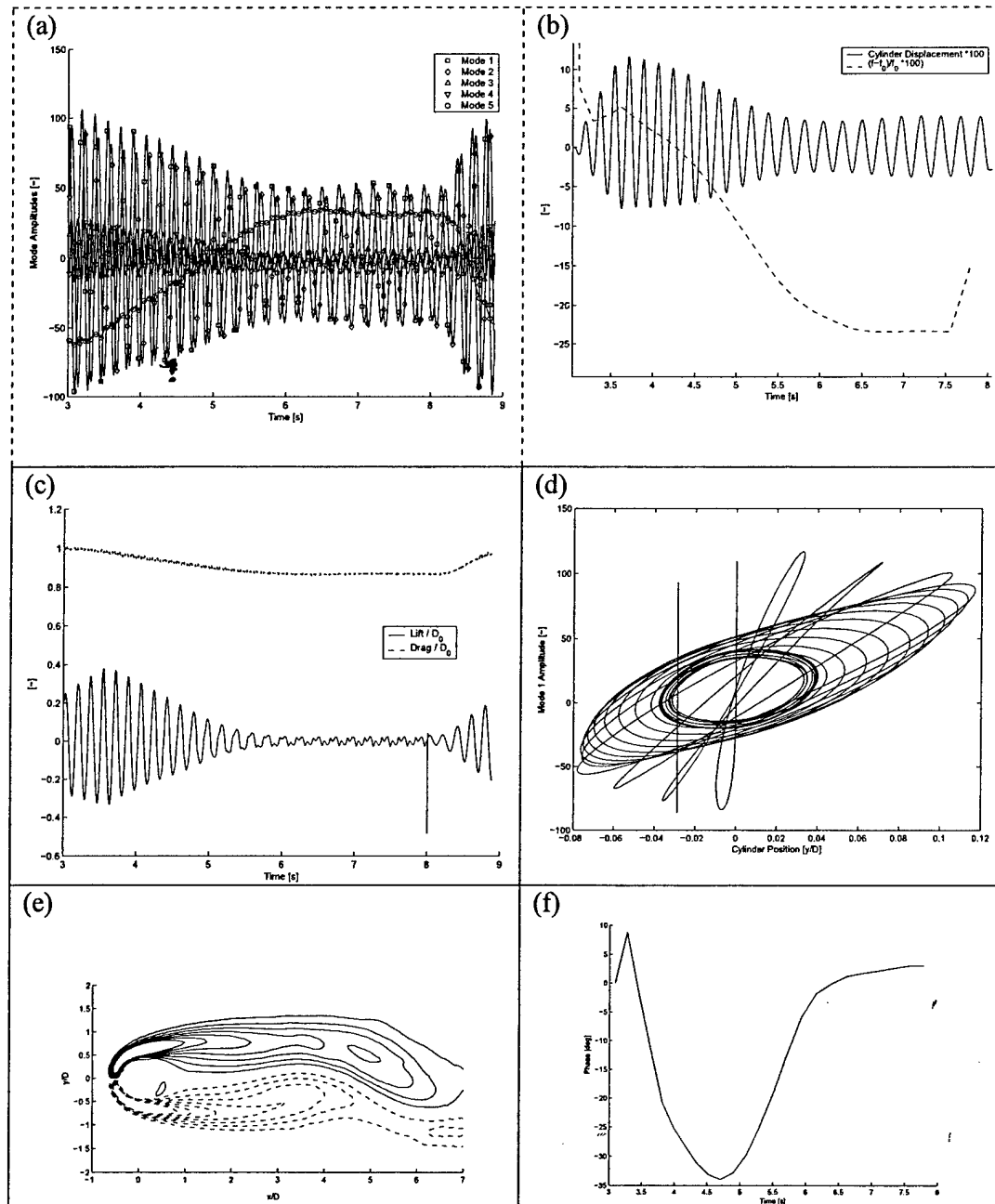


FIGURE 4.8 Linear feedback of Mode 1 with variable Phase advance. (a) Mode Amplitudes (b) Cylinder Displacement and Frequency (c) Lift and Drag (d) Phase between Cylinder Position and Mode 1 (e) Instantaneous Vorticity Contours at $t=7.5$ s (f) Phase advance during the run



The drag and unsteady lift force reduction manifests itself in a change in the mean flow, as well as the RMS distribution. Figure 4.9 compares the unforced mean flow and RMS distributions to those encountered in the stabilized state, between 6 and 8 seconds, in the feedback controlled run. The recirculation zone length has almost doubled in length, and the peak in the RMS distribution is shifted from $x/D=2.5$ to $x/D = 5$. Also, it can be seen that the controlled wake up to 3 diameters downstream of the cylinder is entirely steady.

When applying feedback control, significant changes in the mean flow field occur, as shown in the previous section. It is therefore of interest to investigate how the stability characteristics of the mean flow are modified as a result of the mean flow changes. Linear stability analysis based on numerical solution of the Orr-Sommerfeld equations using spectral methods (Trefelthen) was used to analyze these changes. Figure 4.10 compares the maximum growth rate of the unforced flow field at a Reynolds number of 100 to the steady state feedback controlled flow field (Run 122). Despite the fact that the near wake fluctuations are suppressed by the feedback as shown in the previous section, the flow field has become more unstable beyond two diameters downstream of the cylinder. Comparing the unforced flow to a stable flow field at a subcritical Reynolds number of 40, one can see that the Karman vortex street at $Re = 100$ leads to a more stable flow field beyond $x/D = 3$.

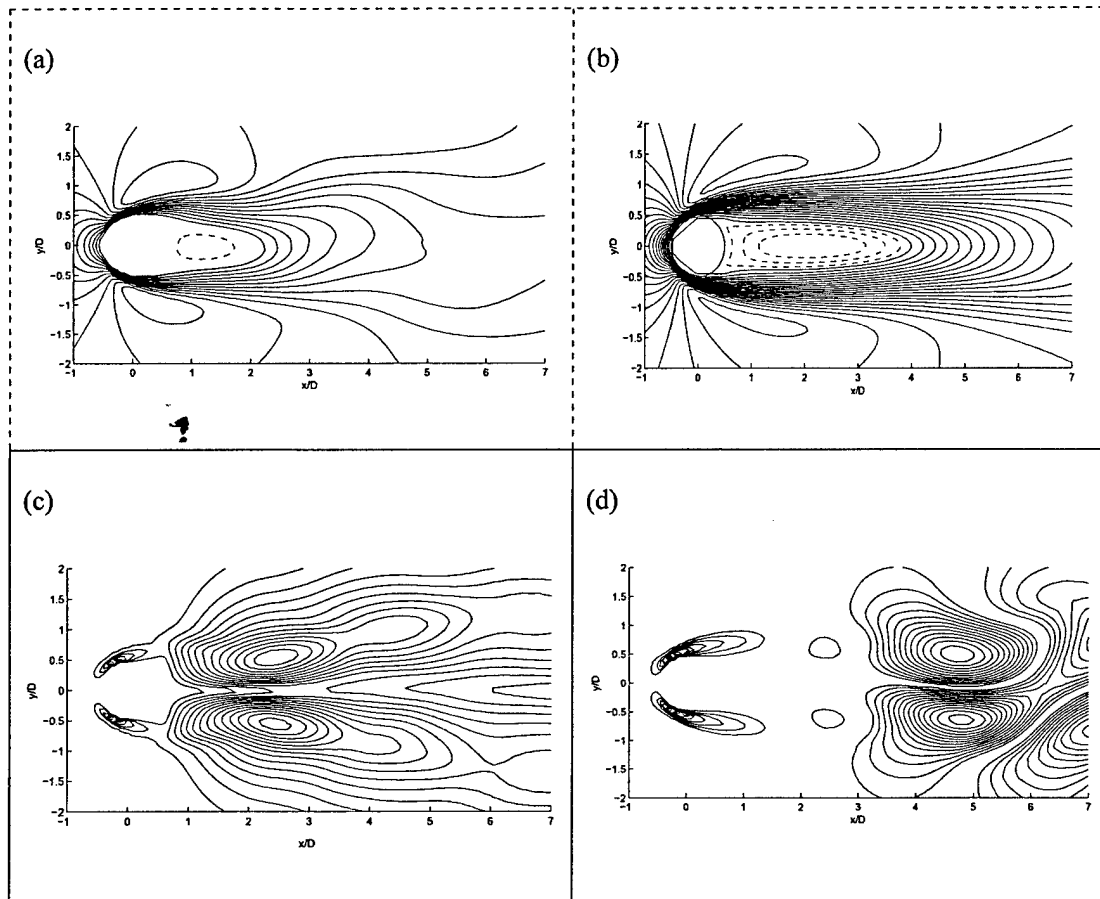


FIGURE 4.9 Mean flow (a,b) and RMS velocity distributions (c,d). Left, uncontrolled, right, controlled case. The cylinder is centered at (0,0) and of diameter 1, flow from left to right. Negative isocontours are dashed, positive isocontours are solid lines.

Discussion

We used Proper Orthogonal Decomposition (POD) as a tool to process multiple sensor signals into a global estimate of the flow state. POD allows for stable global wake state estimation, enables multi sensor evaluation and eliminates artifacts of local sensing, i.e. sensing at nodes of the vortex street. It also allows for an accurate state estimate when the effect of the controller causes major changes both in the mean flow and the rms amplitudes of the fluctuating velocity components. However, we find it necessary to account for the changes in the mean flow by adding a mean flow mode (mode 5) to the model.

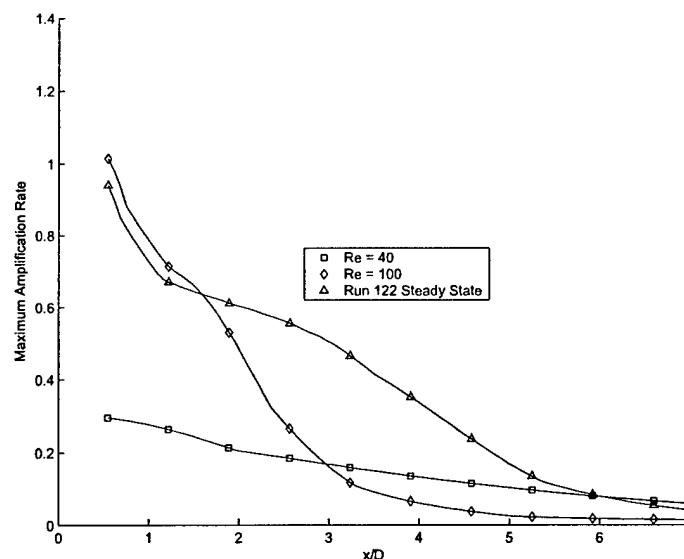
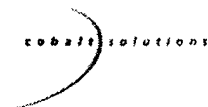


Figure 4.10 Linear stability analysis of unforced and feedback controlled flow fields

While we used only Mode 1 for closing the feedback loop, all the higher order POD modes experienced proportional reductions in mode amplitude. This suggests a strong coupling between all modes, and implies that the existence of the higher order modes is conditional on the presence of the fundamental modes. This confirms the results of our previous work.

While feedback control was able to stabilize the near wake of the cylinder, vortex formation still occurred, though further downstream. While the reasons for this are not entirely clear, we suggest several possible causes. The change in the mean flow caused by the controller lengthens the recirculation zone. This moves the vortex formation location further downstream and causes a reduction in both drag and rms lift force. While both of these effects are desired, the downstream shift in vortex formation location causes a larger spatial separation between the actuation, which remains at the cylinder, and the oscillations the actuator attempts to cancel. This requires both more actuation input, and also an adjustment in the actuation phase in order to account for the time a given disturbance takes to travel from the actuator to the vortex formation location. At the same time the disturbances caused by the actuator need to travel through a region of the flow which, while stabilized, is only stabilized within a narrow range of phase angles. If the far wake requires a phase angle for stabilization that at the same time destabilizes the near wake, a physical limit has been reached in terms of what can be achieved given the actuator location. This effect may limit the spatial range for which stabilization can be achieved with the current actuator setup. This is particularly true since the vortex suppression achieved in this investigation decreases the stability of the feedback controlled flow field and extends the unstable region of the flow further downstream of the cylinder, as was demonstrated by the linear stability investigations shown in the previous section.

Despite all these problems, we were able to suppress the oscillations in the near wake without actively modifying the mean flow or changing the separation point using, for example, momentum injection. Thus this effort shows that the cylinder wake flow can be improved in



terms of drag and unsteady lift by feedback control. For this reason, one would expect the current control approach to be applicable to wake flows with fixed separation points, like the flow around a D- shaped cylinder. The same cannot be said for approaches that aim at moving the separation point aft, for example by tripping the boundary layer or using blowing and suction upstream of the separation point to delay separation.

In parallel with this paper, Gerhard et al. also employ a low order model based approach to control the circular cylinder wake. While details of the low order model, estimation technique and control algorithm employed are different from our approach, the qualitative effects of the control on the flow field appear to be very similar. This indicates that the limitations encountered in both of our control approaches may be inherent to actuation authority - both approaches use a localized actuation in a small portion of the flow field - and inherent to the physics of the flow field itself.

Overall, we were able to reduce the effect of vortex shedding on both the unsteady lift and the vortex induced portion of the pressure drag by about an order of magnitude.

4.6 Circular Cylinder: 3-D High Reynolds Number Baseline CFD

Circular Cylinder calculations at a subcritical Reynolds number of 3900 have been conducted by Hansen and Forsythe (2003). Although this work was not performed as part of this STTR, it is included (briefly) in this report since it forms the baseline for similar calculations of the "D"-shaped cylinder and NACA 0015. A comprehensive set of experiments and other computations are available at this Reynolds number and were used for validation of the solution method. At this Reynolds number, the boundary layers are laminar, and the shear layers transition to turbulent in the wake. For the computations, Large Eddy Simulation (LES) was applied with no explicit subgrid scale model. This means that the numerical dissipation of the solver was used to model the subgrid scale stresses. LES was used rather than DES since at this Reynolds number the boundary layers are laminar, so a hybrid RANS/LES method such as DES holds no advantage over LES. LES assumes sufficient grid resolution to resolve the large scale energy containing eddies. A large part of the study was a comprehensive grid refinement study to determine the necessary grid resolution. Starting from a baseline grid, two other grids were created. Each grid refinement was achieved by increasing the cell density by a factor of $\sqrt{2}$ in each coordinate direction, resulting in volume cell counts of 442,018, 1,230,710, and 3,258,000, for grids A, B, and C, respectively. The effect of grid refinement on the flow is shown in Figure 4.11, with increasing grid resolution resolving more structure.



Figure 4.11. Top and side views of isosurfaces of non-dimensional spanwise velocity perturbations $v'/U_{\infty} = \pm 0.2$. Red shows the positive valued isosurfaces. Grid A results are on top, grid B results are below.

Figure 4.12 shows the coefficient of pressure on the cylinder surface for the different grids used. The experimental data of Norberg (1987) at $Re=3000$ and $Re=4020$ provide pressure data over the entire surface. Only the coefficient of backpressure (C_p at $\theta=180$) is available for $Re=3900$. The grid C results match very closely with the $Re=3000$ experiment, particularly beyond 78 degrees. The actual $Re=3900$ pressure coefficient line is judged to lie somewhere close to midway between the grid B and grid C results based on the $Re=3900$ base pressure coefficient. Both grids B and C seem to be of sufficient resolution, while grid A is clearly under-resolved.

Hansen and Forsythe (2003) also examined wake statistics such as mean centerline velocity and Reynolds stresses, and for the two finer grid there was good agreement with the experiments.

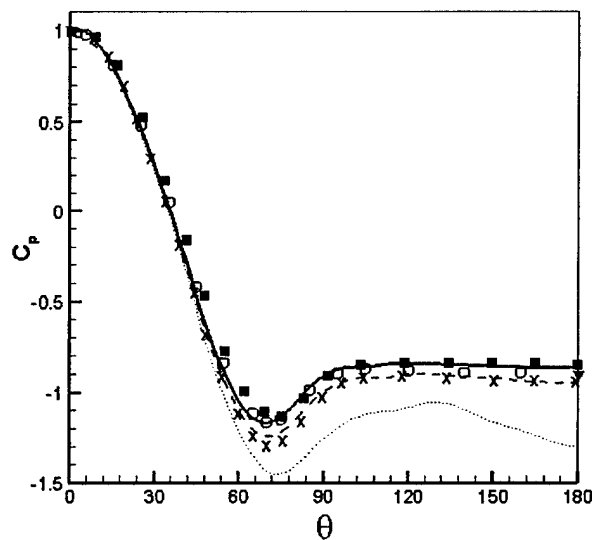
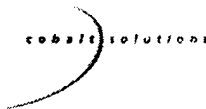


Figure 4.12. Cylinder Surface Coefficient of Pressure. Experiment is from Norberg .
 grid A; --- grid B; — grid C; X Tremblay (2000) DNS; ■ experiment, Re= 3000;
 ▼ experiment, Re=3900; O experiment, Re = 4020.

4.7 Summary

The effect of feedback flow control on the wake of a circular cylinder at a Reynolds number of 100 is investigated in direct numerical simulation. Our control approach uses a low dimensional model based on proper orthogonal decomposition (POD). The controller applies linear proportional and differential feedback to the estimate of the first POD mode. The range of validity of the POD model is explored in detail. Actuation is implemented as displacement of the cylinder normal to the flow. We demonstrate that the threshold peak amplitude below which the control actuation ceases to be effective is in the order of 5% of the cylinder diameter.

The closed loop feedback simulations explore the effect of both fixed phase and variable phase feedback on the wake. While fixed phase feedback is effective in reducing drag and unsteady lift, it fails to stabilize this state once the low drag state has been reached. Variable phase feedback, however, achieves the same drag and unsteady lift reductions while being able to stabilize the flow in the low drag state. In the low drag state, the near wake is entirely steady, while the far wake exhibits vortex shedding at a reduced intensity. We achieved a drag reduction of 15% of the drag, and lowered the unsteady lift force by 90%. 3-D calculations at a higher Reynolds number have been performed and validated, and are available for subsequent control attempts in phase II.



5. Application II: "D" Shaped Cylinder Wake Control

5.1 "D" Shaped Cylinder: Application Background

In order to demonstrate the applicability of the toolbox to new flow geometries, the D shaped cylinder geometry was considered. The main motivation to include the D-shaped cylinder in the AFC project is because it has a fixed separation point. This means that the only way to suppress the vortex shedding is by means of controlling the absolute instability of the wake and *not* by moving the separation point. Additionally, due to the fixed separation point this geometry is an excellent test bed for demonstrating actuation using a blowing and suction slot.

CFD computations have been performed on a grid developed for the "D" shaped cylinder. While we initially used a Reynolds number of 150 to make sure that the flow is two-dimensional and laminar, we found that due to the thick boundary layers the D shaped cylinder flow was much more stable than the circular cylinder flow at the same Reynolds number. This extends the computation times for both open loop forced and feedback controlled simulations. A flow visualization study in the water tunnel revealed that the critical Reynolds number for 2D to 3D transition of the D cylinder flow is in the order of 380.

For the above reasons, it was decided to increase the Reynolds number to 300 for the investigation of the open loop forced and future closed loop simulations. Figure 5.0 compares the two different Reynolds numbers. It can be seen that the higher Reynolds number establishes a limit cycle vortex shedding within fewer cycles. This speeds up the computations, since the minimum possible time step is a fixed fraction of a shedding cycle.

- $Re=300$
- $M=0.1$
- $\Delta t^* = 0.005$ shedding cycles (non-dimensional time step)

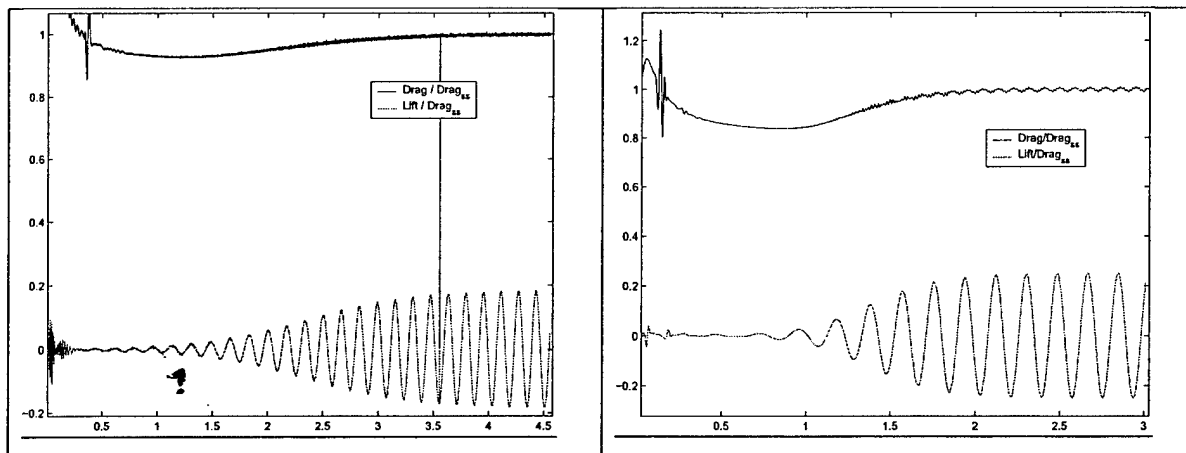


Figure 5.0 Lift and Drag forces during the startup of the CFD simulation. Left, $Re = 150$; right, $Re = 300$

5.2 “D” Shaped Cylinder: Surface Mounted Sensor Estimation

Recent research on closed-loop control of the von Kármán wake instabilities have addressed the issue of sensor placement and number based on non-intrusive sensors in the wake. This approach may not always be implemented and it is important to develop an effective method for sensor placement and number based on body mounted sensors. These sensors may measure skin friction or surface pressures, as done in this effort. The advantages of surface mounted sensors are:

- Simple, relatively inexpensive and reliable
- Essential for real-life, closed-loop flow control applications where the direct measurement of the wake flow field is cumbersome (if not impossible)
- Enable “nearly collocated” sensors and actuators, which eliminates substantial phase changes (affects controller design)

In this section, we demonstrate and validate a systematic approach, based on the spatial Eigen-functions of the POD model, for determining sensor number and location for estimation of the truncated POD states of a cylinder wake. A simple model of the flow-field was sought to design sensor configuration for feedback control algorithms. Numerical simulations were conducted on COBALT solver V.2.02. In this effort, the solver was used for direct numerical solution of the Navier Stokes equations with second order accuracy in time and space. An unstructured two-dimensional grid with 120,000 nodes and 115,000 elements was used. The cylinder geometry comprises of a semi ellipse with base height of 7mm and length of 61.25mm. Additional simulation parameters are as follows:

- Initial perturbation: $AOA=1^\circ$ (to kick off the vortex shedding)



- Damping Coefficients:
 - Advection = 0.01
 - Diffusion = 0.00
- Reynolds Number: $Re = 300$
- Free stream velocity: $U_{inf} = 34$ [m/s]
- Shedding Frequency 8.02 Hz
 $\Rightarrow St = 0.165$
- Time-step = 0.5 ms
 $\Rightarrow 250$ time steps per shedding cycle

The simulation was triggered by skewing the incoming mean flow by $\alpha = 1$ degrees to introduce an initial perturbation. The validity of the CFD model, used in this effort was established by comparing the Strouhal number from the simulation to a water tunnel experiment. The water tunnel experiment yielded $St = 0.163$, therefore there is good agreement since the difference between simulation and experiment is far less than the experimental uncertainty of 0.01.

In this effort, the flow field in the wake, represented by the Pressure and stream-wise Velocity variables are obtained from the numerical solution of the Navier-Stokes equations obtained using the CFD model. All the 100 snap-shots (~ 15 shedding cycles) were equally spaced in time. The snap-shots were taken after ensuring that the cylinder wake reached steady state. For control design purposes, the POD method enables the Navier-Stokes equations to be modeled as a set of ordinary differential equations (O.D.E.). At first, the flow field data is loaded and arranged from the CFD solver of the "D" shaped cylinder wake at $Re = 300$. The decomposition of this component of the velocity field (a similar representation may be made for the Pressure field) is as follows:

$$\tilde{u}(x, y, t) = U(x, y) + u(x, y, t) \quad (5.1)$$

where U denotes the mean flow and u is the fluctuating component that may be expanded as:

$$u(x, y, t) = \sum_{k=1}^n a_k(t) \phi_i^{(k)}(x, y) \quad (5.2)$$

where $a_k(t)$ denotes the time-dependent coefficients and $\phi_i(x, y)$ represents the non-dimensional spatial Eigen-functions of the Velocity (see Fig. 5.1) and Pressure (see Fig. 5.2) determined from the POD procedure. From an ensemble of snapshots, the 'mean snapshot' is computed and then this mean is subtracted from each member of the ensemble. This is done primarily for reasons of scale; *i.e.* the deviations from the mean contain information of interest but may be small compared with the original signal.

Next, the empirical correlation matrix is computed using the inner product. Solving the Eigen-value problem, the Eigen-values and the orthogonal spatial Eigen-functions, $\phi_i(x, y)$, are obtained. Since the Eigen-values measure the relative energy of the system dynamics contained in that particular mode, they may be normalized to correspond to a percentage of the system energy. For the current working point ($Re=300$), the Eigen-values for the Pressure and U-



Velocity are presented in Table 5.1. Note that the great majority of the energy, associated with the POD procedure, is located in the first two modes.

Mode	Pressure POD Eigen-Values [%]	Velocity (U) POD Eigen-Values [%]
1	48.21	49.31
2	41.30	43.14
3	4.73	2.92
4	4.68	2.85
Total	98.92	98.22

Table 5.1: Eigen-Values of Wake Flow-Field

Finally, the time histories of the temporal coefficients of the POD model, $a_k(t)$, are determined using the extracted spatial modes and the snapshots of the unforced flow. However, it is not possible to obtain a direct measurement of a_k , which is why it needs to be estimated from direct measurements such as body mounted sensors. An important aspect of reduced order modeling concerns truncation. How many modes are important and what are the criteria for effective truncation?

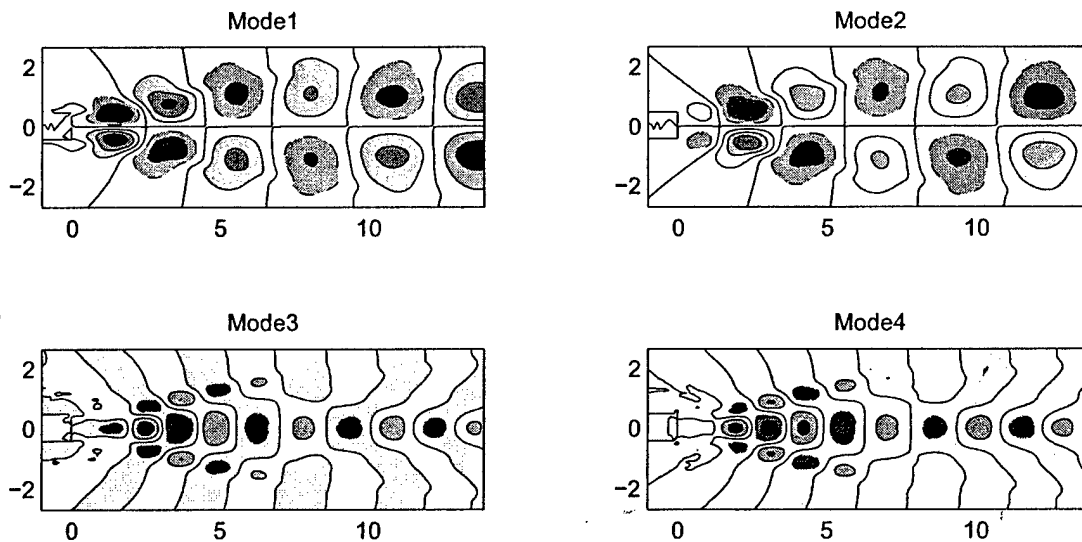


Figure 5.1. Eigen-Functions of stream-wise Velocity of the "D"-shaped cylinder Wake Flow Field Solid lines are positive, dashed lines are negative isocontours

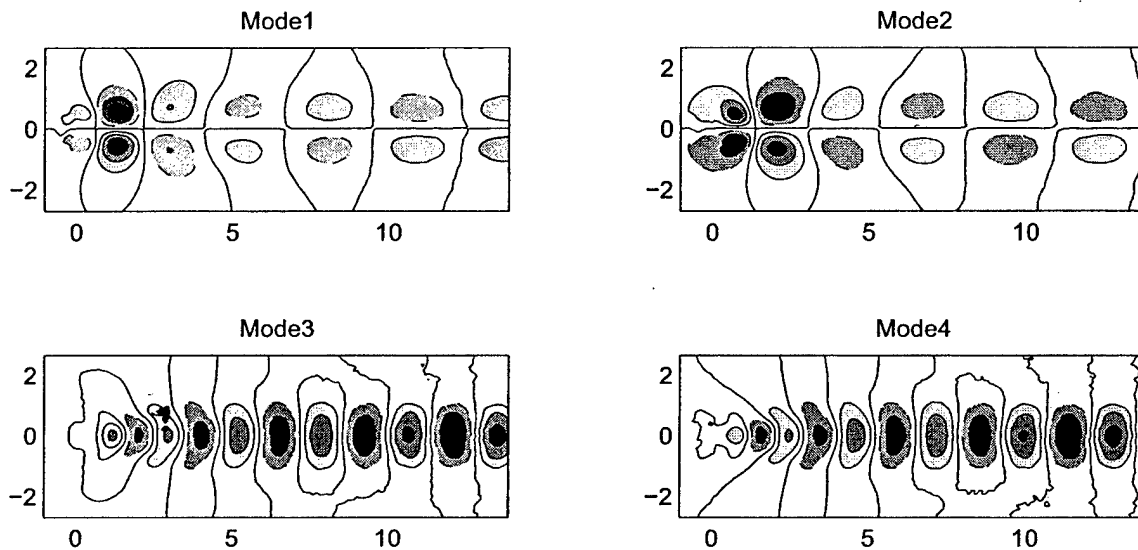


Figure 5.2 Eigen-Functions of Pressure of wake Flow Field
 Solid lines are positive, dashed lines are negative isocontours

The answers to the above questions have been addressed by Cohen et al (2003). That effort demonstrated that control of the POD model of the von Kármán vortex street in the wake of a circular cylinder at low Reynolds numbers ($Re \sim 100$) is enabled using just the first mode. Furthermore, feedback based on the first mode alone significantly attenuated all the other modes in the four-mode POD model.

In view of the above result, in this effort, truncation of the POD model takes place after the first three modes, which contain 95-97% of the energy, as seen in Table 5.1. At this point, it is imperative to note the difference between the number of modes required to *reconstruct* the flow and the number of modes required for effective low-dimensional modeling for control design purpose. In this effort, we are interested in estimating only those modes required for closed-loop flow control. On the other hand, a more accurate reconstruction of the velocity and pressure field, based on a low-dimensional model, may be obtained using between 4-8 modes.

The quintessential question is whether an effective estimate of the states, of the 3 mode low-dimensional model coefficients, a_k , can be estimated based on body mounted pressure sensors. The answer is positive and the details that provides the estimate of the first three modes, a_1 - a_3 , are presented in the next section.

The time histories of the temporal coefficients of the flow field Velocity and Pressure variables are determined by introducing the POD spatial Eigen-functions into the flow field data using the least squares technique. The intent of the proposed strategy is that the pressure measurements provided by the body mounted pressure sensors are processed by the estimator to provide the estimates of the first three temporal modes of the flow field variables stream-wise Velocity and Pressure. The estimation scheme, based on the linear stochastic estimation (LSE) procedure introduced by Adrian (1977), predicts the temporal amplitudes of the first three POD



modes from a finite set of pressure measurements obtained from the CFD solution of the uncontrolled cylinder wake. All the measurements were taken after ensuring that the cylinder wake flow regime converges to steady state vortex shedding. The mode amplitudes, a_1 - a_3 , will be mapped onto the extracted sensor signals from the pressure sensors, u_s , as follows:

$$a_n(t) = \sum_{s=1}^m C_s^n u_s(t) \quad (5.3)$$

where m is the number of sensors and C_s^n represents the coefficients of the linear mapping. The effectiveness of a linear mapping between for velocity measurements and POD states has been experimentally validated by Cameron et al (2004). The coefficients C_s^n ($n=1-3$; $s=1, m$) in Equation (5.3) are obtained via the linear stochastic estimation method from the set of discrete sensor signals and temporal mode coefficients, $a_1 - a_3$.

The issue of sensor placement and number has been dealt with in an ad-hoc manner in published studies concerning closed-loop flow control. For effective closed-loop control system, the following questions need to be answered:

- How many sensors are required?
- Where should the sensors be placed?
- What are the criteria for judging an effective sensor configuration?
- What are the robustness characteristics of a given sensor configuration?

In this effort, an attempt will be made to emulate some of the proven successes from the field of structural control. Heuristically speaking, when some very fine dust particles are placed on a flexible plate, excited at one of its natural frequencies, after a short while the particles arrange themselves in a certain pattern typical of those frequencies. The particles will be concentrated in the areas that do not experience any motion (the nodes). On the other hand, at the areas where the motion is large (the internodes) will be clean of particles. It is at the internodes that the vibrational energy of that particular mode is at a maximum and sensors placed at these locations are extremely effective in estimating that particular mode.

The above heuristic approach has been used by Siegel et al (2003) in locating effective sensor placement for acceleration feedback control to alleviate tail buffeting of a high performance twin tail aircraft. Note the usage of the term "effective sensor configuration" as it is based on validated heuristics as opposed to "optimal sensor configuration" that results from a mathematically optimal pattern search for a sensor configuration. So, what needs to be done to determine an effective sensor configuration is to find the areas of energetic modal activity.

CFD data provided simulated pressure signals at 286 locations distributed at equidistances all along the surface of the cylinder (see the cylinder surface grid in Fig. 5.3). A three- step procedure is proposed for determining sensor placement and number as follows:

- Run the POD procedure on the 286 pressure signals. Examine the frequencies of the energetic modes. In this effort, three energetic modes are found and their frequencies correspond to the fundamental von Kármán shedding frequency (first two modes) and the next higher frequency (third mode).



- The spatial Eigen-functions obtained from the POD procedure provides information concerning the locations where the modal activity is at its highest (see Fig. 5.5). Examine the maxima/minima of the spatial Eigen-functions of the 286 Pressure signals.
- Place sensors at the energetic maxima and minima of each mode as shown in Fig. 5.3. The locations of the sensors in Table 5.2 are referenced in terms of the coordinates, non-dimensionalized with the model base height H , namely, X/H and Y/H . Three sensors are placed at the upper surface of the cylinder near the trailing edge and three more sensors placed symmetrically at the lower surface. These six sensors target modes 1 and 2. Finally, four sensors are located at the base of the cylinder, targeting mode 3. The time histories of the 10 sensors are presented in Fig. 5.4. Note the two distinct frequencies picked up by the sensors.
- Run the LSE procedure to obtain the transformation matrix C^n , and to obtain the estimates of the U-Velocity/Pressure POD mode coefficients. The estimated versus desired mode amplitude plot, for the above sensor configuration is presented in Fig. 5.6. The estimates resulting from the 10 sensor configuration are very accurate as seen in Table 5.2.

For convenience, this RMS error (defined as the difference between the RMS of the desired extracted mode amplitudes and the estimates obtained from the LSE procedure) is normalized with the RMS of the desired extracted mode amplitudes, presented as a percentage. The resulting error and the number of sensors may be integrated together into a cost function. The purpose of the design process would then be to select the configuration that minimizes this cost function. For this configuration, the RMS estimation errors are provided in Table 5.2. Considering the fact that the LSE is providing U-Velocity/Pressure estimates of the wake flow field, the RMS values in Table 5.2 are low and can be used for closed-loop flow control using a moderately robust controller. Also, provided in Table 5.2 are the RMS errors for sensor configurations consisting of 2, 4 and 6 sensors. Note that the three latter configurations enable the estimation of modes 1 and 2 quite well but not of the 3rd since they do not include a sensor that targets the higher frequency.

Number of Sensors	Sensor Locations (x/H, y/H)	Mode 1 RMS Error [%]	Mode 2 RMS Error [%]	Mode 3 RMS Error [%]	POD Coeff. Estimated (in Wake)
2	(-0.07, 0.50), (-0.10, -0.50)	22.74	60.27	Only Modes 1 & 2 Targeted	Pressure
4	(-0.07, 0.50), (-0.10, -0.50) (-0.10, 0.50), (-0.07, -0.50)	2.99	8.07	Only Modes 1 & 2 Targeted	Pressure
6	(-0.07, 0.50), (-0.10, -0.50) (-0.10, 0.50), (-0.07, -0.50) (-0.13, 0.50), (-0.13, -0.50)	0.78	2.17	Only Modes 1 & 2 Targeted	Pressure



10	(-0.07, 0.50), (-0.10,-0.50) (-0.10, 0.50), (-0.07,-0.50) (-0.13, 0.50), (-0.13,-0.50) (0, 0.42), (0,-0.01) (0, 0.24), (0,0.08)	0.77	2.10	20.90	Pressure
10	Same 10 sensor configuration as above	2.30	2.30	12.5	U_Velocity

Table 5.2: Sensor Coordinates and RMS Estimation

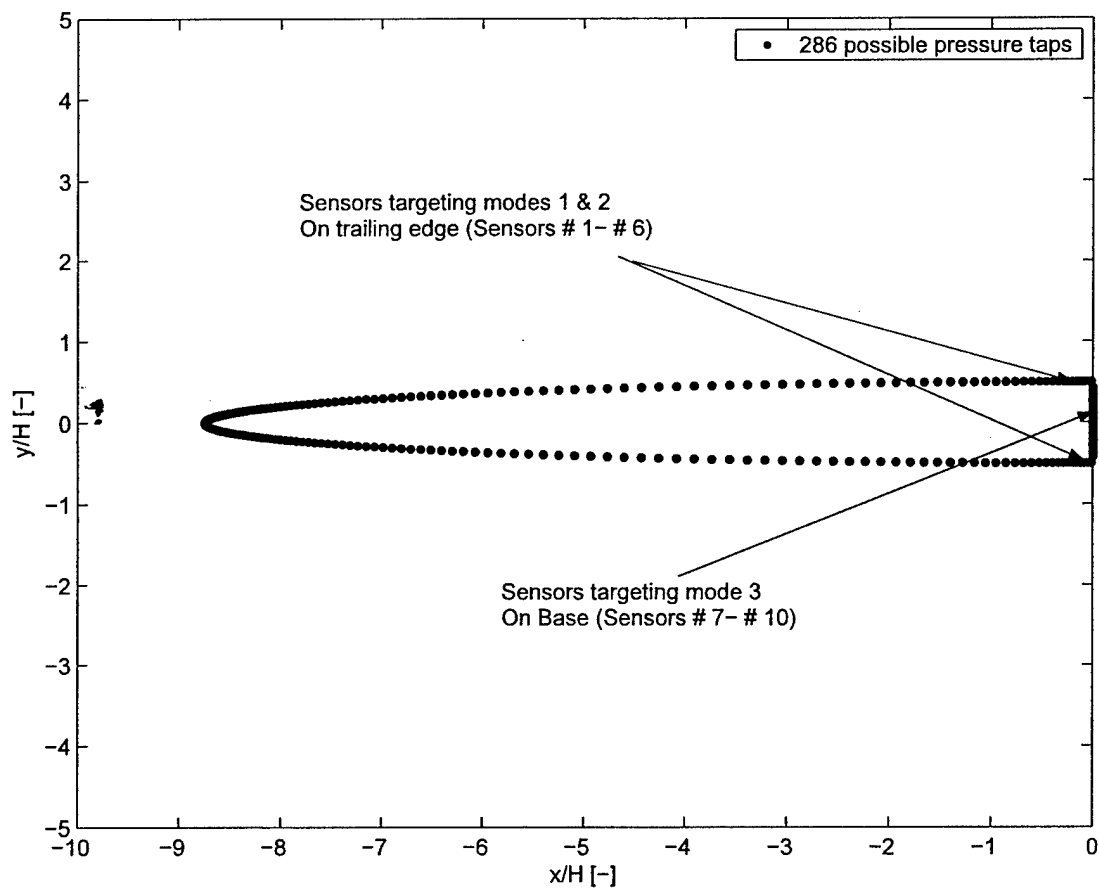


Figure 5.3. 10 sensor configuration out of 286 possible ports

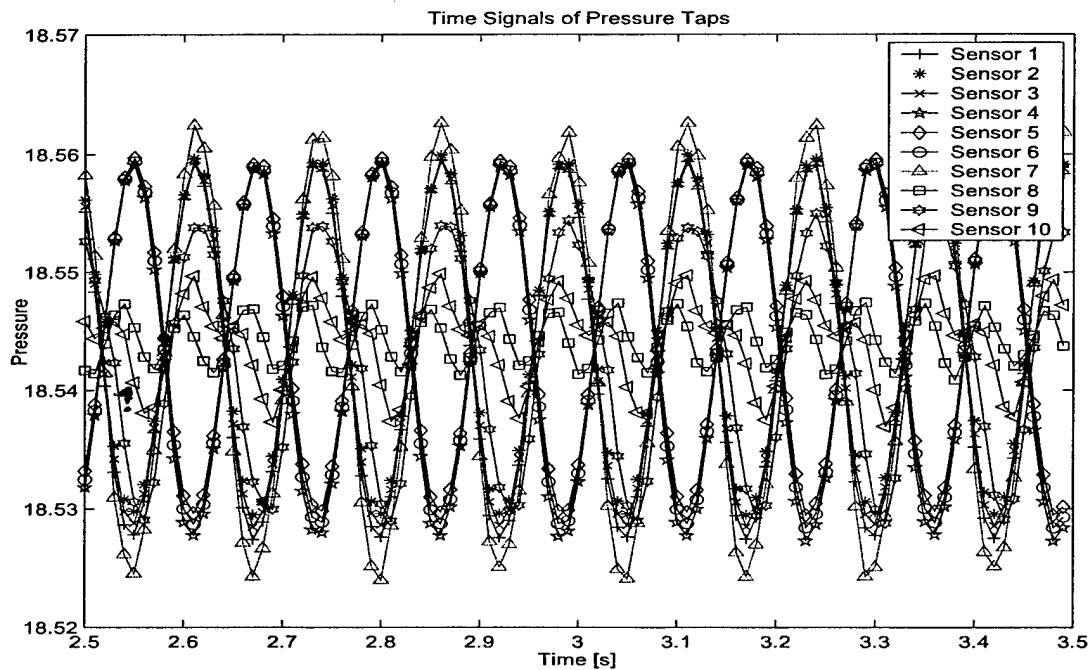


Figure 5.4. Time Histories of Pressure taps for the 10 Sensors

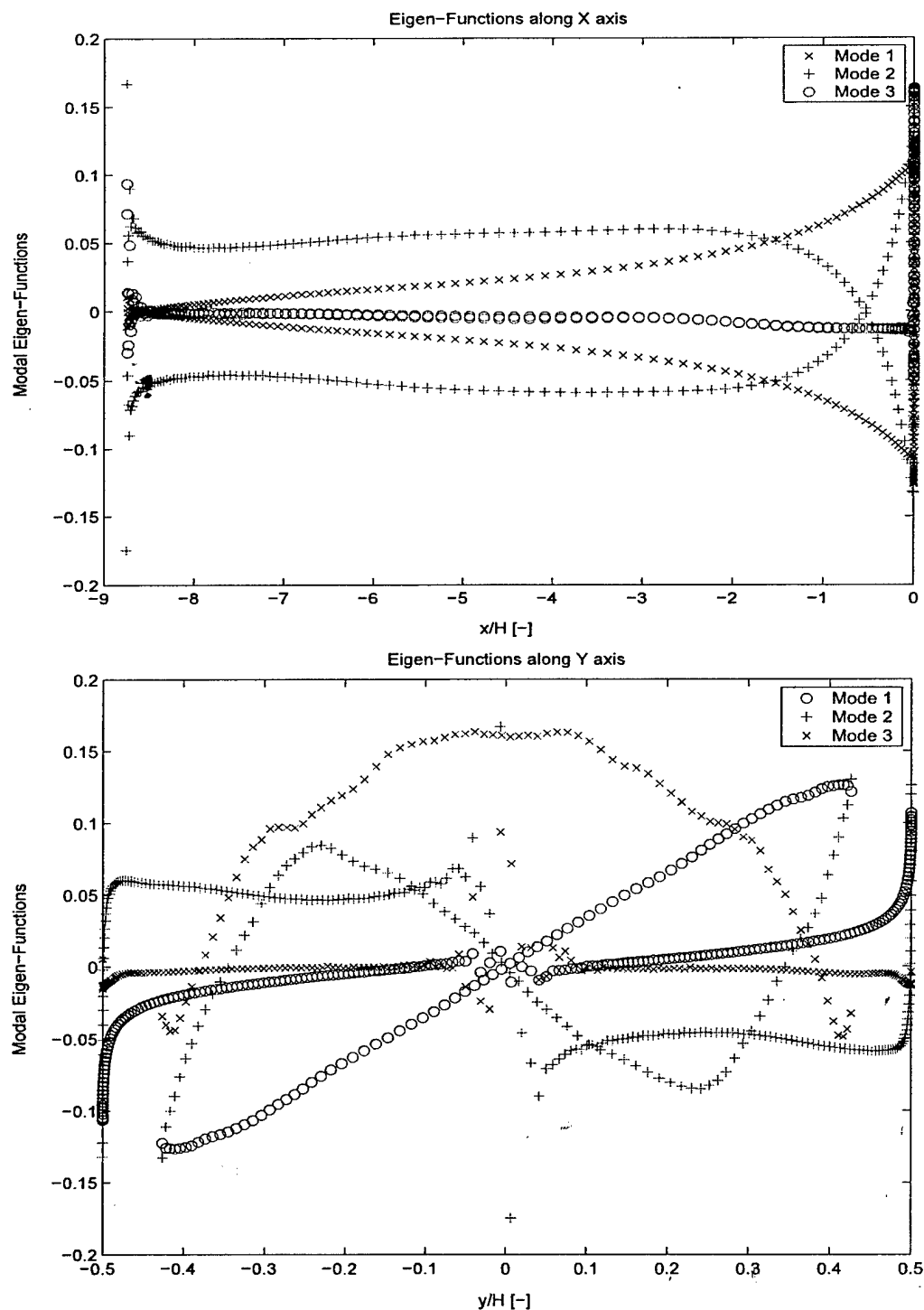
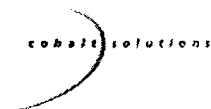


Figure 5.5. Spatial Surface Eigen-functions for 286 Pressure sensors (note that the mode amplitudes are plotted against x/H – in the top Figure; and against y/H in the bottom Figure)

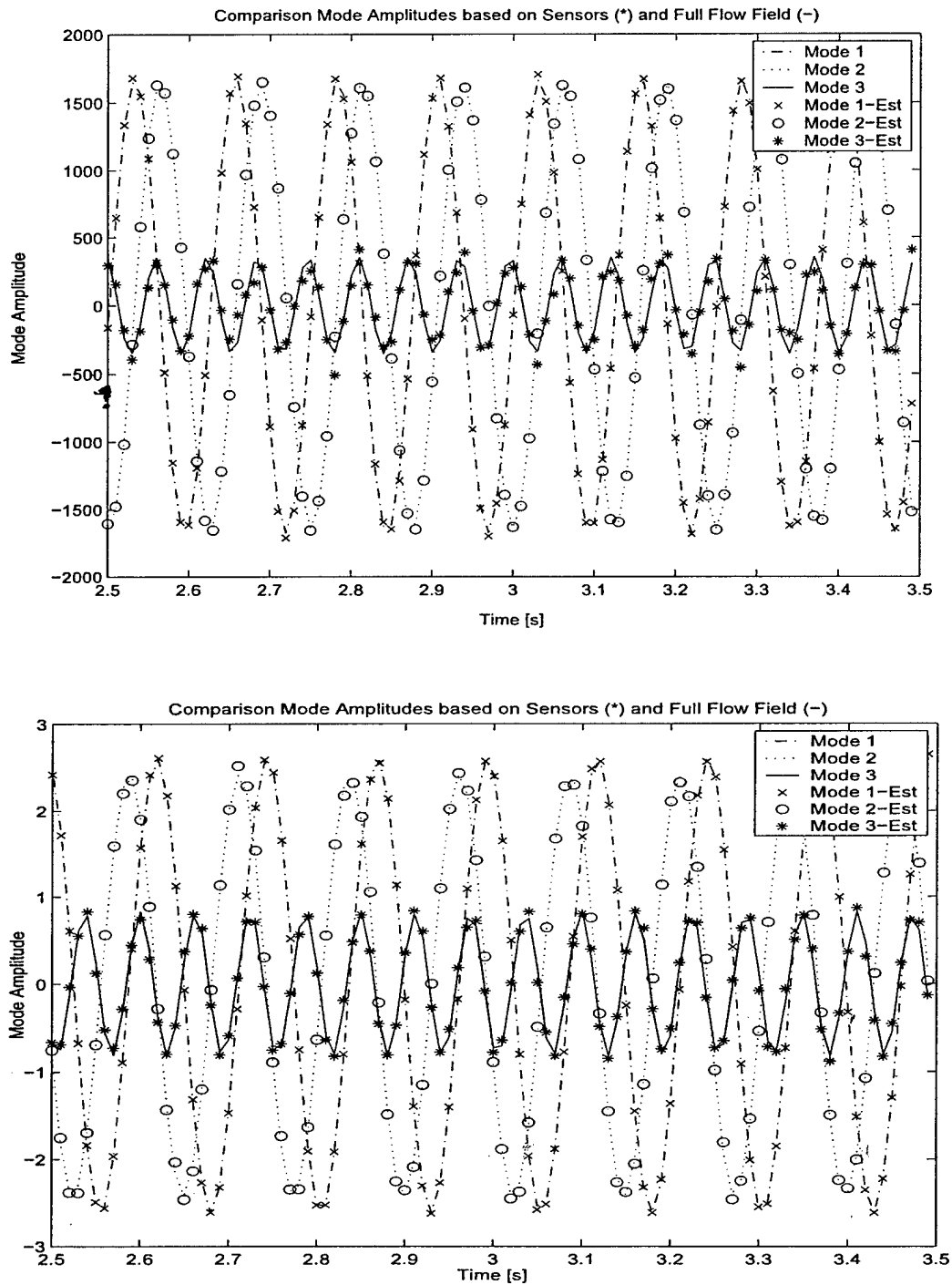


Figure 5.6. Estimation of POD Time Coefficients for 10 Sensor configuration
 (U_Velocity – Top Figure; Pressure – Bottom Figure)



5.3 "D" Shaped Cylinder: Blowing/Suction Modeling

Figure 5.7 shows the grid implementation of blowing and suction slots into the D shaped cylinder geometry. The actuators are modeled by short channels at an angle of 30 degrees to the mean flow. At the end of the channel a either periodic or feedback controlled velocity is prescribed, leading to an unsteady flow through the channel into the flow field.

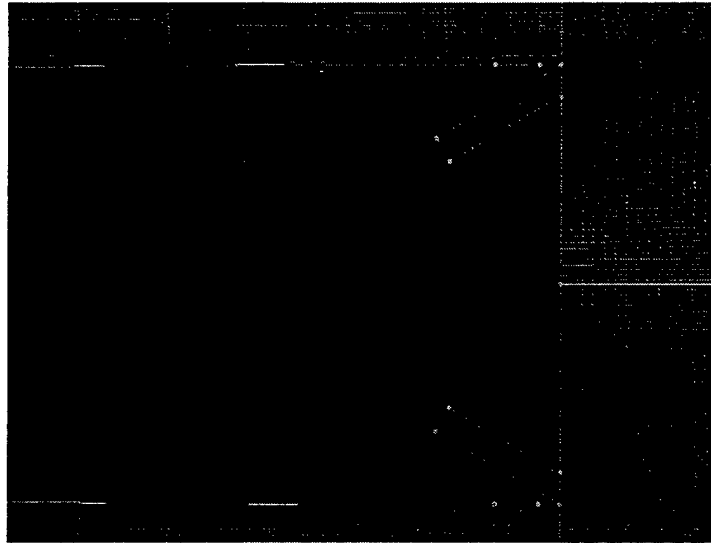


Figure 5.7 Computational grids developed for modified D-shaped cylinder using blowing and suction actuation.

Figure 5.8 demonstrates the effect of periodic open loop blowing and suction through these patches at the bottom of short ducts at an angle of 30 degrees to the freestream direction. The forcing frequency is equal to the natural shedding frequency, while the peak velocity during a sinusoidal blowing and suction cycle is 12.5% or 100% of the freestream velocity, respectively. The top and bottom slot were operated 180 degrees out of phase for all investigations. The plots show isocontours of vorticity, demonstrating the local effect of the forcing. The blowing and suction velocity is not large enough for the resulting jet to penetrate the boundary layer in either case. However, with the higher velocity more vorticity is injected into the boundary layer, effectively cutting of the forming vortices. Additionally, the vorticity ejected from the slots then merges with the vortices of the Karman vortex street.

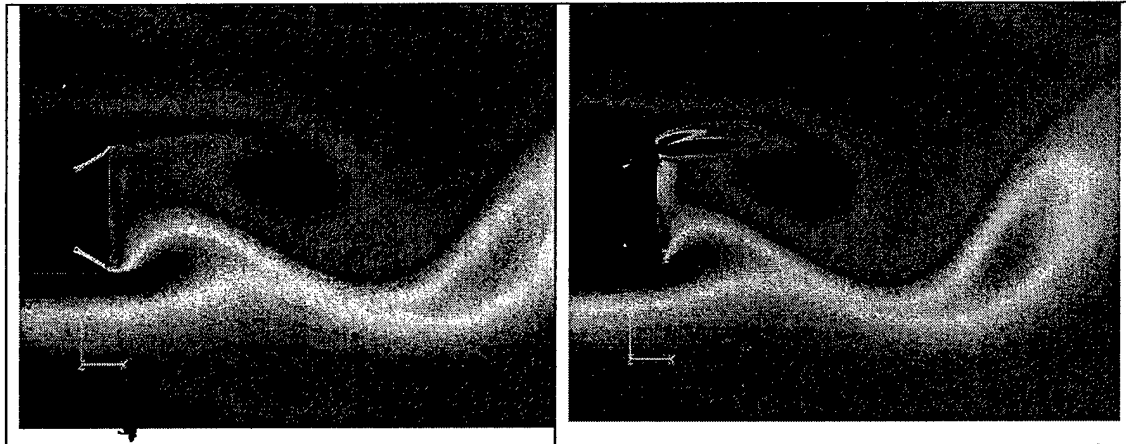


Figure 5.8 Instantaneous snapshots of vorticity during a blowing and suction cycle. Left, 12.5% of the freestream velocity, right, 100% of the freestream velocity.

As can be seen in the transient lift and drag force plots shown in Figure 5.9, the higher velocity forcing creates a transient behavior that is quite different in that there is significant overshoot before the wake settles into a phase locked state. This is a result of the vorticity ejected from the blowing and suction slot merging with the vortex street, an effect that is not existent for smaller velocities. The open loop investigations used blowing and suction peak velocities down to 3% of the freestream velocity, however, for values smaller than about 10% the transient settling times increased strongly. This indicates a loss of controllability, and 10% was determined to be the minimum desirable actuation amplitude for the subsequent closed loop controlled simulations.

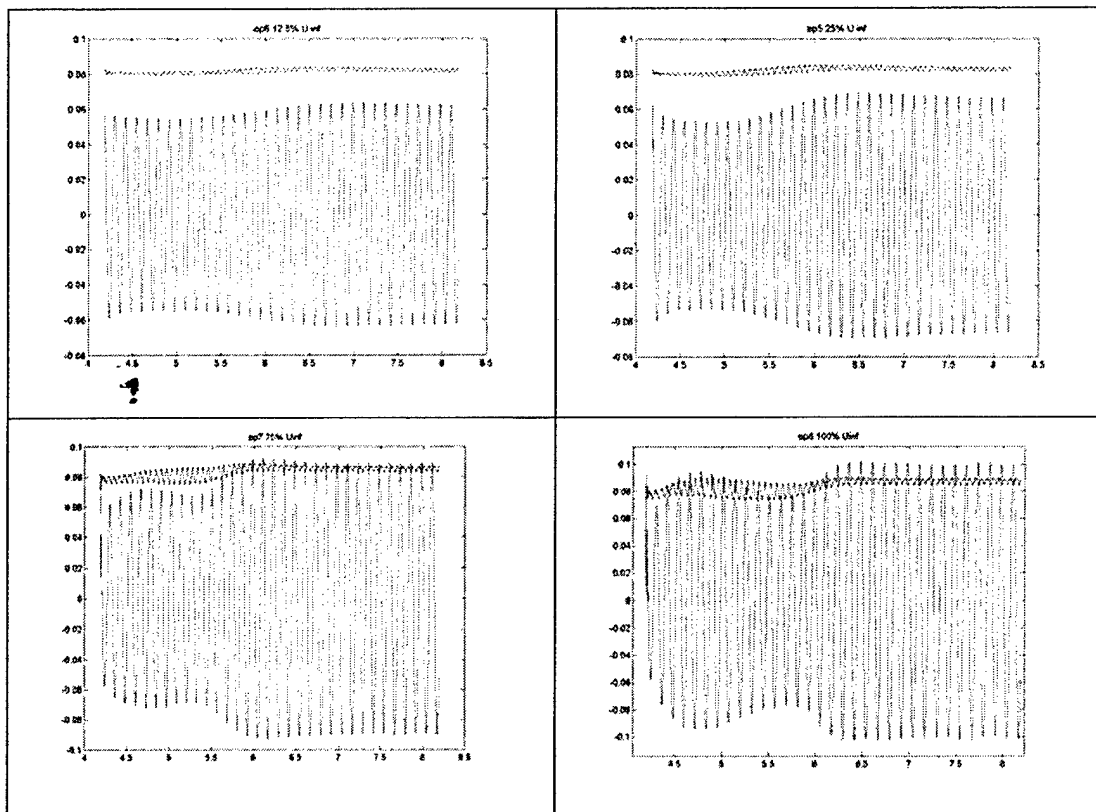


Figure 5.9 Transient lift (green) and drag (blue) forces for different actuation levels; top left: 12.5% of the freestream velocity, top right: 25%, bottom left: 75% and bottom right: 100% of the freestream velocity.

5.4 "D" Shaped Cylinder: Feedback Controlled Results and Discussion

For the feedback controlled simulations, the spatial modes shown in figure 5.10 were employed for global flow state estimation. They are qualitatively similar to the modes found in the circular cylinder wake which are shown in Figure 4.3. The procedure used to develop these modes is identical to the procedure used for the circular cylinder, which is presented in the previous chapter. The sensor arrangement used for the circular cylinder consisting of a rectangular grid of 35 sensors was also kept.

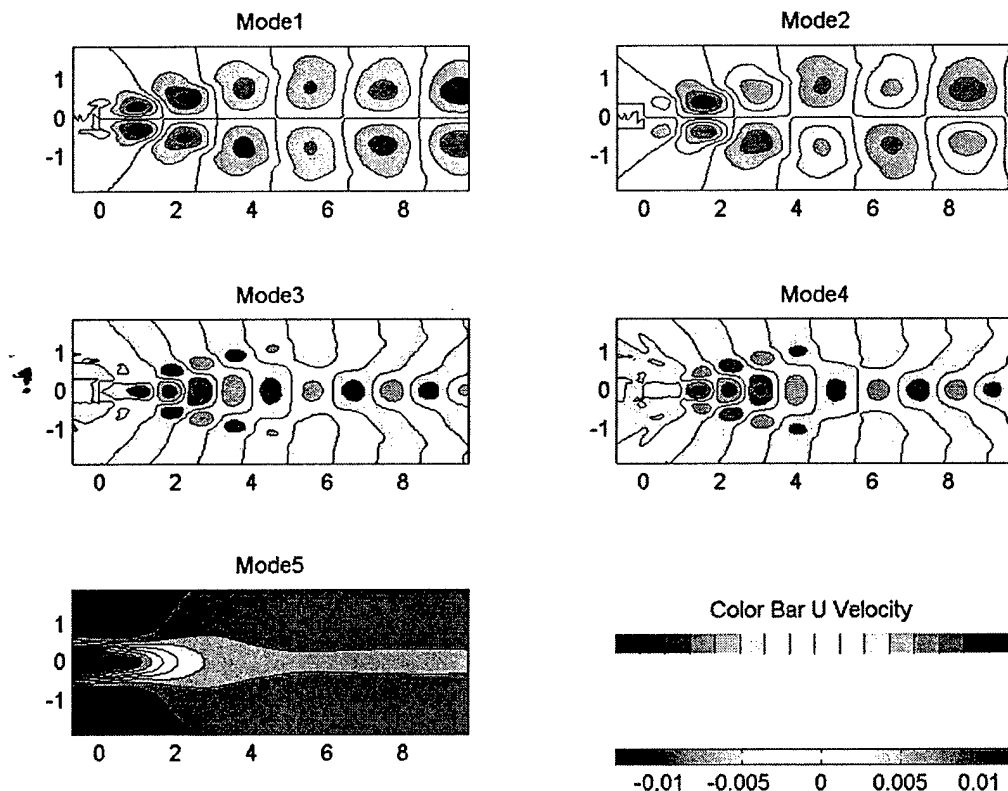


Figure 5.10 POD modes used for feedback state estimation.

A scan through the range of possible controller feedback phases showed an increase in vortex shedding and modal amplitudes for phases in the range of 0 – 120 degrees, a neutral range where the intensity of the vortex street remained about the same between 120 – 180 degrees, and reduction in vortex shedding strength for phase angles beyond 180 degrees. Figure 5.11 demonstrates the ability to reduce vortex shedding with a feedback phase of 210 degrees. The unsteady lift fluctuations decrease continuously over about 20 shedding cycles and are stabilized at a level 40% lower than in the natural wake. During the same time the drag force decreases by about 10%. This behavior is qualitatively similar to the circular cylinder wake, while the reduction levels in unsteady lift and mean drag force have not yet been matched. This may be accomplished by adjusting the feedback parameters further, which is exceeded the scope of this study. Figure 5.12 shows the changes in vortex shedding patterns due to the feedback. The formation length has increased, and the vortices being shed are less strong than in the unforced case. These findings compare well with the circular cylinder results as well.

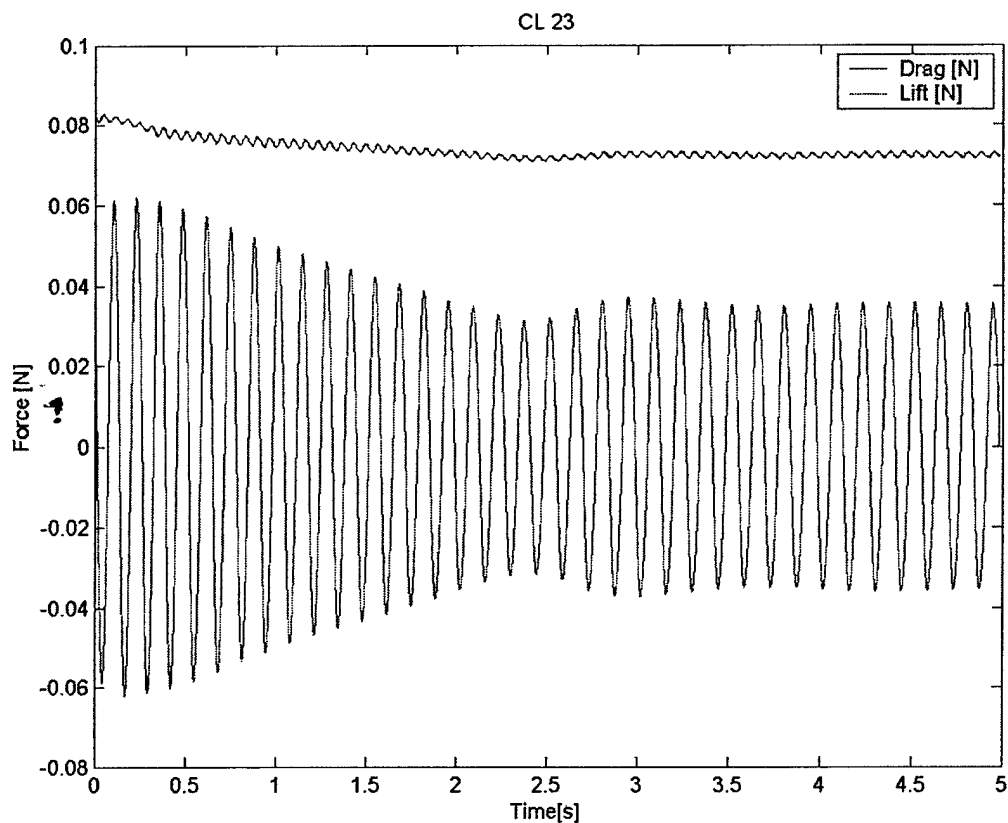


Figure 5.11 Feedback controlled lift and drag force.

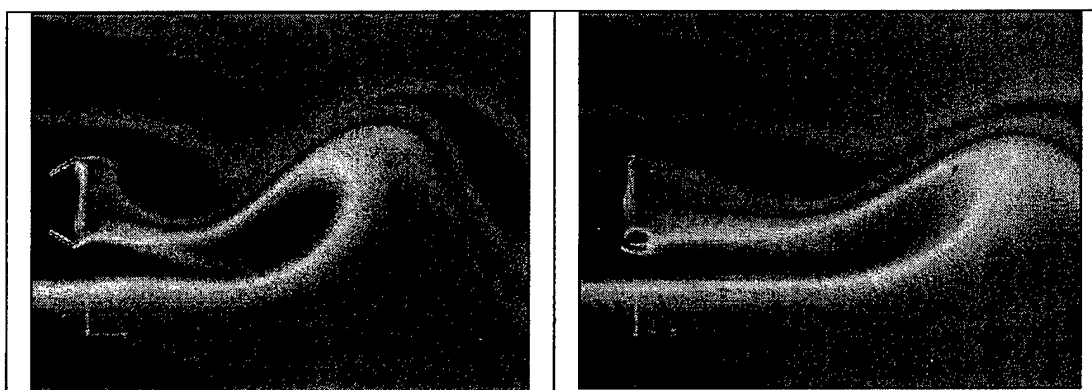


Figure 5.12 Unforced (left) and feedback controlled (right) vorticity contours.

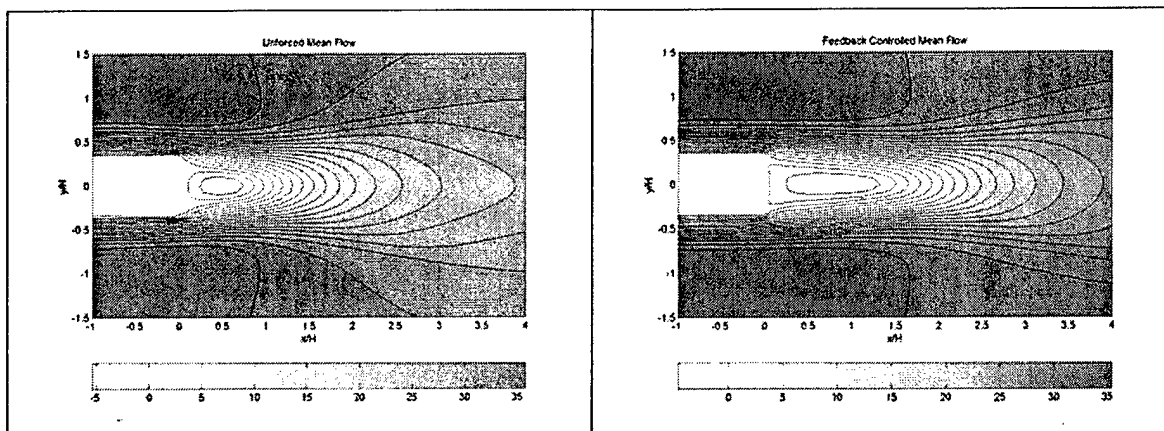


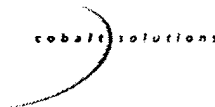
Figure 5.13 Unforced (left) and feedback controlled (right) mean flow.

The transfer of energy from the vortex shedding back to the mean flow is shown in figure 5.13. A similar lengthening of the recirculation zone that was observed in the circular cylinder wake is achieved in the D shaped cylinder wake, even though the increase in recirculation zone length is again less than in the circular cylinder wake.

While the geometry of the circular and D shaped cylinders are very different, and different actuation methods were employed, we demonstrate that the feedback flow control toolbox is well suited to develop and test control algorithms for this flow field. The approach of using POD for global flow estimation is just as well suited for the blowing and suction slot actuated flow field as it is for the translation actuated flow field of the circular cylinder. Moreover, the response of both flow fields to the feedback control is very similar, indicating that feedback flow control is applicable to different wake flow topologies. Since the D shaped cylinder features fixed separation points, the data presented shows conclusively that our control approach influences the vortex shedding and formation in the wake directly, rather than modifying the stability behavior of the mean flow by using separation control.

5.5 "D" Shaped Cylinder: Experimental Validation and Discussion

In order to validate the computational results, the vortex shedding frequency of the D shaped cylinder simulations were compared to water tunnel experiments. Figure 5.14 shows good agreement between experiment and simulation, indicating sufficient resolution of the numerical model. In case of under resolved numerical simulation in unsteady wake flows the shedding frequency deviates significantly, as has been shown for circular cylinder wakes in literature.



Plot of Strouhal Number vs. Reynolds number for Water tunnel data and CFD data

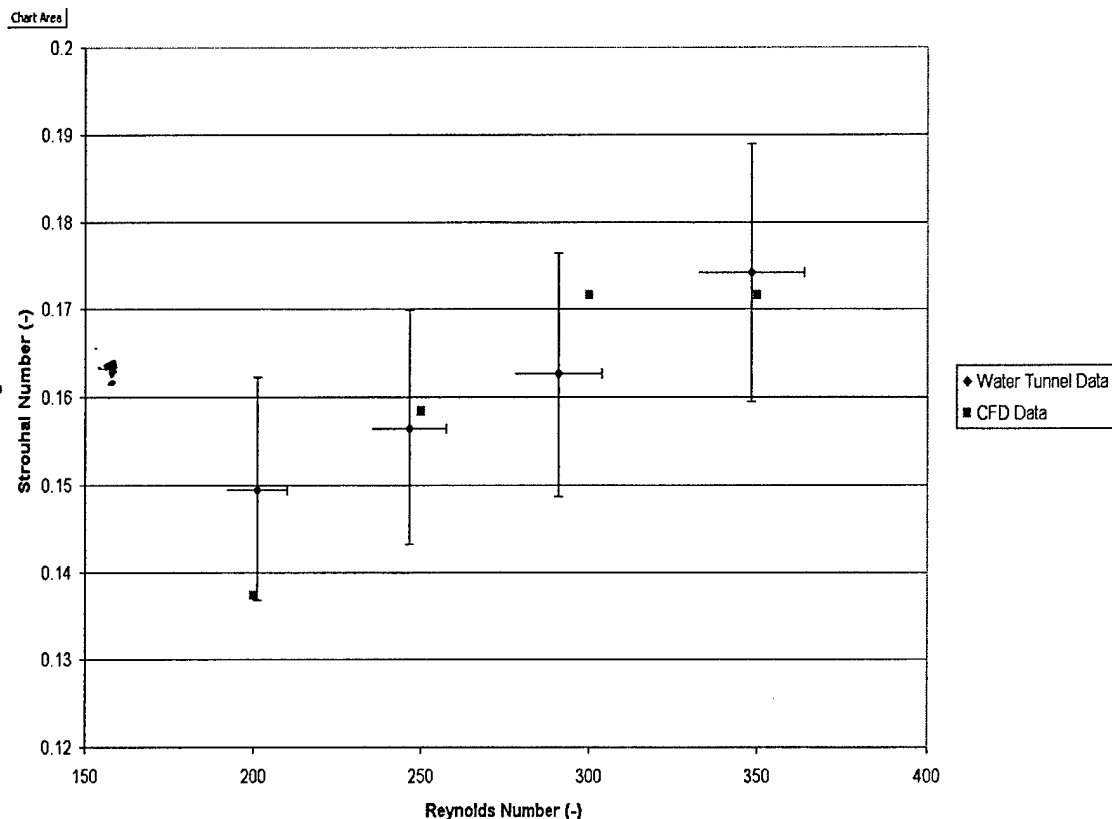


Figure 5.14 Strouhal number comparison for different Reynolds numbers.

5.6 "D" Shaped Cylinder: 3-D High Reynolds Number Baseline CFD

Calculations of the "D" shaped cylinder were performed at a Reynolds number based on base height of 3900, using the experience gained on the circular cylinder. The two-d grid used for the closed loop control cases was extruded into the span using 66 points and 4 base diameters, resulting in a grid with 7.5×10^6 cells. This was larger than the circular cylinder grids due to the very fine-spacing in the x-y plane. LES with no explicit model was applied just as was the case for the circular cylinder. A non-dimensional timestep of 0.01 (made non-dimensional by the freestream velocity and base height) was used. A visualization of the flow using iso-surfaces of vorticity is shown in Figure 5.15. Note that the shedding is occurring at different phases along the span, evidenced by spanwise pressure variations near the back end of the cylinder. This demonstrates the likely necessity of spanwise distributed actuators. The wake exhibits similar structures as seen for the circular cylinder. There are spanwise rollers connected



to streamwise counter-rotating vortices. These results will be available for use in phase II for 3-D attempts at control of a higher Reynolds number flow.

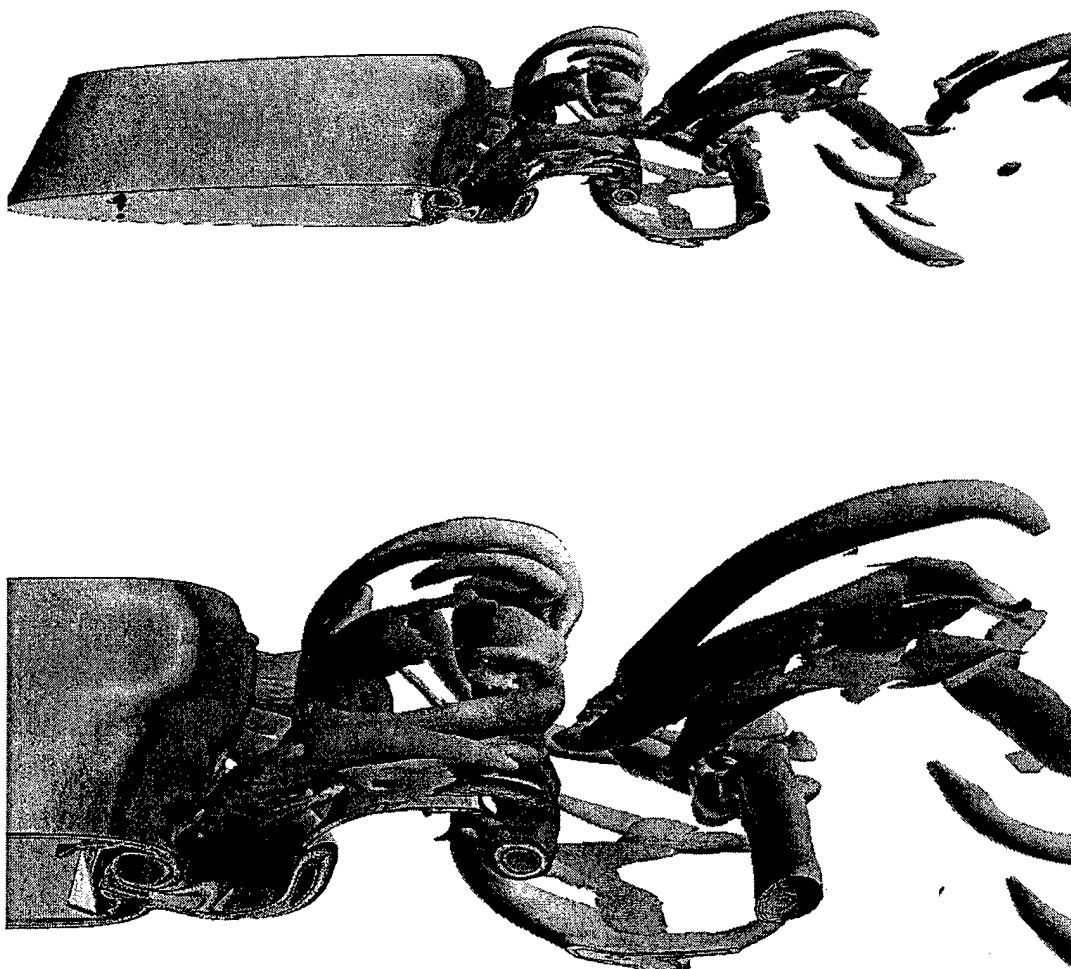


Figure 5.15 LES calculation of the "D" shaped cylinder. Isosurface of vorticity colored by pressure.



6. Application III: NACA 0015 Airfoil Separation Control

6.1 NACA 0015 Airfoil: Application Background

Separation control on the NACA 0015 airfoil serves as the final demonstration case of the developed flow control toolbox. It should be realized that in this case the objective of flow control is entirely different than in the wake cases described above. The goal here is the delay of flow separation, and it is clear from a hydrodynamic stability point of view that the structures in the boundary layer have to be *enhanced* to increase the momentum transfer from the free stream toward the wall. This is essentially the opposite of the goal in control of the wake, where flow control is applied to *reduce* the strength of the vortices in the wake. However, our toolbox was successfully applied to this case as well, as described below.

6.2 NACA 0015 Airfoil: Computational Model

Calculations were performed at a chord Reynolds number of $Re_c=10,000$. The grid is shown in figure 6.1. As a first step, a suitable angle of attack was determined by performing unforced computations angles of attack ranging from 0° to 15° . From these simulations, it was determined that $\alpha=8^\circ$ is optimal. Once a test case was defined, we performed open loop simulations utilizing the blowing and suction boundary condition module at a position of 10% chord on the upper airfoil surface to verify the effectiveness of blowing and suction for controlling airfoil separation. The simulations confirmed the applicability of periodic forcing for separation control. Figure 6.2a shows a snapshot of the instantaneous pressure field of the unforced case, which indicates massive separation near the leading edge and the development of large vortical structures near the trailing edge of the airfoil.



Figure 6.1 Computational grid developed for NACA 0015

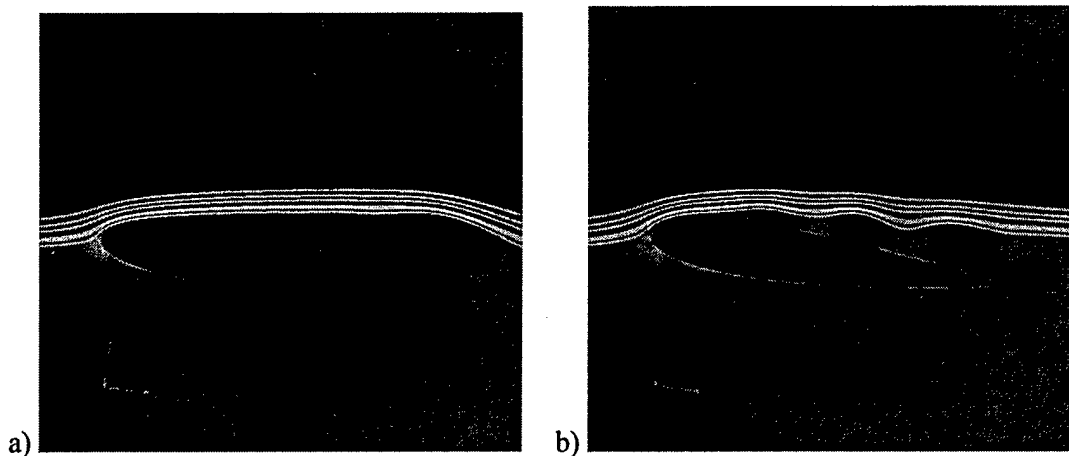


Figure 6.2: Instantaneous pressure and streamlines: a) unforced, b) forced

6.3 NACA 0015 Airfoil: Computational Results and Discussion

Scrutinizing the spatial POD modes of the streamwise velocity component of the unforced case (Figure 6.3) as well as the respective temporal coefficient (Figure 6.4), it becomes clear that two different frequencies are present, one of the vortices in the separated shear layer (Modes 1 and 2, containing 96% of the energy) at a frequency of $F=25\text{Hz}$ and one in the boundary layer (Modes 3 and 4, containing an additional 3%) at a frequency of about $F=60\text{Hz}$. In order to introduce disturbances in the most efficient manner, this frequency was chosen as the forcing frequency.

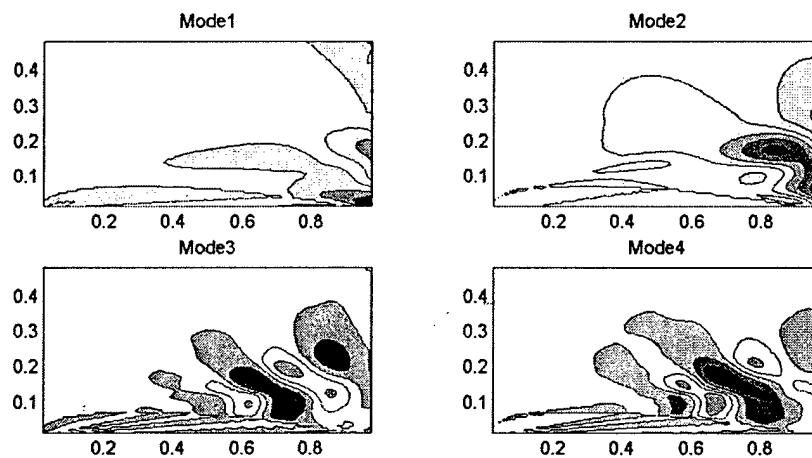


Figure 6.3: POD modes of the U velocity for the unforced case

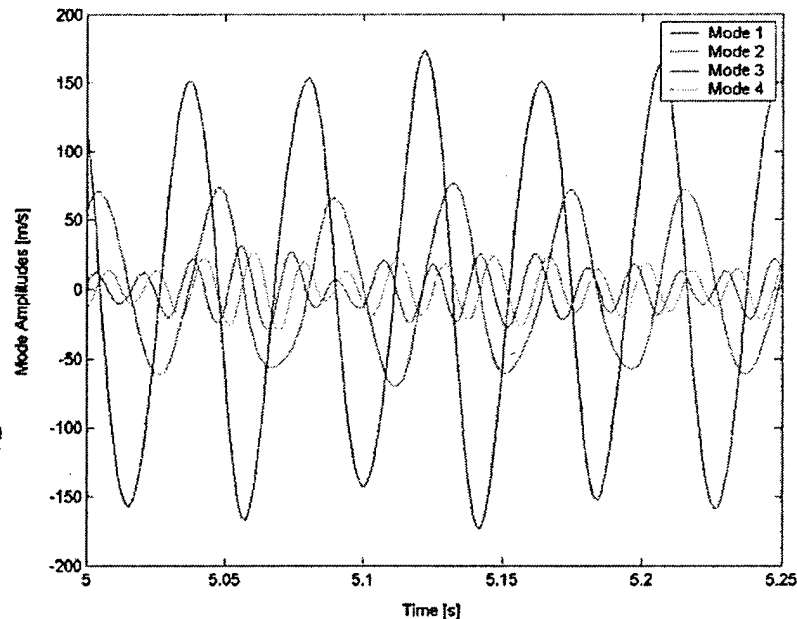


Figure 6.4: Temporal Mode Coefficients for the unforced case

Using a blowing and suction slot 2.5% chord long at a location of 10% chord on the upper surface of the airfoil, periodic blowing and suction with a maximum amplitude of 4m/s (13% of the freestream velocity) was used to attempt the delay of separation. Figure 6.2b shows a snapshot of the instantaneous flow field after the initial transient. The alternating high and low pressure regions indicate the presence of large vortices near the airfoil surface. The resulting POD modes of the U velocity are shown in Figure 6.1. It can be seen that Modes 1 and 2 (containing 98% of the energy) of the forced flow correspond to Modes 3 and 4 of the unforced case. Furthermore, their maxima are significantly closer to the airfoil surface, indicating a reduction of size of the separation.

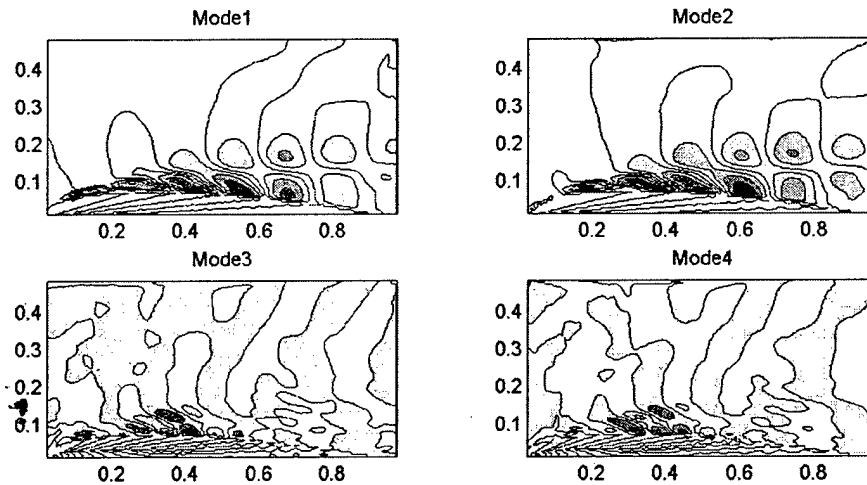


Figure 6.1: POD modes of the U velocity. Forced case, $F=60\text{Hz}$

Concomitant with these changes in flow topology, forcing has a large effect on the lift and drag. Figure 6. shows the time history of the lift (F_y) and drag (F_x) for the unforced (left) and forced (right) cases. Clearly, active control not only markedly reduces the amplitude of the force fluctuations, but also – in the mean – increases the lift by more than 120% and reduced the drag by over 55%.

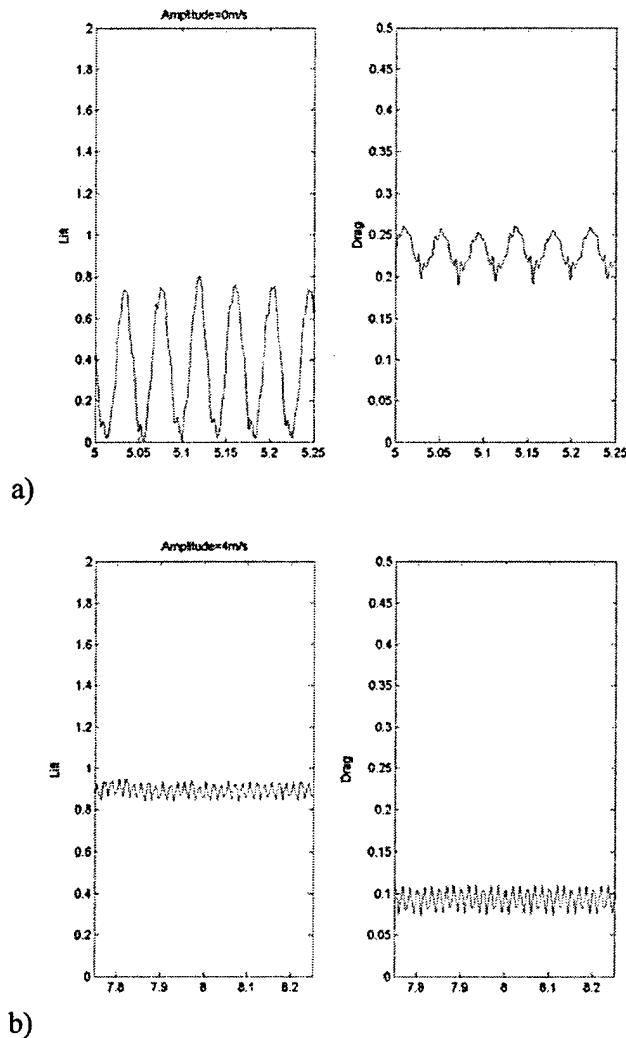


Figure 6.5: Lift (left) and drag (right) for a) unforced and b) forced case

To close the feedback loop, sensor placement has been studied for this flow, using the heuristic method developed earlier. In the current configuration, 20 sensors are placed at the relative maxima of the first U velocity modes for both the forced and unforced cases (see Figure 6.6). Using the time signals at the sensor locations, the flow state can be estimated with errors of less than 10%. Figure 6.7 shows the reconstruction of the time signals of the unforced flow (left) and the forced flow (right).

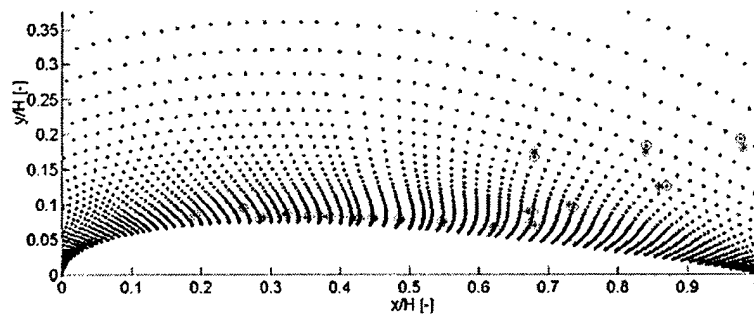


Figure 6.6: Grid points (blue) and sensor location (red)

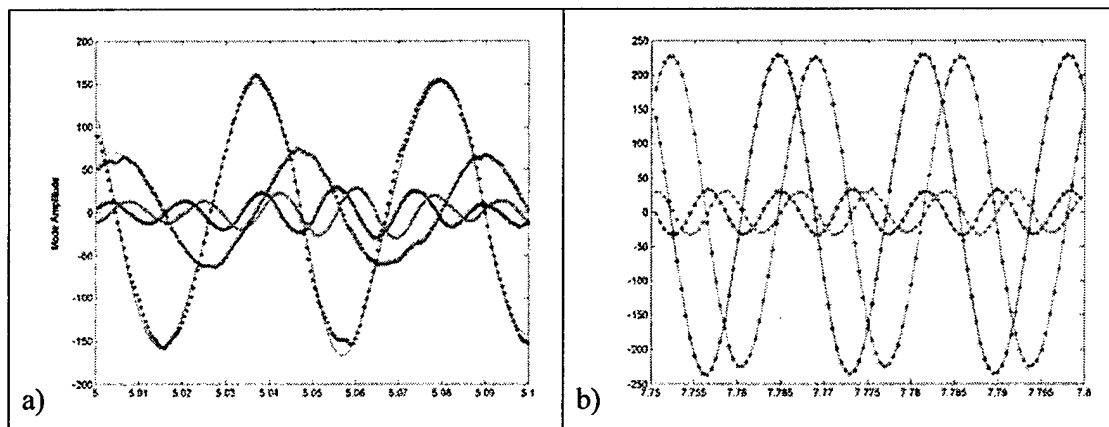


Figure 6.7: Mode estimation. a) Unforced b) Forced

To close the feedback loop, a simple proportional feedback controller is used for the forcing amplitude only. In order to determine the sensor signal best suited for feedback, a transient simulation was performed. In this simulation, the forcing is started during the calculation to observe the complete transition from the unforced (natural), separated flow to the forced. Utilizing the POD module of our toolbox, the amplitude of the unforced and forced mean flow modes are extracted (see figure 6.8). As can be seen in the figure, the flow changes from the unforced state, where the forced mean flow mode amplitude is approx. 1 and the unforced mode amplitude is 0, to the forced state with the amplitudes reversed. This significant change in mode amplitudes serves as a good indication of the flow state, and with an appropriate feedback gain, can be used as a feedback signal. However, it is also clear that a minimum threshold amplitude is needed to keep the flow attached.

In the simulation presented here, the amplitude limits were set to $A_{\max}=5.5\text{m/s}$ and $A_{\min}=2.5\text{m/s}$. With these limits, lift and drag as a function of time are shown in figure 6.9. When compared to the results of purely periodic blowing and suction at $A=4\text{m/s}$, the



feedback controlled run shows slightly lower lift and higher drag, but the forcing amplitudes are considerably lower. Figure 6.10 shows the amplitude of the unforced mean flow mode as a function of time (top) and the accompanying forcing velocity (bottom). Analyzing figures 6.9 and 6.10, it becomes clear that the controller is able to sense the deviation of the sensor signal from zero and accordingly increase the forcing amplitude. However, because of the time delay between forcing slot and the sensors, the controller is not able to react fast enough to suppress incipient separation. The short bursts of separated flow lead to the comparatively large temporal fluctuations of lift and drag.

These results are by no means optimal, but clearly demonstrates that our toolbox can be applied successfully for the case of separation control. To further improve the effectiveness of the controller, and especially to take the time delay between a change in actuation and the response at the sensor locations into account, different sensor and controller configurations are currently under investigation.

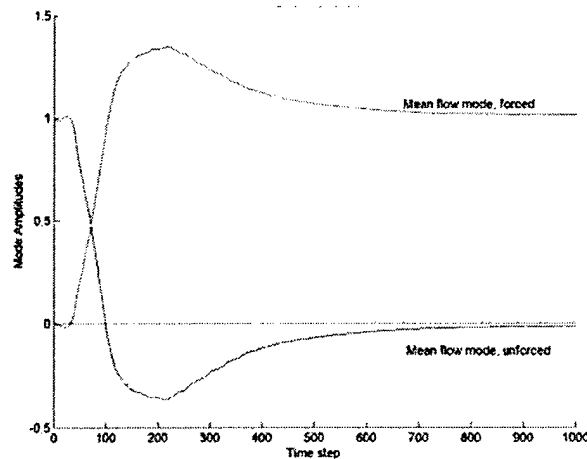


Figure 6.8: Temporal development of mean flow modes. Unforced (blue) and forced (red)

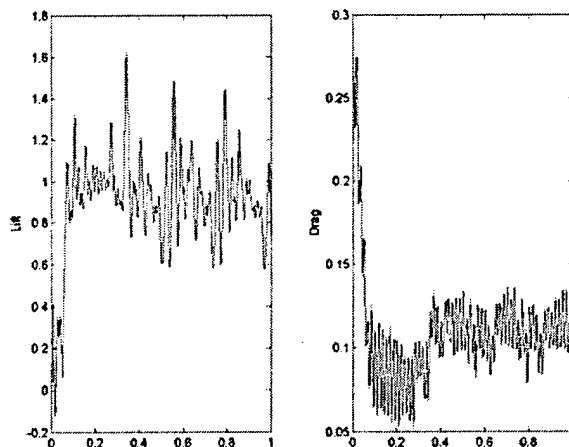


Figure 6.9: Lift (left) and drag (right) as a function of time for the feedback controlled run

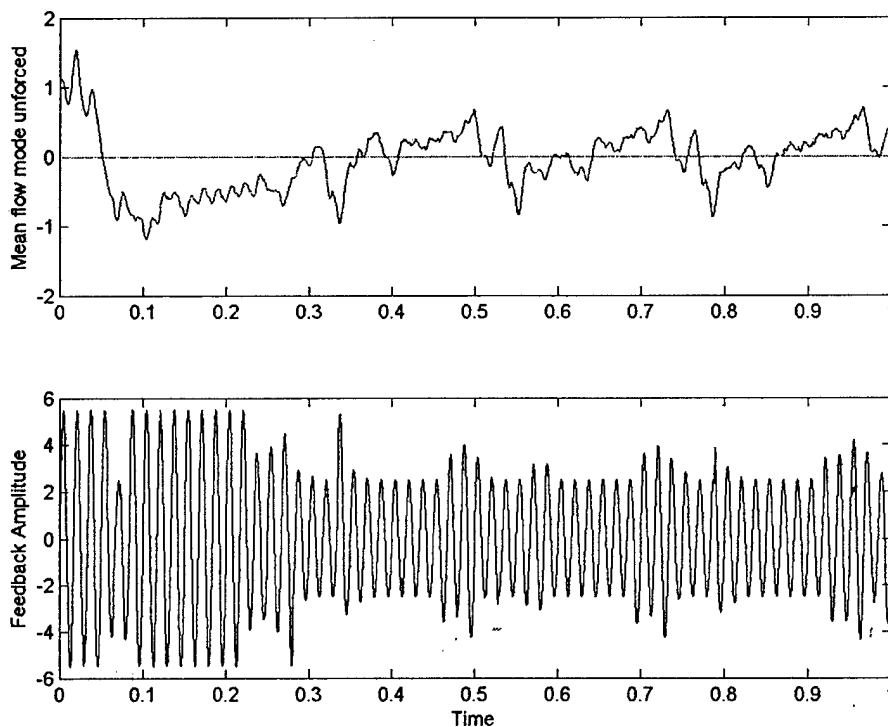


Figure 6.10: Amplitude of unforced mean flow mode (top) and forcing velocity (bottom)



6.4 NACA 0015 Airfoil: 3-D Baseline CFD

3-d calculations were performed for the NACA 0015 at the same flow conditions as controlled in 2-d, i.e. a Reynolds number of 10,000, and an angle of attack of 8 degrees. The 2-d grid used in the control case was extruded into the span using 66 points and one chord length, leading to 800,000 cells. Simulations were performed with a non-dimensional timestep of 0.01 (made non-dimensional by the chord and freestream velocity). LES with no explicit subgrid scale model was applied due to the expected laminar boundary layers. Flow visualizations are shown in Figure 6.11. The variation in separation in the spanwise direction is seen, again emphasizing the need to progress the closed loop tools to handle 3-D cases. The resolved content in this simulation is fairly weak compared to what may be expected at this Reynolds number, and what was seen for the circular and D-shaped cylinders. Further grid refinement may be required. These results will be available for subsequent attempts at control in 3-d during phase II.

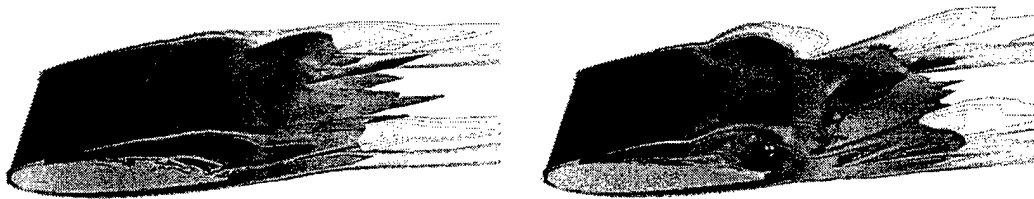
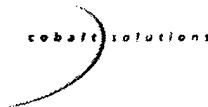


Figure 6.11 LES calculation of the NACA 0015 airfoil. Isosurface of vorticity colored by pressure. Flow shown at two different times.



7. Summary of Phase I & Recommendations for Phase II

At the end of Phase I of this project, we conclude that we developed a toolbox that meets or exceeds the capabilities outlined in the proposal. We were able to demonstrate the successful application of the toolbox to control three feedback flow control applications as proposed. For these reasons, in comparing our recommendations for phase II outlined in the next section, you will find them to be identical to the original suggestions we made in the Phase I proposal, with more detail added.

7.1 Main Achievements of Phase I

The main achievements of Phase I are as follows:

- Toolbox is complete and fully functional and tested
- Demonstrated application of our modeling and control approach to three different geometries, namely a Circular Cylinder, D shaped Cylinder and NACA 0015 airfoil
- Implemented and tested feedback controlled boundary conditions in the Cobalt CFD solver.
- Implemented and tested hdf output in the Cobalt CFD solver to provide data to the matlab based flow control toolbox components
- Performed 3D simulations of the D-shaped cylinder and the NACA 0015 airfoil
- Overall, we showed that we can accomplish low dimensional modeling, control and closed loop simulation for very different flow fields using very different actuation approaches. All of this applies to 2D flow fields.
- The POD algorithm developed deals with unstructured data and delivers accurate results at the body surface.
- A shell script was developed that starts the controller automatically with the CFD simulation from within the queue. Thus feedback controlled runs can be queued just like any other CFD simulation run.

These achievements meet and in some cases exceed the goals of the proposed research. They demonstrate the feasibility of the approach and are a sound basis to move ahead into Phase II of the STTR.



7.2 Recommended Development Approach for Phase II

1. Extend the capabilities of the Toolbox to 3D flow fields

Reasons and justification to do this:

- Recently, we found that even nominally 2D flow fields like the cylinder wake turn 3D once feedback control is applied (Siegel et al. 2004). Furthermore, higher Re flows tend to be 3D anyways.
- This suggests that in order to provide a toolbox that enables realistic feedback flow control, it is imperative to expand the capabilities to the 3D regime.
- While some parallel research teams may have / have 2D closed loop capabilities, usually they use home brew CFD codes that cannot easily be expanded to 3D.
- Cobalt has excellent 3D capabilities with DES and turbulence modeling. The proposed plan leverages Cobalt's strength in LES and DES. Cobalt's turbulence modeling software building blocks can be put to good use in order to be able to build low dimensional models at higher Reynolds numbers

2. Increase the Reynolds number into realistic Regimes

Reasons and justification to do this:

- While we have learned many important lessons in feedback flow control working on low Reynolds number problems, it is necessary to expand the Reynolds number range in order to be able to do real life problems
- This requires the 3D capabilities outlined above
- It again leverages Cobalt's strength in LES and DES
- Cobalt's turbulence modeling software building blocks can be put to good use in order to be able to build low dimensional models at higher Re

3. Extend the capabilities of the Toolbox to model Body Forces for actuation

Reasons and justification to do this:

- Body forces are a generic way to model actuation. They can be implemented at less cost in a CFD simulation than using a high resolution grid to accurately resolve actuator geometry, thus improving the performance of the simulation
- Body forces can be used to model the effect of plasma actuators, which have shown a lot of promise for feedback flow control applications due to their simple setup without any moving mechanical parts



8. Matlab Modeling and Control Toolbox Suite

This chapter is intended to give some insight into the functionality of the main components of the Matlab based feedback flow control toolbox developed within this program. It is neither complete, nor intended to be a manual for the toolbox, which will be developed in Phase II of the project. It lists the calling convention along with the documentation of the modules, which gives insight into both functionality and implementation of the tools. Note that none of the many sub-functions are listed, but rather the functions a typical user will interface with. Also omitted are scripts dedicated to plotting or presentation of data. The overall number of matlab scripts and functions in the toolbox specific to this project is currently in the order of 250.

```
function [EnergyContent, U_Modes,varargout] =
    POD_Modes(NModes, SubMean,varargin)
%
% [EnergyContent, U_Modes] = POD_Modes(NModes, SubMean, U_SnapShots)
% [EnergyContent, U_Modes, U_SnapShotMean] = POD_Modes(NModes, SubMean,
    U_SnapShots)
% [EnergyContent, U_Modes, V_Modes] = POD_Modes(NModes, SubMean,
    U_SnapShots, V_SnapShots)
% [EnergyContent, U_Modes, U_SnapShotMean, V_Modes, V_SnapShotMean] =
    POD_Modes(NModes, SubMean, U_SnapShots, V_SnapShots)
%
% General Inputs:
%   NModes:      While the POD yields as many modes as there are
%                 Snapshots, only NModes will be returned by this function
%   SubMean:     SubMean indicates if the average of all snapshots is to
%                 be subtracted
%                 before calculating the POD modes:
%   SubMean = 1: SnapShot Mean WILL be subtracted
%   SubMean = 0: SnapShot Mean WILL NOT be subtracted
%
% 1 Dimensional or unstructured Data:
%*****
%   The u and (optional) v velocity components are stored in matrices
%   with size NxM.
%   N is the number of gridpoints and M is the number of snapshots.
%   The Spatial Modes are returned in U,V_Modes, with size NxM.
%   U,V_SnapShotMean is the average of all U,V SnapShots, dimension is
%   Nx1.
%
% 2 Dimensional Data:
%*****
%   The 2D scalar Data Field(s) is/are in a 3D Matrix called U,V
%   SnapShots, size(SnapShots)=[Nx, Ny, M]
%   where: Nx and Ny are the number of gridpoints from in X and Y
%           Direction at intervals of DeltaXY
%   M is the number of snapshots, typically at different instants of time
%   The spatial Modes are returned in U,V Modes, with sizes [Nx Ny
%   NModes]
%
%
% The Energy Content of the retained modes is stored in EnergyContent.
```



```
%
% Revision History: Code assembled 3-10-2004

function [TimeCoeff] = POD_Time_Coeff(U_SnapShots, ModesU,
    varargin);
    % [TimeCoeff] = POD_Time_Coeff(U_SnapShots, ModesU)
    % [TimeCoeff] = POD_Time_Coeff(U_SnapShots, ModesU, MeanU)
    % [TimeCoeff] = POD_Time_Coeff(U_SnapShots, ModesU, V_SnapShots, ModesV)
    % [TimeCoeff] = POD_Time_Coeff(U_SnapShots, ModesU, MeanU, V_SnapShots,
    ModesV, MeanV)

    % Does a least squares fit to determine the temporal coefficients of the
    POD Modes
    % U Velocity and V Velocity as well as ModesU and ModesV need to have the
    same dimensions

function ReconData = POD_Reconstruct(Modes, SnapshotMean,
    TimeCoeff)
    %
    % ReconData = POD_Reconstruct(Modes, SnapshotMean, TimeCoeff)
    % Reconstructs the Snapshots in ReconData from Modes, Mean and Time
    Coefficients
    % 5-4-04 SGS supports UNS data

function OrthMatrix = POD_Orthogonality(Modes, DeltaXY)
    % Checks if the POD Modes are orthogonal.
    % If they are, OrthMatrix should equal the Kronecker delta function

function [ObsMatrix, EstimatedSignals, MeanErrors,
    ErrorSignals] =
    LinearStochasticEstimation(Observation, ToBeEstimated)

    %*****
    %
    % Purpose / Usage
    %*****
    %
    % Linear Mapping of Observations onto Estimated States or vice versa:
    %
    % If you use Time signals in a flow field as Observations
    % AND POD temporal coefficients as ToBeEstimated Signals
    % you will develop an ObsMatrix that you can multiply with instantaneous
    % Velocities in order to get POD Amplitude estimates

    % If you use Time signals in a flow field as ToBeEstimated Signals
    % AND POD temporal coefficients as Observations
    % you will develop an ObsMatrix that you can multiply with instantaneous
    % Mode Amplitudes in order to get Velocity Field estimates

    %*****
    %
    % Data Structures / Dimensions
    %*****
    %
    % Observation is a 2D matrix size M x N
    % M being the number of Observations
    % N being the number of time steps / samples
```




```
% ToBeEstimated is a 2D matrix that contains K x N time signals measured
in
% the flow field
% K is the number of signals to be estimated
% ObsMatrix is 2D and has K x M Elements
% ErrorSignals is KxN in size and has the difference between Estimated
and
% ToBeEstimated signals
% MeanErrors is a K size vector that has the mean square error for each
to be
% estimated signal in it, normalized by the instantaneous amplitude of
the signal

function [EstTempCoeff, FullTempCoeff, Error] =
  SensorBasedTempCoeff(XLoc, YLoc, XAxis, YAxis,
  PODModes, PODMean, SnapShots)
% [EstTempCoeff, FullTempCoeff, Error] ...
% = SensorBasedTempCoeff(XLoc, YLoc, XAxis, YAxis,
  PODModes, PODMean, SnapShots)
%
% Calculates the Temporal Coefficients based on both the full flow field
% contained in the SnapShots,
% as well as the Flow Field sampled at the XLoc, YLoc Locations
% Error is the difference between the two
% Uses least square fitting to estimate the Temp Coeff for both full flow
% field and sensor based estimation

function [ModeCoeff, Indices] = POD_Model(TimeCoeff,
  MaxMode)

% Creates a low order model  $dA_n/dt = f(C_0 + c_{1i}A_i + c_{2ij}A_{ij} + c_{3ijk}A_{ijk})$ 
of cubic order
% Indices returns a 2D Array, the columns are first second third
coefficient and so on
% the rows are one term each
% Calculates all linear and quadratic coefficients
% Modified to include only cubic terms up to Mode Number MaxMode

function [FilteredTime, FilteredTempCoeff] =
  SplineFilterTempCoeff(Time, TempCoeffs, NPoints)
%
% [FilteredTime, FilteredTempCoeff] = SplineFilterTempCoeff(Time,
  TempCoeffs, NPoints)
% uses spline_filter to filter each Temporal Coefficient
% NPoints determines the width of filter kernel in data points, and has
one
% element for each TempCoeff to allow different filter settings for each
% mode
% the resulting FilteredTempCoeff are shorter in time by two times the
% maximum filter kernel width

function CFD_Controller_Main_V3(CaseName,varargin)
% CFD_Controller_Main_V3(CaseName) As before
% CFD_Controller_Main_V3(CaseName,NodeNumber) NodeNumber: hostnode
of cobalt run
%
% interfaces to Cobalt CFD code for closed loop flow control
% filepath is the fully qualified path to the hdf file created by cobalt
```



```
% MaxIteration is the number of time steps for this run
% V3 supports unstructured POD modes and feedback controlled Boundary
%
% varargin added for support of remote execution
```

```
function [FileStructure] = Read_HDF_Cobalt(Filename,
    varargin)
%
% [FileStructure] = Read_HDF_Cobalt(Filename)
% [FileStructure] = Read_HDF_Cobalt(Filename, Skip)
% [FileStructure] = Read_HDF_Cobalt(Filename, NStart, NTimeSteps)
% [FileStructure] = Read_HDF_Cobalt(Filename, Skip, NStart, NTimeSteps)
% Reads all the non-empty SDS'es in an hdf mtap file created by Cobalt V3
% If NStart and NTimeSteps are specified, only the N Time steps starting
at NStart
% will be read
% If Skip is specified, only every Skip-th data point in space will be
% loaded
% FileStructure: Name of a structure that will hold all the variables in
the hdf file
% c 2004 Stefan Siegel
```

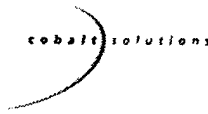


9. References

- Abergel, F. and Temam, R., "On some Control Problems in Fluid Mechanics", *Theor. Comput. Fluid Dynamics*, Vol. 1, 1990, p. 303.
- Adrian, R.J., "On the Role of Conditional Averages in Turbulence Theory", *Proceedings of the Fourth Biennial Symposium on Turbulence in Liquids*, J. Zakin and G. Patterson (Eds.), Science Press, Princeton, 1977, pp. 323-332.
- Balas M.J., "Active Control of Flexible Systems", *Journal of Optimization Theory and Applications*, Vol. 25, No. 3, 1978, pp. 217-236.
- Cameron, J., Sick, A., Cohen, K., Wetlesen, D., and Siegel, S., "Determination of an Effective Sensor Configuration for Suppression of the von Kármán Vortex Street", AIAA Region V Student Paper Conference, University of Colorado, Boulder, CO, April 9-11, 2003 .
- Cattafesta III, L.N., Williams, D.R., Rowley, C.W., and Alvi, F.S., "Review of Active Control of Flow-Induced Cavity Resonance", AIAA Paper 2003-3567, June 2003.
- *Cohen, K., Siegel S., McLaughlin T., and Myatt J., "Proper Orthogonal Decomposition Modeling Of A Controlled Ginzburg-Landau Cylinder Wake Model", 41st AIAA Aerospace Sciences Meeting & Exhibit, Reno, NV, Jan. 6-9 2003, Reston, VA: AIAA, Inc., AIAA Paper 2003-1292.
- *Cohen K., Siegel S., McLaughlin T., and Gillies E., "Feedback Control of a Cylinder Wake Low-Dimensional Model", 55th APS/DFD Meeting, Vol. 47, No. 10, Paper DN 2, Dallas, TX, Nov. 24-26, 2002.
- *Cohen K., Siegel S., McLaughlin T., and Gillies E., "Feedback Control of a Cylinder Wake Low-Dimensional Model", AIAA Journal, Vol. 41, No. 8, August 2003.
- *Cohen, K., Siegel S., McLaughlin T., and Myatt J., "Proper Orthogonal Decomposition Modeling Of A Controlled Ginzburg-Landau Cylinder Wake Model", 41st AIAA Aerospace Sciences Meeting & Exhibit, Reno, NV, Jan. 6-9 2003, Reston, VA: AIAA, Inc., AIAA Paper 2003-1292.
- Constantinescu, G.S., Pacheco, R. and Squires, K.D., "Detached-eddy simulation of flow over a sphere", *AIAA Paper 2002-0425*, 2002.
- Constantinescu, G.S., Chapelet, M. and Squires, K.D., "Prediction of the turbulent flow over a sphere", accepted for publication in *AIAA Journal*, 2003.



- Forsythe, J.R., Strang, W., Hoffmann, K.A., "Validation of Several Reynolds-Averaged Turbulence Models in a 3D Unstructured Grid Code," AIAA 00-2552, June 2000.
- Forsythe, J.R., Squires, K.D., Wurtzler, K.E. and Spalart, P.R., "Detached-Eddy Simulation of the F-15E at High Alpha", *AIAA Journal of Aircraft*, Vol. 41, No. 2, 2004, pp. 193-200.
- Forsythe, J.R., Hoffmann, K.A., Cummings, R.M., Squires, K.D., "Detached-Eddy Simulation with Compressibility Corrections Applied to a Supersonic Axisymmetric Base," *Journal of Fluids Engineering*, Vol. 124, No. 4, 2002, pp. 911-923.
- Forsythe, J.R., Woodson, S.H., "Unsteady CFD Calculations of Abrupt Wing Stall Using Detached-Eddy Simulation", AIAA 2003-0594, Jan 2003.
- Gad-el-Hak, M., "Modern Developments in Flow Control", *Applied Mechanics Reviews*, vol. 49, 1996, pp. 365-379.
- Gillies, E. A., "Low-dimensional Control of the Circular Cylinder Wake", *Journal of Fluid Mechanics*, Vol. 371, 1998, pp. 157-178.
- Gottlieb, J.J. and Groth, C.P.T., 1988, "Assessment of Riemann Solvers for Unsteady One-Dimensional Inviscid Flows of Perfect Gases", *Journal of Computational Physics*, pp. 437-458.
- Grismer, M. J., Strang, W. Z., Tomaro, R. F. and Witzeman, F. C., "Cobalt: A Parallel, Implicit, Unstructured Euler/Navier-Stokes Solver", *Advances in Engineering Software*, Vol. 29, No. 3-6, pp. 365-373, 1998.
- *Hansen, R.P. and Forsythe, J.R., "Large and Detached Eddy Simulations of a Circular Cylinder Using Unstructured Grids", *AIAA Paper 2003-0775*, 2003.
- Holmes, P., Lumley, J.L., and Berkooz, G., "Turbulence, Coherent Structures, Dynamical Systems and Symmetry", Cambridge University Press, Cambridge, 1996.
- Karypis, G., Schloegel, K., and Kumar, V, ParMETIS: Parallel Graph Partitioning and Sparse Matrix Ordering Library Version 1.0. University of Minnesota, Department of Computer Science, Minneapolis, MN 55455, July 1997.
- Koopmann, G., "The Vortex Wakes of Vibrating Cylinders at Low Reynolds Numbers", *Journal of Fluid Mechanics*, Vol. 28 Part 3, 1967, pp. 501-512.
- *Krishnan, V., Squires, K.D., Forsythe, J.R., "Prediction of Separated Flow over a Hump Using RANS and DES," *AIAA Paper 2004-2224*, 2004.



Luchtenburg, M., Cohen, K., D., Siegel, S., McLaughlin, T., Noack, B., and Tadmor, G.
"Low Dimensional Model of a Cylinder Wake", Session EM, EM.005, 56th APS/DFD
Meeting, Nov. 23-25, 2003, New Jersey.

Morton, S.A., Steenman, M.B., Cummings, R.M. and Forsythe, J.R., "DES grid
resolution issues for vortical flows on a delta wing and an F-18C", *AIAA 2003-1103*,
2003.

Norberg, C., "Effects of Reynolds Number and Low-Intensity Free-Stream Turbulence
on the Flow Around a Circular Cylinder". *Publication 87/2, Department of Applied
Thermosciences and Fluid Mechanics, Chalmers University of Technology*,
Gothenburg, Sweden, 1987.

Roshko, A., "Experiments on the Flow past a Circular Cylinder at Very High Reynolds
Number", *Journal of Fluid Mechanics* 10(3), 345-356, 1961.

Roussopoulos, K., "Feedback Control of Vortex Shedding at Low Reynolds Numbers",
Journal of Fluid Mechanics, Vol. 248, 1993, pp. 267-296.

Serrano, M., Leigh, E., Johnson III, W., Forsythe, J.R., Morton, S.A. and Squires, K.D.,
"Computational aerodynamics of the C-130 in airdrop configurations", *AIAA Paper
2003-0229*, 2003.

*Siegel S., Cohen, K. and McLaughlin T., (2003a) "Feedback Control of a Circular
Cylinder Wake in Experiment and Simulation", Invited lecture at the 33rd AIAA Fluid
Dynamics Conference and Exhibit, Orlando, AIAA-2003-3569, June 23-26 2003.

*Siegel S., Cohen, K., and McLaughlin T., (2003b) "Low-Dimensional Feedback Control
of the von Karman Vortex Street at a Reynolds number of 100", (accepted for
presentation at IUTAM Symposium: Fluid-Structure Interactions, Piscataway, USA,
June 2-6 2003).

*Siegel S., Cohen K., Smith D., and McLaughlin T., "Observability Conditions for POD
Modes in a Circular Cylinder Wake", 55th APS/DFD Meeting, Vol. 47, No. 10, Paper
DN 4, Dallas, TX, Nov. 24-26, 2002.

*Siegel S., Cohen K., McLaughlin T., and Myatt J., "Real-Time Particle Image
Velocimetry for Closed-Loop Flow Control Studies", 41st AIAA Aerospace Sciences
Meeting & Exhibit, Reno, NV, Jan. 6-9 2003, Reston, VA: AIAA, Inc., AIAA Paper
2003-0920.

Sirovich, L., "Turbulence and the Dynamics of Coherent Structures Part I: Coherent
Structures", *Quarterly of Applied Mathematics*, Vol. 45, No. 3, 1987, pp. 561-571.



- *Smith, D. R., Siegel, S., and McLaughlin T., "Modeling of the wake Behind a Circular Cylinder Undergoing Rotational Oscillation", AIAA Paper 2002-3066, June 2002.
- *Smith D., Cohen K., Siegel S., McLaughlin T., "Towards Closed-loop Control of the Wake behind a Circular Cylinder Using Rotational Oscillations", (currently under review of the *Physics of Fluids*), 2003.
- Spalart, P.R., Jou, W-H., Strelets, M. , and Allmaras, S.R., "Comments on the Feasibility of LES for Wings, and on a Hybrid RANS/LES Approach," *Advances in DNS/LES*, 1st AFOSR International Conference on DNS/LES, Greyden Press, Columbus, OH, 1997.
- Spalart, P.R., "Strategies for Turbulence Modeling and Simulations", *International Journal of Heat and Fluid Flow*, **21**, p. 252-263, 2000.
- Squires, K.D., Forsythe, J.R. and Spalart, P.R., "Detached-Eddy Simulation of the separated flow around a forebody cross-section", *Direct and Large-Eddy Simulation IV*, ERCOFTAC Series – Volume 8, B.J. Geurts, R. Friedrich and O. Metais, editors, Kluwer Academic Press, pp. 481-500, 2001.
- Squires, K.D., Forsythe, J.R., Morton, S.A., Strang, W.Z., Wurtzler, K.E., Tomaro, R.F., Grismer, M.J. and P.R. Spalart, "Progress on Detached-Eddy Simulation of massively separated flows", *AIAA Paper 2002-1021*, 2002.
- Strang, W.Z., Tomaro, R.F, Grismer, M.J., 1999, "The Defining Methods of Cobalt60: a Parallel, Implicit, Unstructured Euler/Navier-Stokes Flow Solver", AIAA 99-0786, January 1999.
- Tomaro, R.F., Strang, W.Z., and Sankar, L.N., 1997, "An Implicit Algorithm for Solving Time Dependent Flows on Unstructured Grids, AIAA 97-0333, January 1997.
- Travin, A., Shur, M., Strelets, M., and Spalart P., "Detached-Eddy Simulations Past a Circular Cylinder", *Flow Turbulence and Combustion*, **63**, 293-313, 1999.
- Tremblay, F., Manhart, M., Friedrich, R., "DNS of Flow Around a Circular Cylinder at a Subcritical Reynolds Number with Cartesian Grids", *Proceedings of the 8th European Turbulence Conference, EUROMECH*, Barcelona, Spain, June 2000.
- van Nunen, J.W.G., "Pressure and Forces on a Circular Cylinder in a Cross Flow at High Reynolds Numbers", in Naudasher, E. (ed.), *Flow Induced Structural Vibrations*, Springer-Verlag, Berlin, 748-754, 1974.